

Analysis of Structural Development During Superdrawing of Poly(ethylene terephthalate)
Fibers

A Thesis
Presented to
The Academic Faculty

By

Vibhor Jain

In Partial Fulfillment
Of the Requirements for the Degree
Doctor of Philosophy in
Polymer, Textile and Fiber Engineering

Georgia Institute of Technology

May, 2009

ANALYSIS OF STRUCTURAL DEVELOPMENT DURING SUPERDRAWING OF
POLY (ETHYLENE TEREPHTHALATE) FIBERS

Approved by:

Dr. Youjiang Wang, Advisor
School of Polymer, Textile and Fiber
Engineering
Georgia Institute of Technology

Dr. Karl I. Jacob, Advisor
School of Polymer, Textile and Fiber
Engineering
Georgia Institute of Technology

Dr. Yonathan S. Thio
School of Polymer, Textile and Fiber
Engineering
Georgia Institute of Technology

Dr. Donggang Yao
School of Polymer, Textile and
Fiber Engineering
Georgia Institute of Technology

Dr. Hamid Garmestani
School of Materials Science and
Engineering
Georgia Institute of Technology

Date Approved: January 06, 2009

To my parents and the Almighty without whose grace this work would not be possible.

*I have been extremely fortunate to have their unwavering love and blessings
throughout my life.*

ACKNOWLEDGEMENTS

First and foremost, I would like to thank my advisors, Professors Youjiang Wang and Karl I. Jacob. Their continued support and visionary guidance has made this achievement possible. It is their advice and excellent supervision that proved critical to solving the many challenges during the course of this study. It is their patience with my numerous questions and the energy they put into my development that I have reached where I am. I am grateful to them for this feeling of personal growth and satisfaction. Although I am amazed at the distance travelled since the start of this study, I realize that many more goals remain to be achieved, and I look forward to putting in my best efforts.

I am especially grateful to Dr. Xin Li for his tremendous help in the experimental design of this study. His inspiration was essential for the ideas behind this study. In addition, I would like to thank Yutong Pan for her help with the experiments. I would also like to thank the graduate students at the Polymer, Textile and Fiber Engineering school. My special thanks go to graduate students Shamal K. Mhetre and Kishor K. Gupta who provided invaluable help and support at all times.

Last, but certainly not the least, I would like to thank the staff and people at the various labs all of whom have contributed in many important ways.

TABLE OF CONTENTS

ACKNOWLEDGEMENTS	IV
LIST OF TABLES	X
LIST OF FIGURES.....	XI
LIST OF SYMBOLS AND ABBREVIATIONS	XVI
SUMMARY	XIX
CHAPTER 1. INTRODUCTION	1
CHAPTER 2. LITERATURE REVIEW	6
2.1 Types of drawing.....	6
2.1.1 Conventional Mechanical Drawing.....	6
2.1.2 The Superdrawing Process.....	7
2.1.3 Mechanisms of Superdrawing.....	7
2.1.4 Advantages of Superdrawing	8
2.1.5 Superdrawing of hollow PET fibers.....	9
2.2 Typical tensile behavior of PET in an amorphous state: strain-induced crystallization (SIC) associated with necking	9
2.2.1 Theoretical description of strain-induced crystallization (SIC)	13
2.3 Structure evolution in PET fiber extrusion – effect of spinning conditions.....	16
2.3.1 Differences between conventional and high-speed spinning	16
2.3.2 High-speed spun fibers: a brief overview	18
2.3.3 Physical properties of fibers as a function of spinning speed	18

2.3.4	Mechanisms of development of superstructure of as-spun fibers	23
2.3.5	Molecular orientation and flow-induced crystallization in high-speed spinning25	
2.3.6	Necking deformation in high-speed spinning	27
2.4	Crystallization behavior during drawing	29
2.4.1	Important processes during drawing	29
2.5	Aspects of stress-strain behavior of PET.....	30
2.5.1	Role of Temperature.....	30
2.5.1.1	Drawing under T_g (Cold Drawing).....	30
2.5.1.2	Drawing above T_g (Hot Drawing).....	34
2.5.1.3	Effect of temperature - strain rate regimes	37
2.5.2	Role of strain rate	39
2.5.3	Role of amorphous phase orientation.....	44
2.6	Studies of the crystallization behavior of PET	48
2.7	Rate of crystallization.....	60
2.7.1	Homogeneous nucleation of unoriented melts	60
2.7.2	Kinetics of quiescent crystallization	64
2.7.3	Nucleation rate under applied stress.....	65
2.7.3.1	Failure of nucleation theory under large stress and supercooling.....	66
2.7.4	Kinetics of strain-induced crystallization (SIC).....	67
2.7.5	Governing transport equations	71
2.8	Models to describe the mechanical behavior of PET	72
2.8.1	Background	72
2.8.2	Constitutive relationships proposed on basis of molecular structure.....	74
2.8.3	Mathematical formulations	80

2.8.3.1 Intermolecular resistance.....	80
2.8.3.2 Network resistance	82
2.9 On the elastic modulii of the amorphous and crystalline phases of PET	84
2.10 Literature review summary	88
CHAPTER 3. OBJECTIVES	91
3.1 Motivation	91
3.2 Research plan.....	91
3.2.1 Scope of study	91
3.2.2 Process conditions for superdrawing.....	93
3.3 Specific Goals.....	94
CHAPTER 4. EXPERIMENTAL STUDIES	96
4.1 Materials	96
4.2 Stress-strain curves during uniaxial stretching of amorphous PET fibers at different temperatures and strain rates	98
4.2.1 Methodology	98
4.2.1.1 Drawing apparatus.....	98
4.2.2 Effect of temperature on the drawing behavior as a function of strain rate	99
4.3 Study of crystallization behavior of drawn PET fibers using differential scanning calorimetry (DSC).....	108
4.3.1 Methodology	108
4.3.2 Effect of draw conditions on the crystallization in drawn PET samples ..	108
4.3.3 Effect of crystallization rate on crystallinity development	119
4.3.3.1 Isothermal crystallization parameters of amorphous PET - Avrami kinetic analysis	120

4.3.3.2 Comparison of drawing time with crystallization rate and its effect on crystallinity development	124
4.4 Analysis of the development of orientation in drawn PET fibers using polarized microscopy	125
4.4.1 Methodology	126
4.4.2 Effect of draw conditions on the orientation in drawn PET samples.....	126
4.4.2.1 Birefringence as a function of draw temperature	127
4.4.2.2 Birefringence as a function of strain rate	129
4.4.2.3 Birefringence as a function of draw ratio.....	130
4.5 Analysis of mechanical, thermal and orientation behavior at representative strain rates	133
4.6 Summary.....	138
CHAPTER 5. MODELING THE NON-LINEAR VISCOELASTIC DEFORMATION BEHAVIOR OF PET FIBERS	
5.1 Constitutive relations for the large strain stress-strain behavior of amorphous PET at different temperatures and strain rates	141
5.1.1 Summary of the model	142
5.1.2 Intermolecular resistance (A).....	145
5.1.2.1 Elasticity modeling.....	146
5.1.2.2 Effect of crystallization	149
5.1.3 Entropic resistance (B).....	149
5.1.4 Model parameters	152
5.1.4.1 Viscosity parameter: η	152
5.1.4.2 Initial modulus of the crystalline phase: E_c	153
5.1.4.3 Initial modulus of the amorphous phase: E_a	153
5.1.4.4 Limiting stretch ratio of the amorphous PET network: λ_{\max}	154

5.1.4.5 Molar mass of the PET elastic subchain: M_s	154
5.1.4.6 Constants of the hardening parameter: $C1$, $C2$, α and σ_0	155
5.2 Comparison of predictions with experiment	156
5.2.1 90°C.....	157
5.2.2 105°C.....	159
5.2.3 110°C.....	161
5.2.4 115°C.....	163
5.2.5 120°C.....	165
5.3 Evolution of crsytallinity	167
5.4 Significance of model parameters	169
5.4.1 Deficiencies in the model and possible ways of improvement	172
5.4.2 Model predictions at other drawing conditions.....	172
5.5 Summary.....	173
CHAPTER 6. CONCLUSIONS AND FUTURE DIRECTIONS.....	174
6.1 Conclusions	174
6.2 Future directions	177
REFERENCES.....	179

LIST OF TABLES

Table 1. Various types of nucleation and growth processes and its relation with Avrami exponent (From Ref. 93)	58
Table 2. Description of the fiber samples used	97
Table 3. Tensile properties of the as-spun fibers at room-temperature and strain rate of 0.083 s^{-1} (5 inches min^{-1}).....	97
Table 4. Thermal properties of the as-spun fibers measured on Seiko 220 DSC at a heating rate of $10^{\circ}\text{C min}^{-1}$	97
Table 5. Thermal properties of the fibers drawn at 90°C to draw ratio of 3 at different strain rates	111
Table 6. Thermal properties of the fibers drawn at 105°C and different strain rates.....	112
Table 7. Thermal properties of the fibers drawn to draw ratio of 3 at 0.008 s^{-1} and at 90 and 105°C as compared to as-spun fibers	113
Table 8. Thermal properties of the fibers drawn at 115°C to draw ratio of 8 and different strain rates	116
Table 9. Isothermal crystallization parameters for amorphous PET	123
Table 10. Thermal properties of the fibers drawn at representative strain rates and different temperatures	137
Table 11. Parameter window for Superdrawing.....	138
Table 12. The values of constant of the hardening parameter (σ_0) and the sensitivity coefficient (C) at all deformation conditions	152
Table 13. Viscous dashpot parameter η (MPa.s) at all deformation conditions	153
Table 14. Young's modulus of crystalline phase of PET (GPa) at all deformation conditions	153
Table 15. Young's modulus of amorphous phase of PET (GPa) at all deformation conditions	154
Table 16. Values of the molar mass of subchain of PET network (From Ref. 143).....	154
Table 17. The values of constants of the non-linear hardening parameter $f(\epsilon)$: C_1 , C_2 and α , at all deformation conditions.....	156

LIST OF FIGURES

Figure 1. Different stages in the typical stress-strain response of a ductile material.....	10
Figure 2. Load elongation curves in the two stretching regimes for PET (a) deformed below T_g and (b) deformed above T_g (From Ref. 21).....	11
Figure 3. Variation in the draw stress and crystallinity level with strain rate at two temperatures above the glass transition (From Ref. 21).....	12
Figure 4. Effect of strain rates (or take-up speed) on the mechanical and optical properties of PET fibers (From Ref. 28)	21
Figure 5. WAXS photographs of as-spun PET fibers (From Ref. 28).....	22
Figure 6. Effect of take-up speed on the morphological development of PET fibers (From Ref. 27).....	25
Figure 7. DSC thermograms at 20°C/min of PET fibers drawn to different draw ratios (From Ref. 12).....	31
Figure 8. Wide-angle x-ray patterns of (a) Amorphous; (b) Cold-drawn (necked portion); (c) Cold-drawn sample annealed at 140°C for 10 min at constant length; (d) Cold-drawn sample annealed at 140°C for 10 min without constraint; (e) Cold-drawn sample stretched another 20% at 90°C (From Ref. 2).....	34
Figure 9. Wide-angle x-ray diffraction patterns for PET stretched at 80°C to different strains: (a) undrawn, 0%; (b) 80%; (c) 175%; (d) 255%; (e) 250% (From Ref. 2)	36
Figure 10. Critical draw ratio for onset of strain-induced.....	39
Figure 11. Crystallinity versus draw ratio at different temperatures and strain rates (From Ref. 15).....	41
Figure 12. Increase in fractional crystallinity with draw ratio for PET drawn at 80°C and 0.007 s ⁻¹ (From Ref. 30)	46
Figure 13. True stress–strain curves from drawing amorphous PET at.....	46
Figure 14. DSC scans for as-drawn and relaxed PET samples drawn at 80°C and	47

Figure 15. Tensile stress as a function of draw ratio at 0.06 s^{-1} and 95°C (From Ref. 87)	50
Figure 16. Tensile stress as a function of draw ratio at 0.75 s^{-1} and 95°C (From Ref. 87)	50
Figure 17. Comparison of the evolution of the maximum dichroism (blank squares) versus the initial strain rate at 90°C and the evolution of the final value of the crystallinity (filled blocks) ratio (From Ref. 88)	52
Figure 18. Change in storage modulus (G') versus time at 220°C for PET at frequencies of 1, 3 and 5 rad/s (From Ref. 89)	53
Figure 19. Change in dynamic viscosity (η') versus time at 220°C for PET at frequencies of 1, 3 and 5 rad/s (From Ref. 89)	54
Figure 20. Areas of the 971 cm^{-1} (<i>trans</i>) and 1370 cm^{-1} (<i>gauche</i>) bands as a function of time during isothermal crystallization at 93°C (From Ref. 91)	56
Figure 21. Comparison of crystallization half-time values obtained in two works (From Ref. 92)	57
Figure 22. Fractional crystallinity as a function of time at $T_c = 100^\circ\text{C}$ for PET with f_a (from left to right) = 0.123, 0.044, 0.023 (From Ref. 96)	60
Figure 23. Schematic representation of the breakdown of the total resistance into an intermolecular resistance A occurring in parallel with a network resistance B. The network resistance was modeled as consisting of a molecular relaxation process in addition to a network orientation process (From Ref. 102)	78
Figure 24. Schematic showing the decomposition of total polymer resistance into an intermolecular resistance (A) acting in parallel with a network resistance (B): (a) Upper bound- intermolecular resistance as a parallel combination of amorphous and crystalline phase stiffness and flow; (b) Lower bound- intermolecular resistance as a series combination of amorphous and crystalline phase stiffness and flow (From Ref. 124)	79
Figure 25. The schematic representation of the parallel-series model (From Ref. 138)	87
Figure 26. A schematic drawing of the insulated chamber along with the sample attached to the Instron for hot drawing of PET samples	99
Figure 27. A schematic illustration of the types of mechanical response of PET fibers observed under different stretching conditions	100

Figure 28. Stress-strain curves, until failure, at 90°C showing the type-I draw behavior that leads to non-superdrawn samples. Different strain rates are indicated	101
Figure 29. Stress-strain curves, until failure, at 105°C showing the type-II drawing behavior at small strain rates that leads to unoriented superdrawn samples. Type-I behavior is observed at the fastest strain rates of 0.333 s ⁻¹ and 0.425 s ⁻¹	102
Figure 30. Stress-strain curves at 110°C at different strain rates	105
Figure 31. Stress-strain curves at 115°C. Different strain rates are indicated. Note that only the samples at 0.008 and 0.016 s ⁻¹ failed due to SIC.....	106
Figure 32. Stress-strain curves at 120°C at different strain rates	107
Figure 33. The primary thermal transitions during non-isothermal DSC scans.....	109
Figure 34. DSC scans (10°C min ⁻¹) of samples drawn at 90°C at different strain rates .	110
Figure 35. DSC scans (10°C min ⁻¹) of samples drawn at 105°C to draw ratios greater than 10. Different strain rates are indicated	112
Figure 36. DSC scans (10°C min ⁻¹) of samples drawn to draw ratio of 3 at 0.008 s ⁻¹ and at 90 and 105°C as compared to undrawn (as-spun) fibers.....	113
Figure 37. DSC scans (10°C min ⁻¹) of samples drawn to draw ratio of 8 at 110°C. Different strain rates are indicated	115
Figure 38. DSC scans (10°C min ⁻¹) of samples drawn to draw ratio of 8 at 115°C. Different strain rates are indicated	116
Figure 39. DSC scans (10°C min ⁻¹) of samples drawn to draw ratio of 8 at 120°C. Different strain rates are indicated	117
Figure 40. The Avrami plot for isothermal crystallization of amorphous PET at 105°C	120
Figure 41. The Avrami plot for isothermal crystallization of amorphous PET at 110°C	121
Figure 42. The Avrami plot for isothermal crystallization of amorphous PET at 115°C	121
Figure 43. The Avrami plot for isothermal crystallization of amorphous PET at 120°C	122
Figure 44. The development of fractional crystallinity during isothermal crystallization of amorphous PET at different temperatures.....	123

Figure 45. A graph between drawing time and strain rate at three draw ratios. The dotted straight lines mark the threshold time, shown for two draw temperatures, above which a sample undergoes thermal crystallization during drawing.....	125
Figure 46. Birefringence for samples drawn to draw ratio of 5 versus draw temperature at three strain rates	127
Figure 47. Birefringence for samples drawn to draw ratio of 10 versus draw temperature at five strain rates	128
Figure 48. Birefringence for samples drawn to draw ratio of 5 versus strain rate at four draw temperatures	129
Figure 49. Birefringence for samples drawn to draw ratio of 10 versus strain rate at four draw temperatures	130
Figure 50. Birefringence versus draw ratio for three selected strain rates at draw temperature of 105°C	131
Figure 51. Birefringence versus draw ratio for three selected strain rates at draw temperature of 110°C	131
Figure 52. Birefringence versus draw ratio for three selected strain rates at draw temperature of 115°C	132
Figure 53. Birefringence versus draw ratio for three selected strain rates at draw temperature of 120°C	132
Figure 54. Stress-strain curves for four draw temperatures at representative strain rates: (a) 0.008 s ⁻¹ , (b) 0.166 s ⁻¹ and (c) 0.425 s ⁻¹	134
Figure 55. DSC scans at 10°C/min of PET drawn at different temperatures and at rates of (a) 0.008/s, (b) 0.166/s and (c) 0.425/s; compared with as-spun fibers	136
Figure 56. Birefringence versus draw ratio for four different draw temperatures at the strain rates of (a) 0.008/s and (b) 0.425/s.....	138
Figure 57. Schematic representation of breakdown of overall resistance to deformation	144
Figure 58. Schematic representation of the parallel-series model for determination of modulus	147
Figure 59. Predicted stress-strain curves at the draw temperature of 90°C for the strain rates of (a) 0.008 s ⁻¹ , (b) 0.166 s ⁻¹ and (c) 0.425 s ⁻¹	158

Figure 60. Predicted stress-strain curves at the draw temperature of 105°C for the strain rates of (a) 0.008 s ⁻¹ , (b) 0.166 s ⁻¹ and (c) 0.425 s ⁻¹	160
Figure 61. Predicted stress-strain curves at the draw temperature of 110°C for the strain rates of (a) 0.008 s ⁻¹ , (b) 0.166 s ⁻¹ and (c) 0.425 s ⁻¹	162
Figure 62. Predicted stress-strain curves at the draw temperature of 115°C for the strain rates of (a) 0.008 s ⁻¹ , (b) 0.166 s ⁻¹ and (c) 0.425 s ⁻¹	164
Figure 63. Predicted stress-strain curves at the draw temperature of 120°C for the strain rates of (a) 0.008 s ⁻¹ , (b) 0.166 s ⁻¹ and (c) 0.425 s ⁻¹	166
Figure 64. The evolution of weight fraction crystallinity (calculated), y, with time of drawing at the strain rate of 0.008 s ⁻¹ for all draw temperatures.....	168
Figure 65. The evolution of weight fraction crystallinity (calculated), y, with time of drawing at the strain rate of 0.166 s ⁻¹ for all draw temperatures.....	168
Figure 66. The evolution of weight fraction crystallinity (calculated), y, with time of drawing at the strain rate of 0.425 s ⁻¹ for all draw temperatures.....	169
Figure 67. Variation of viscosity coefficient (η) of the intermolecular resistance with (a) 1/temperature and (b) strain rate [data adapted from Ref. 43].....	170

LIST OF SYMBOLS AND ABBREVIATIONS

A	Intermolecular resistance to deformation
α	Constant of the hardening parameter
B	Network resistance to deformation
C	Sensitivity parameter to non-linear strain stiffening
C₁	Constant of the hardening parameter
C₂	Constant of the hardening parameter
Δf	Gibbs free energy change
ΔG	Bulk free energy of fusion per unit volume
Δh	Enthalpy change
ΔH^*	Enthalpy of formation of crystallite
ΔH_0	Enthalpy of fusion for a 100% crystalline PET
ΔH_c	Area under cold crystallization peak
ΔH_m	Area under melting peak
$\Delta \phi$	Total free energy of an embryonic nucleus
$\Delta \phi^*$	Free energy of formation of a nucleus of critical size
ΔS^*	Entropy of formation of crystallite
$\Delta s/\Delta S'/\Delta S_{el}$	Entropy change during crystallization
ΔT	Supercooling
DSC	Differential scanning calorimetry
E	Elastic modulus of spring
E_a	Elastic constant of the amorphous phase
E_c	Elastic constant of the crystalline phase
$E_{c\equiv}$	Crystal modulus along the fiber axis
E_f	Fiber modulus
ε	Total applied strain
ε_A	Strain in intermolecular resistance
ε_B	Strain in network resistance
$\dot{\varepsilon}$	Strain rate

η	Viscosity parameter of dashpot
\mathbf{F}	Total applied deformation gradient
\mathbf{f}	Correction factor in Nakamura equation
$f(\varepsilon)$	Dimensionless hardening parameter
\mathbf{F}_A	Deformation gradient of intermolecular resistance
\mathbf{F}_B	Deformation gradient of network resistance
FTIR	Fourier transform infra-red
h	Planck's constant
\mathbf{I}	Homogenous nucleation rate in absence of stress
\mathbf{I}_0	Nucleation rate constant
IR	Infra-red
k	Boltzmann's constant
\mathbf{K}	Experimentally measured isothermal crystallization rate constant
K_k	Nucleation exponent
L^{-1}	Inverse Langevin function
λ	Draw ratio along the stretching direction
λ_c	Critical draw ratio for onset of crystallization
λ_{max}	Limiting stretch ratio on each chain
m/min.	Spinning speed in meters per minute
μ	Number of statistical segments per network chain
\mathbf{M}_s	Molar mass of the elastic subchain of the network
\tilde{N}	Number of network chains per unit volume
n	Avrami exponent
$\langle \mathbf{P}_2(\cos\theta) \rangle_{cr}$	Critical level of amorphous orientation
PET	Poly(ethylene terephthalate)
POY	Partially oriented yarns
ϕ	Ratio of the mean crystallite length to the long period
QC	Quiescent crystallization
r	Measured retardation on polarized microscope
ρ	Density of amorphous PET
ρ_o	Density of crystalline PET

SAXS	Small angle x-ray scattering
SIC	Strain- (or stress-) induced crystallization
σ	Total stress in the polymer
σ_0	Stress constant
σ_A	Stress in intermolecular resistance
σ_B	Stress in network resistance
σ_e	End surface free energy
σ_s	Lateral surface free energy
T	Temperature of crystallization or drawing
T_m^0	Equilibrium melting temperature of crystal
$t_{1/2}$	Half-time of isothermal crystallization
T_A	Intermolecular stress
T_B	Network stress
T_{c_onset}	Initial point of cold crystallization exotherm during DSC scans
T_{c_peak}	Peak point of cold crystallization exotherm during DSC scans
T_g	Glass transition temperature
T_m	Modified melting temperature
θ	Measured angle of extinction on polarized microscope
U^*	Activation energy for the segmental jump
WAXS	Wide angle x-ray scattering
x	Volume fraction crystallinity
y	Weight fraction crystallinity
Y_{lower}	Lower yield point
Y_{upper}	Upper yield point
ξ	Chain end-to-end distance of crystallite in the direction of stretch

SUMMARY

PET (polyethylene terephthalate) is usually processed at temperatures above the glass transition by some form of stretching process (film stretching, fiber drawing, blow molding). If the strain-induced crystallization (SIC) is avoided during drawing, PET fibers can be easily drawn to draw ratios larger than 10. This process is called flow-draw or superdrawing. In a superdrawing process, a polymer filament is elongated without developing significant crystallinity. Exploiting this phenomenon may bring about lower cost, more flexible and faster response in synthetic fiber production. This thesis focuses on the fundamental mechanisms of PET superdrawing, including experimental and theoretical analyses.

A comprehensive study was conducted to determine the limitations in processing conditions for superdrawing. Experimental studies were carried out by uniaxial drawing tests at temperatures from 90 to 120°C and at strain rates ranging from 0.008/s to 0.425/s. Crystallinity and orientation of the drawn samples were evaluated using differential scanning calorimetry and birefringence measurements. The results indicate that superdrawing is not possible for any strain rate at 90°C because of significant strain-induced crystallization (SIC). Between 90°C and 105°C, superdrawing occurs only when the strain rate is below a threshold value, and the allowable strain rate for superdrawing increases from less than 0.333/s to below 0.425/s as the drawing temperature increases from 105°C to 110°C. When the temperature is increased to 115°C and 120°C, however, superdrawing is only possible at strain rates higher than 0.016/s. This study also revealed

that increasing temperature from 110°C to 120°C leads to more crystallization at low strain rates (0.001/s), and less crystallization at high strain rates (0.1/s). It was shown for the first time that the mechanism of crystallinity development in PET undergoes a transition at draw temperature of 113°C and strain rate of 0.17/s.

A model was developed to predict the stress-strain behavior of PET fibers as they are drawn to very large draw ratios (up to 10) over a wide range of temperature (90-120°C) and strain rate (0.008-0.425/s). The stress-strain behavior of PET fibers under this range of conditions has not been modeled explicitly by other researchers. A one-dimensional constitutive model based on the rubber elasticity theory and non-linear viscoelasticity was used to predict the stress-strain curves of PET fibers at the aforementioned conditions. The overall stress-strain curve was constructed from the stresses arising from an intermolecular resistance (A) and a network resistance (B). The intermolecular resistance was modeled to represent the initial elastic response followed by yielding. The effect of crystallization was accounted for by increasing intermolecular resistance and increased elastic modulus of the material. The model also takes into consideration of the strain rate and temperature dependence of the time-dependent response of intermolecular resistance. The network contribution to stress, which represented the strain hardening at large strains, was quantified on the basis of conformational properties of the PET network. It was found that the dependence of the mechanical behavior on strain, strain rate and temperature in drawing of PET fibers could be adequately captured by the model.

This study sheds new light on the fundamental understanding of the PET superdrawing behavior and provides useful tools for developing a superdrawing based cost-effective fiber manufacturing process.

CHAPTER 1

INTRODUCTION

Poly (ethylene terephthalate) (PET) is one of the most widely used and commercially successful polymers, particularly used in the form of fibers and films. Its use as a commodity fiber dates back to as early as 1953. Apart from being used as fibers, PET is extensively used in industry in a semi-crystalline state to manufacture beverage bottles, films, food packaging, etc. due to its high strength, toughness and good chemical resistance. PET polymer chains comprise of repeat units with one benzene ring, two methylene units, two ethers and two carbonyl groups. The chains are arranged in crystalline regions in the triclinic form with one repeat unit per cell [1]. The *d*-spacing as observed in x-ray diffraction peaks are 5.11, 4.04 and 3.46 Å corresponding to planes with Miller indices (010), (110) and (100) respectively [2]. PET undergoes the glass transition at about 343K (80°C) and melts at around 533K (260°C).

PET is usually processed by melt extrusion followed by some form of stretching process (e.g. film stretching, fiber drawing and blow molding). The fiber drawing process involves stretching the fibers between two rolls at temperatures just above the glass transition. The drawing process is widely used for producing textile fibers as well as industrial yarns. The crystallization that follows after orientation of the molecules during a drawing process is called stress/strain-induced crystallization (SIC). This, as opposed to thermally induced crystallization, is fundamentally an orientation or entropy driven process. If the strain-induced crystallization (SIC) is avoided during drawing, PET fibers

can be easily drawn to draw ratios larger than 10. This process is called flow-drawing or superdrawing which can lead to novel and low cost processes in fiber manufacturing. Experimental studies have shown that amorphous PET can be drawn under a low tension with no measurable changes in orientation or observable crystallization at a high temperature and a low strain rate. This means the drawing can proceed to much larger strains since the hardening mechanisms are not present. The superdrawing process has a potential cost advantage in producing hollow and ultrafine fibers (*Section 2.1*).

PET has been a subject of intensive study in connection with the above mentioned applications, as well as attracted considerable attention from a viewpoint of understanding the fundamental mechanisms of crystallization. This is because it has a low enough rate of crystallization so as to allow its production in a wide range of physical states. A comprehensive review of the processing, crystallization behavior and modeling of PET is given in *Chapter 2*. A description of necking behavior and SIC (*Section 2.2*) followed by melt spinning techniques to produce the PET fibers, and their effect on the structural evolution of the final product is given (*Section 2.3*).

Numerous researchers have studied the crystallization behavior of unoriented, amorphous PET and the corresponding changes in the microstructure (*Sections 2.4, 2.5, 2.6 and 2.7*). Many previous papers focused on the morphological development and strain- (or stress-) induced crystallization during stretching of amorphous PET [3-22]. In most of the experimental and theoretical studies reported in the literature, the process conditions for occurrence of strain- (or stress-) induced crystallization and their effect on its mechanism

have been discussed [23-33]. Very little investigation, however, has been reported on the exact range of process parameters conducive to superdrawing. In particular, how the morphology of fibers develops during the superdrawing process is not completely understood. It is felt that a deeper fundamental understanding of the crystallization mechanism during superdrawing of fibers is needed. An extensive experimental work on the fiber stress-strain behavior during uniaxial extension in a large range of temperature and strain rates would enable us to determine the parameter window of superdrawing. Exploiting this phenomenon may bring about lower cost, more flexible and faster response in synthetic fiber production.

Literature review in *Chapter 2* shows that strain-induced crystallization (SIC) causes strain hardening in final stages of deformation due to polymer chain alignment, giving rise to higher overall crystalline content and thereby to increased density and flow-stress values. Moreover, it was shown that development of significant crystallinity in drawn samples occurs only after a critical level of orientation is achieved. The critical value of orientation was shown to be strongly affected by temperature and strain rate. This leads to the belief that the occurrence of SIC, whose absence results in flow-drawing, depends mainly upon temperature, strain rate and orientation. There are only a few combinations of strain rate and temperature that will lead to superdrawing.

Specific goals of this study are given in *Chapter 3*. The first main objective of this research is to elucidate the crystallization mechanisms, particularly in order to explore the regime of drawing parameters where superdrawn samples are obtained. Second main

objective is to model the large strain mechanical behavior, during superdrawing, of PET fibers in a large range of temperature and strain rates which is not covered in previous research. An experimental study was designed to observe the stress-strain behavior at a range of strain rates (0.008 to 0.425 s^{-1}) and temperatures above the glass transition (90°C - 120°C). The uniaxial tensile tests (*Section 4.2*) are followed by the thermal analysis (*Section 4.3*) and finally the orientation studies (*Section 4.4*) of drawn samples.

The existing theories in literature are reviewed concerning the modeling of the basic features of stress-strain behavior of PET, i.e., elastic response followed by yielding and finally dramatic strain-hardening (*Section 2.8*). It is shown that these strongly temperature- and strain rate- dependent features are captured by many existing constitutive models. However a model that captures the drawing behavior of fibers under superdrawing conditions (negligible crystallinity and orientation development) is not known to exist in the literature. In this study, it is attempted to develop a novel fiber drawing model that can closely predict the observed fiber stress-strain curves in the range of processing conditions of our work (*Chapter 5*). This model is built upon a combination of the molecular and phenomenological approaches.

The findings of this study lead to a determination of the boundary of superdrawing of PET fibers in terms of temperature and strain rate. A transition regime in crystallization mechanism is discovered, in the parameter range of our study, which leads us to a completely new picture of the crystallization behavior of PET fibers that has not been reported in any earlier work. The conclusions derived from experimental and modeling

results are given in *Chapter 6*. A direction for further work and recommendations for improvement upon this study are provided also in *Chapter 6*.

CHAPTER 2

LITERATURE REVIEW

PET fibers, which are generally produced by melt spinning from the polymer melt, are the most widely used synthetic material for the production of textiles. When PET is melt-processed to form products, such as fibers, it is important to control the molecular orientation and degree of crystallinity during processing so as to achieve desired physical and mechanical properties. Modulation of these properties is allowed through several processing techniques, for example, altering parameters in melt spinning processes, crystallization from the amorphous solid by heating, or further drawing of an amorphous specimen at a given constant temperature (cold or hot drawing). Among these techniques, drawing of the amorphous PET material above the glass transition temperature (T_g) is the most important one that can produce oriented crystalline material with greatly enhanced strength. The drawing conditions and type of drawing process largely determine the extent of crystallinity and orientation development, and thus the final structure of the product.

2.1 Types of drawing

2.1.1 Conventional Mechanical Drawing

Commonly PET fibers for textile and technical applications are produced by the melt spinning process. The process involves forced extrusion of the molten polymer through spinnerettes followed by cooling and solidification. The fibers melt-spun at low enough spinning speeds (less than about 3500 m/min.) are only partially oriented and known as

POY (Partially Oriented Yarn). These filaments are almost completely amorphous [19, 20, 27, 28] and therefore need to be mechanically strengthened by a subsequent hot drawing process. This mechanical drawing process leads to increased molecular alignment as well as crystallinity so as to improve the filaments' tensile strength and modulus. In this conventional drawing process the draw ratios usually obtained are in the range 3~9, because deformation at larger strain leads to a dramatic strain-hardening and causes the breakage of the yarns.

2.1.2 The Superdrawing Process

A number of experimental studies [34-37] have shown that the amorphous PET samples can be drawn under a low tension with no measurable changes in orientation or observable crystallization at a high temperature and a low strain rate. This phenomenon has been called superdrawing [21, 22, 29, 38, 39]. The superdrawing phenomenon is characterized by a negligible development of crystallinity and molecular orientation along the fiber axis as well as low axial stress level during the drawing process. Indeed, under the condition for superdrawing, a freshly melt-extruded, amorphous, polyethylene terephthalate (PET) structure such as an as-spun yarn, can be drawn up to 75 times its original length without significant orientation or crystallization. The superdrawing phenomenon is also referred to as flow drawing, amorphous drawing, or super stretching.

2.1.3 Mechanisms of Superdrawing

An accurate definition of superdrawing process in terms of structural changes and stress-strain relations has not been obtained until now. Anderson Pace [39] observed that the superdrawing phenomenon is characterized by a very slow development of crystallinity

and molecular orientation along the fiber axis as well as low axial stress level during the drawing process. It was suggested that in flow-drawn PET the macromolecular chains have some global orientation, while the local segmental orientation is negligible because of the large difference in the relaxation times of chain segments and global chains [36].

2.1.4 Advantages of Superdrawing

During this process, PET samples can be largely extended to its nearly molecular diameter enabling us to produce very fine or even microdenier fibers. Thus for PET fiber manufacturing, this superdrawing process offers a cost-effective route to manufacture fibers of very fine denier. It is known that a large percentage of the total cost of production resides in the melt-spinning phase (extrusion and solidification) of the process. The orienting or drawing operation is considerably cheaper and represents a much lower investment figure than the rather complex and expensive melt-spinning machines. A superdrawing process has the possibility of first melt-spinning fibers of large denier at low spinning speeds and then using a relatively cheap drawing process, superdrawing, to obtain any desired fineness. This is a quicker and less expensive method - employing a standard spun yarn supply from just one spinning die - than the traditional approach requiring multiple spinning dies to produce various fiber denier or finenesses. Therefore, with this process the PET fiber manufacture is more efficient and flexible than that with the traditional approach to meet customer demands for fibers with varying denier.

2.1.5 Superdrawing of hollow PET fibers

The drawing without significant crystallization can be useful in production of hollow fibers of very small deniers. The work of Aneja [40] demonstrated the use of flow drawing process for obtaining very fine hollow fibers with larger voids than those produced via melt spinning process. He used a water-based drawing process to obtain increased void content due to the effect of air expansion and water permeation. The use of two different methods was applied to produce ultralarge void fibers- one uses solvents such as methanol or ethanol to obtain final fiber voids in excess of 65%, the other uses a temperature inversion process using dry ice to give a final void content of 41.5%. A model based on a geometric technique was also proposed for the kinetics of the process. It was found that the void content rises to a steady state rapidly [41].

2.2 Typical tensile behavior of PET in an amorphous state: strain-induced crystallization (SIC) associated with necking

The drawing behavior of PET involves three stages as described by Salem [17] and Thompson [22]: The first stage consists of the extension of an amorphous network of entangled chains, in which chains slip past each other. The second stage involves the uncoiling of randomly oriented chains by continued application of stress. In this stage drawing happens at low stress-level because of physical separation of chains. In the third regime chains begin to orient in the direction of applied forces favoring strain-induced crystallization and formation of crystallite junctions which slows down entanglement slippage and results in an inflection point in the true-stress vs. strain curve. Retractable forces develop which continue to increase and finally lead to the break at UTS (ultimate

tensile strength) of the fibers. A typical stress-strain response involving necking is shown schematically in *Figure 1* below:

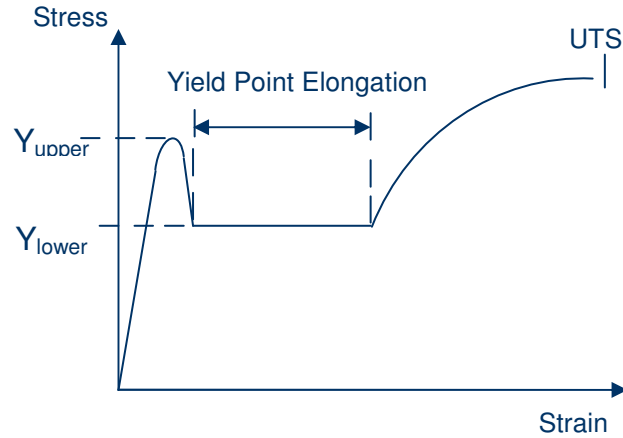


Figure 1. Different stages in the typical stress-strain response of a ductile material

Thompson suggested that since the extension in the first regime is unrecoverable on removal of stress, it is a viscous extension; whereas the second region is mainly a rubber-like or elastic deformation. PET fibers spun at speeds upto 4000 m/min. show the above mentioned yield point elongation behavior [42].

It is well known that strain-induced crystallization (SIC) causes strain hardening during deformation during which alignment of polymer chains occurs, giving rise to higher overall crystalline content and thereby to increased density and flow-stress values [33]. Shimizu et al. [42] showed that there is an inflection in the birefringence vs. density curve at 5000 m/min. suggesting that SIC starts in the spinline at spinning speeds of about 5000 m/min.

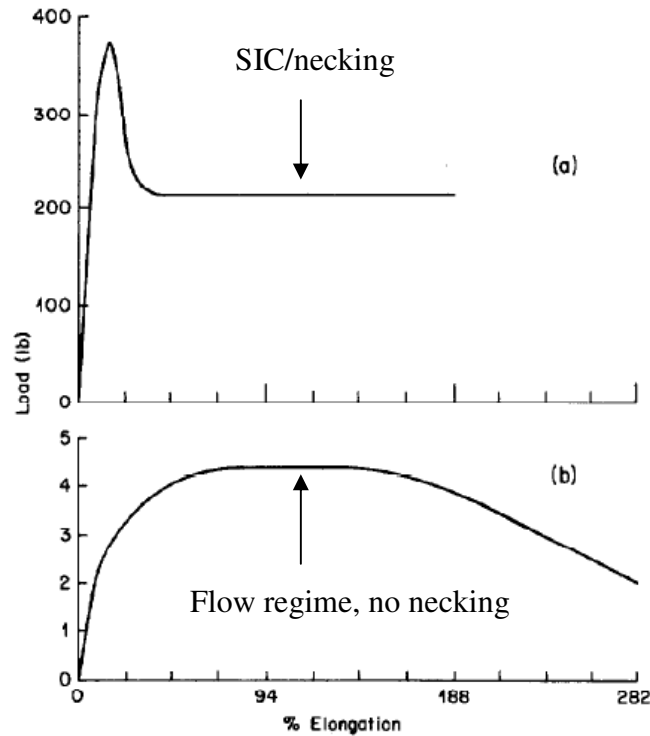


Figure 2. Load elongation curves in the two stretching regimes for PET (a) deformed below T_g and (b) deformed above T_g (From Ref. 21)

SIC has been found to be associated with necking. *Figure 2* shows that in the SIC regime necking deformation leads to rapid local straining in the neck region and thus crystallization whereas in flow regime molecules can return to random state during the extension resulting in low draw stress, little orientation and no crystallization. A uniform reduction in cross-sectional area without necking occurs in the flow regime. Spruiell et al. [21] also showed that at low strain rates flow regime can be obtained while draw at higher strain rates occurs through SIC regime.

Figure 3 shows the two deformation regimes at two different draw temperatures. The change from one regime to other, denoted by a critical strain rate, is indicated when there is a sharp rise in load or crystallinity with strain rate.

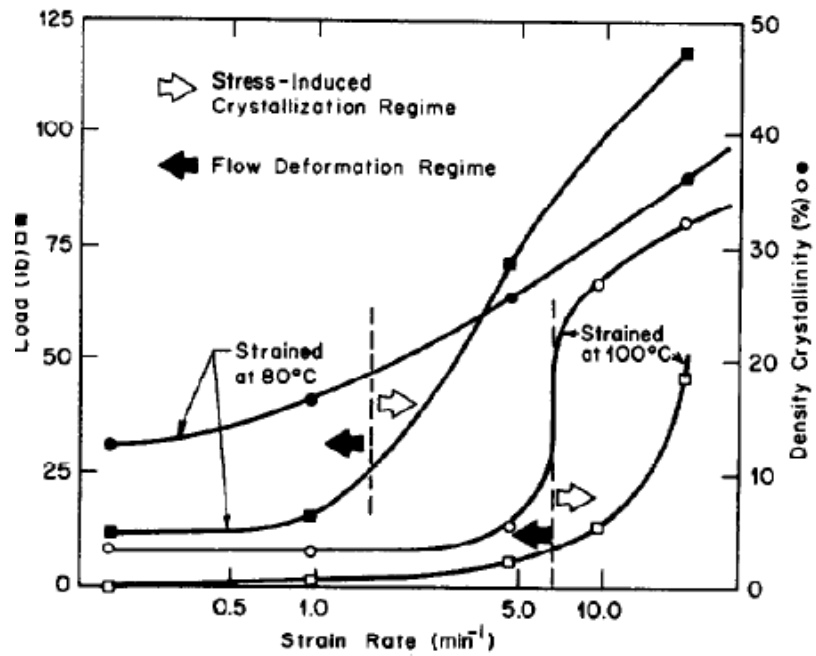


Figure 3. Variation in the draw stress and crystallinity level with strain rate at two temperatures above the glass transition (From Ref. 21)

The critical strain rate is higher at 100°C ($\cong 7 \text{ min}^{-1}$) compared to that at 80°C ($\cong 2.5 \text{ min}^{-1}$). Therefore the effect of temperature and strain rate is inter-related and complex. Whether SIC occurs or not depends strongly on the temperature and strain-rate. SIC is dependent on strain rate and temperature and it could cause rapid increase in flow stress if it takes place at fast rates [21]. A critical stress level is needed to induce crystallization which can be attained only after some critical strain rate is applied. The total amount of strain is less significant than strain rate since higher strain rate leads to increase in yield and flow stress [5].

Kawaguchi [43] explained the amorphous PET superdrawing by examining the stress-strain relationship with a mathematical viscoelastic model. It is expected that the superdrawing process will take place under plastic deformation conditions. The results of

this theoretical work are in good agreement with experiments. It was found in the experiments that for one strain rate and one draw ratio, the stress induced by strain decreases with temperature. At low temperatures and high rates of strain, the stress-strain curve is a sigmoid, indicating a finite extensibility, high molecular orientation and strain-induced crystallization. Kawaguchi also pointed out that at high temperatures and low strain rates crystallization does take place due to an increase of thermal motion. It is reasonable that the superdrawing phenomenon can only be observed in PET within an appropriate range of temperatures and rates of strain.

SIC determines the crystalline structure and orientation of the polymer after it has undergone deformation at a temperature above the glass transition. Kim et al. and Kwon et al. approached the flow-induced crystallization during deformation of PET on a thermodynamic basis [44-47]. They utilized the theory of equilibrium thermodynamics of melting to show that the equilibrium melting temperature is higher for a melt under strain because orientation causes an increase in entropy. The effect of melting point elevation was considered for calculation of crystalline orientation function frozen when the stress-induced crystallization occurred. They predicted the crystalline and amorphous contributions to the overall birefringence from the entropy change calculated using a non-linear viscoelastic constitutive equation.

2.2.1 Theoretical description of strain-induced crystallization (SIC)

The phenomenon of crystallization during deformation has been studied both theoretically [48, 49] and experimentally [50]. The experimental work has provided

evidence for dependence of crystallization kinetics [51] and morphology [52] on temperature and stretch ratio. The experimental results show that the same guiding principles that are used for quiescent crystallization can be applied in a generalized form to describe deformed crystallization [53]. Many theoretical studies that described the thermodynamics of crystallization of polymers under stress have made some assumptions about the fine crystal texture and morphology [54]. For example Flory [48] assumed the existence of only an extended-chain morphology in his paper. Wu [54] extended the work of Flory to obtain the following expression for the free energy F of a stretched polymer network:

$$F = RT \left\{ -n\lambda\theta + \frac{1}{\lambda} \left(\frac{\alpha^2}{2} + \frac{1}{\alpha} \right) + \frac{\beta^2 \xi^2}{\lambda} - \frac{2\xi\alpha\beta}{\lambda\pi^{1/2}} - \frac{3}{2} \right\} \quad (1)$$

where n is the number of free joint segments between crosslinks, ξ is the chain end-to-end distance of crystallite in the direction of stretch, α is the stretch ratio, β is defined as $(3/2n\lambda)^{1/2}$, λ is the fraction of segments between crosslinks in the amorphous phase and θ is defined as the modified melting temperature:

$$\theta = \frac{h_f}{R} \left(\frac{1}{T_m^0} - \frac{1}{T} \right) \quad (2)$$

where T is the crystallization temperature and T_m^0 is defined as h_f/s_f and is the equilibrium melting point of crystal.

According to Wu [54], the crystalline morphology is predictable based upon the above equation for free energy and analyzing the locus of its minima. For $T > T_m^0$, only extended-chain crystals are stable, while at $T < T_m^0$ the stretch ratio defines the type of

crystallites. The stable morphology is extended-chain type above a critical ratio α_c , whereas the folded-chain type is stable at stretch ratio below α_c .

Yeh reviewed the characteristics of SIC in two articles [52, 55]. The rate of SIC is rapid so that the whole process lasts only a few seconds at most. During stress relaxation, rearrangement of crystallites results in formation of chain-folded lamellae. But primary texture of SIC crystals is either fibrillar or lamellar, depending upon the stress levels during crystallization, since amount of stress decides the molecular orientation and their parallel arrangement with other crystallites. A “shish-kebab” structure that has been observed in SIC consists of a folded-chain morphology on top of an extended-chain structure. It has been shown in most polymer systems such as glasses, rubbers, polyethylene etc. that the basic crystalline units have very limited thicknesses along the stretch directions. The melting point elevation in such systems has been also studied and found to be up to 50-100°C higher than the equilibrium melting points of the isotropic polymer.

Gaylord et al. [56] presented a thermodynamic theory for SIC based upon the minimization of free energy of a crystallite. They explained the change in crystal morphology from folded-chain to extended-chain on the basis of entropic changes in the ‘amorphous sections of crystallizing chains’. They also qualitatively explained the initial stress decay and final upturn during crystallization and the reduction in the c -axis orientation of crystals, all as a function of stretch. Their assumption was that crystallization proceeds along a ‘lowest free energy path’, which minimizes the free

energy of the network at a given level of crystallinity, irrespective of the crystal morphology. In another paper Gaylord proposed a non-Gaussian theory of the stress-induced crystallization of polymeric networks [57]. Thus the finite chain extensibility was also accounted for unlike the Gaussian theory. For affine deformation of a polymer chain (with a non-Gaussian distribution function) undergoing isothermal crystallization they identified three contributions to the total free energy: free energy change due to transferring links from amorphous region to crystallite, entropy change in the remaining links of amorphous chain and interfacial free energies at the boundary of crystalline and amorphous regions. They were able to predict the initial crystallization rate, birefringence behavior and incipient melting temperature for polyethylene based on this theory.

2.3 Structure evolution in PET fiber extrusion – effect of spinning conditions

Fiber spinning involves the extrusion of molten polymer through small orifices followed by cooling and then pulling the resulting fibers by a take-up device at a speed, called the spinning speed, which is higher than the exit speed at the orifice. The fibers thus formed are subsequently drawn and oriented to impart desirable mechanical properties. The stage when the fibers are being melt-spun has a considerable effect on the fiber structure and orientation development. Therefore it is possible to obtain a wide range of orientation and crystallinities in the spun samples by varying the conditions such as spinning speed, take-up speed, cooling air velocity profile etc.

2.3.1 Differences between conventional and high-speed spinning

The spinning speeds involved in the process of melt spinning increased only gradually: from 500-1000 m/min. in the early 1950s to 3000-4000 m/min. in the early 1970s [58].

However the potential advantages of high spinning speeds, such as increased productivity and elimination of drawing step to obtain fully oriented yarns, led to a lot of research in the area of high-speed spinning. Producing fibers at high spinning-speeds involves very high spinline stresses (up to 50% of the plasticity limit for a solid polymer) and cooling times approaching 10^{-4} seconds range, thus leading to extreme conditions of fiber structural development. Many classical theories, such as nucleation rate theory of crystallization, fail under these harsh conditions of fiber formation. This requires new basic theoretical research for phenomena of spinline crystallization and spinning dynamics. The earliest evidence of high-speed spinning in the literature appeared in the 1950s [58]. By the late 1970s and early 1980s many studies of fibers spun at spinning speeds of 6000-7300 m/min. were reported in papers [19, 27].

High spinning speeds bring new elements to the melt spinning process. At high speeds spinline dynamics are influenced by inertia and air drag, unlike at low spinning speeds where constant winding tension is dominant. Fibers spun at “low” spinning speeds are only partially oriented and, in case of a slowly crystallizing polymer such as PET, amorphous. Whereas in high-speed spinning the levels of molecular orientation reached are high enough to generate spinline crystallization that yields crystalline fibers [59]. However, too high spinning speeds lead not only to excessive filament breaks, but also poor mechanical properties (owing to reduced crystallinity and orientation) of the as-spun fibers. Filament breakage during high-speed spinning has been attributed to high stress concentrations caused by high tension as well as to the differential birefringence between the skin and the core caused by fast cooling [60].

2.3.2 High-speed spun fibers: a brief overview

The first systematic study of structural changes in PET as a function of spinning speed is due to Heuvel et al. [27] which contains detailed analysis of x-ray diffraction measurements. The properties of high-speed spun yarns are different from conventional spun yarns due to the considerable differences in their fine structure. High-speed spun fibers are crystalline. Their dyeability is significantly higher relative to conventional spun and drawn fibers. They exhibit a pronounced skin-core structure (higher birefringence at the surface than at the center of a single fiber) which can be minimized by increasing the temperature of the spinline surface. A large temperature gradient across the filaments caused by rapid cooling rates may cause the radial variations in fiber structure [60]. The SAXS and WAXS studies on high-speed spun fibers showed that although crystal size increased in the spun fibers, there are large “packets” of amorphous material with nuclei dispersed in it. This may be the reason why spun fibers show enhanced draw-texturability and dyeability without the need of a carrier agent at boil. Although the tenacity of the high-speed spun yarn was similar to that of a conventional drawn yarn, its amorphous orientation was found to be lower [59]. Interestingly a lower orientation of amorphous phase in the high-speed spun yarns has been cited as the main reason for their inferior mechanical properties such as lower elastic modulus and lower yield stress relative to conventional spun-and-then-drawn yarns [60].

2.3.3 Physical properties of fibers as a function of spinning speed

It was reported that the yarn density increases with increasing speed while the boiling shrinkage decreases indicating an increasing crystallinity with spinning speed. Similarly the tenacity, the sonic modulus and the overall birefringence were found to increase with

speed. Beyond a speed of about 6500 m/min. the yarn density, tenacity and birefringence were found to decline gradually. This might be attributed to development of microvoids above this speed [59].

Shimizu et al. showed that for as spun PET filaments spun at a speed of 1000-8000 m/min., there is a significant effect of the spinning take-up velocity on the properties [19]. The X-ray diffraction patterns showed clearly that significantly large crystals are present only in the samples spun above 4000 m/min. The degree of crystallization and molecular orientation leveled-off beyond the speed of 6000 m/min. In another work they found that molecular weight affects the orientation and crystallization behavior of PET for high speeds of spinning [20]. The birefringence decreased after about 7000 m/min. for all molecular weights studied (1.84, 20.5 and 29.8 kg/mol). It was shown that the tenacity increased linearly with speed while the Young's modulus dramatically increased for speeds above 4000 m/min. [42]. Boiling shrinkage was found to decrease for speeds above 3000 m/min. In a study of PET spun in the speed range of 5000 to 9000 m/min. all three crystallite dimensions of PET showed a monotonous increase with increasing velocity, but the crystal density decreased for speeds higher than 7000 m/min. [61].

Heuvel et al. [27] performed a study on PET involving spinning speeds of 2000 to 6000 m/min. and structural analysis tools such as WAXS, DSC, SAXS, IR spectroscopy and pulse propagation. The cold crystallization peaks in the DSC trace shifted towards lower temperatures with increasing spinning speeds and disappeared at speeds above 5000 m/min. The change in the shape of the melting peak started at 4000 m/min. The increase

in melting peak temperature was correlated with large crystallites formed in the spinline. Their x-ray diffraction experiments showed that only speeds higher than 4000 m/min. resulted in any significant crystallinity development in the spun fibers. The structure formed at low speeds (up to about 4500 m/min.) is mainly amorphous with no or very little orientation. Other physical properties such as density, sonic modulus and amorphous orientation factor were all shown to rise with increasing spinning speed and all displayed a sharp upturn at about 4000 m/min. Heuvel and Huisman [62] also proposed the presence of mainly *trans* conformations in a crystalline region of PET based upon the steric hindrance factors. Similarly a large amount of *gauche* sequences are expected in amorphous molecules since they consist of unoriented coiled polymer chains. With increasing spinning speed, the *gauche* content is expected to decrease since uncoiling of molecules occurs with the orientation process. Their IR experiments on PET spun at 2000-6000 m/min. showed some evidence for this theory.

The effect of initial take-up speed on the structure and properties of PET filaments was also studied in detail by Hotter et al. [28]. The variation of thermal, mechanical and other properties of the as-spun fibers with spinning speed was determined. As shown in *Figure 4*, the crystallinity essentially increased only after the speed range 2500 to 3750 m/min., while the birefringence increased almost linearly with increasing take-up speed. Similarly the tenacity of the as-spun filaments was found to increase in a linear fashion with increasing speed, while the elongation at break decreased much more rapidly.

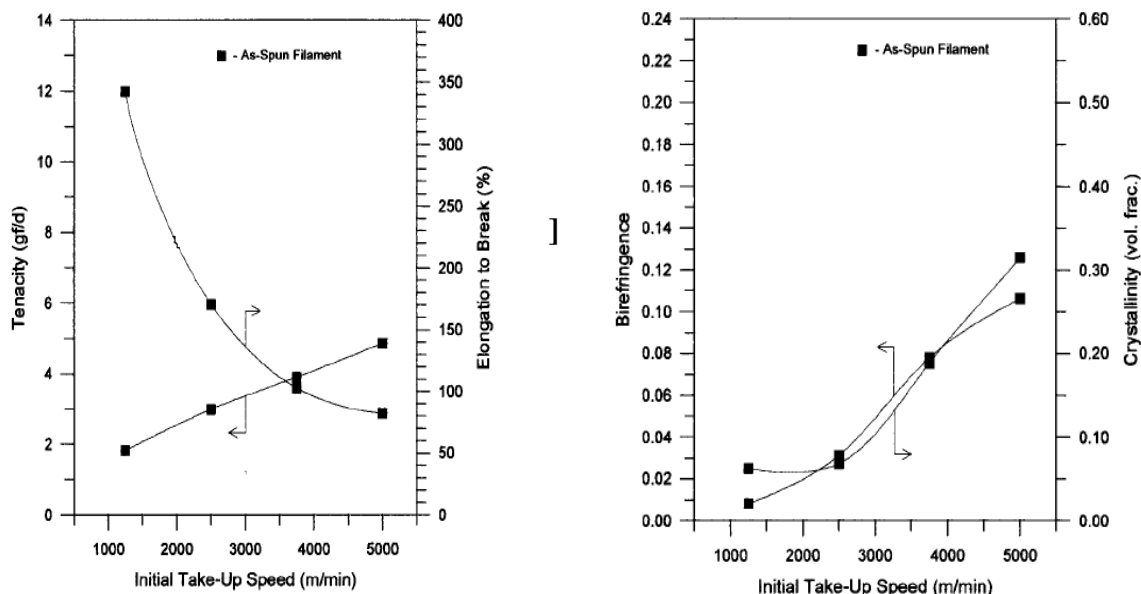


Figure 4. Effect of strain rates (or take-up speed) on the mechanical and optical properties of PET fibers (From Ref. 28)

The changes in orientation and crystallinity with spinning speed were studied from the XRD studies by Hotter et al.. As shown in *Figure 5*, the amorphous halo at low speeds becomes more and more sharp along the equator, and some off-equator reflections also appear with increasing spinning speed of the filaments. This is clearly a strong indication that the structure of as-spun PET fibers is almost totally amorphous at low speeds (until about 4000 m/min.). A well developed crystalline structure appears only at speeds higher than 5000 m/min.

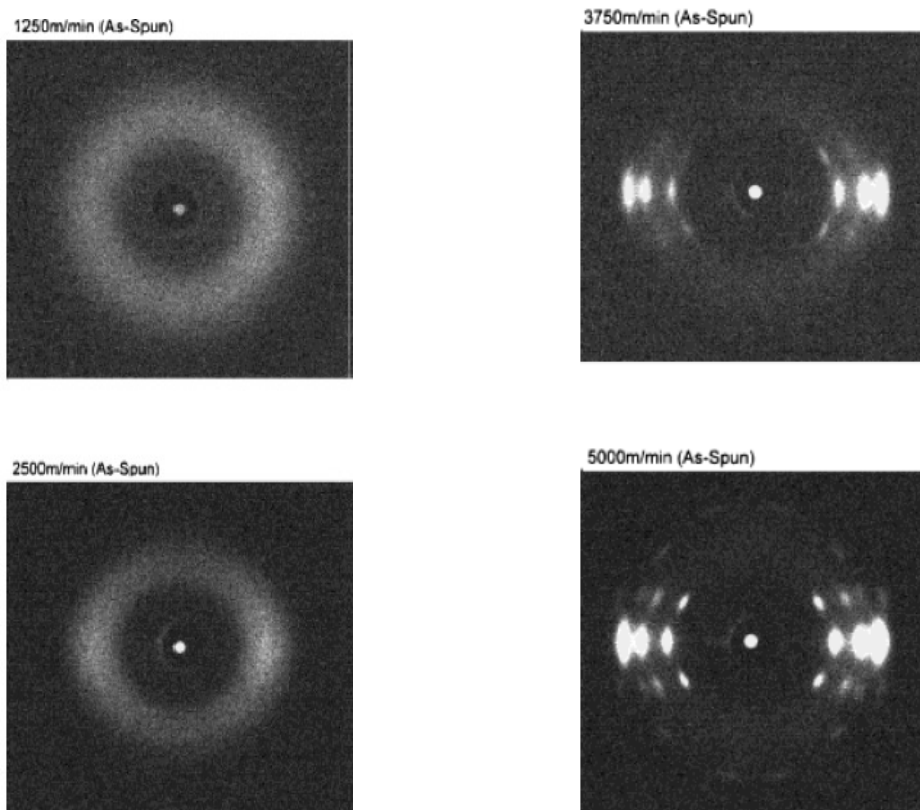


Figure 5. WAXS photographs of as-spun PET fibers (From Ref. 28)

According to Hotter et al. the molecular chains within the less oriented amorphous regions that connect the more rigid crystalline blocks are known as “tie molecules”. The number and distribution of lengths of these tie molecules may affect the tensile properties of the filament. The improvement in tensile properties of as-spun filaments with increasing take-up speed may be attributed to either an increase in these tie molecules or to an increase in the crystalline volume fraction of the material.

Yasuda [63] systematically studied the variation in elongation-at-break, tenacity, specific gravity, shrinkage and birefringence of as-spun PET filaments as a function of the take-up speed. The tenacity, density and birefringence were found to increase with increasing

speed while the shrinkage and breaking elongation decreased. From the abrupt increase in density and sharp decrease in boiling shrinkage at a speed of 4500 m/min., they also concluded that filaments with higher density and well-defined crystalline morphology are formed at speeds greater than 4500 m/min. A stabilized and more oriented structure formed due to spinline crystallization leads to a drop in shrinkage with increasing spinning speed. Their x-ray diffraction studies showed that the apparent crystal size in fibers spun at speeds higher than 4500 m/min. was about two times than that in a conventional spun-drawn filament.

Vassilatos et al. experimentally studied the spinning of PET between 2500 m/min. and 9000 m/min. They found that the SAXS pattern of high-speed spun fibers showed a four-point pattern until 6750 m/min. but changed to a meridional pattern for higher speeds. This was explained on the basis of ceased growth of primary crystals and additional crystals being formed from the existing nuclei thus leading to a decrease in the long-period spacing [59].

2.3.4 Mechanisms of development of superstructure of as-spun fibers

From the results of experimental studies on PET fibers spun at different speeds it has been possible to develop a picture of the morphology and fine structure of as-spun fibers as it forms in the spinline. The fiber diameter begins to decrease immediately upon exiting the orifice in the unoriented state [61]. As deformation progresses the oriented mesophase appears due to molecules being oriented along the fiber axis. Farther down the spinline the necklike deformation appears at a point whose position is not precisely

known. After the necking zone is passed, the diameter change ceases to occur leading to a high molecular orientation and high degree of crystallinity in the fiber.

As shown in *Figure 6*, fibers consist of essentially amorphous regions of unoriented molecules at a speed of 2000 m/min. [27]. Increasing the speed up to 3500 m/min. results in only an increased orientation with no significant crystallization. As take-up speeds are increased more, some apparent crystallization develops, whereas beyond the speed of 5000 m/min. very well developed crystalline regions with higher orientation are formed.

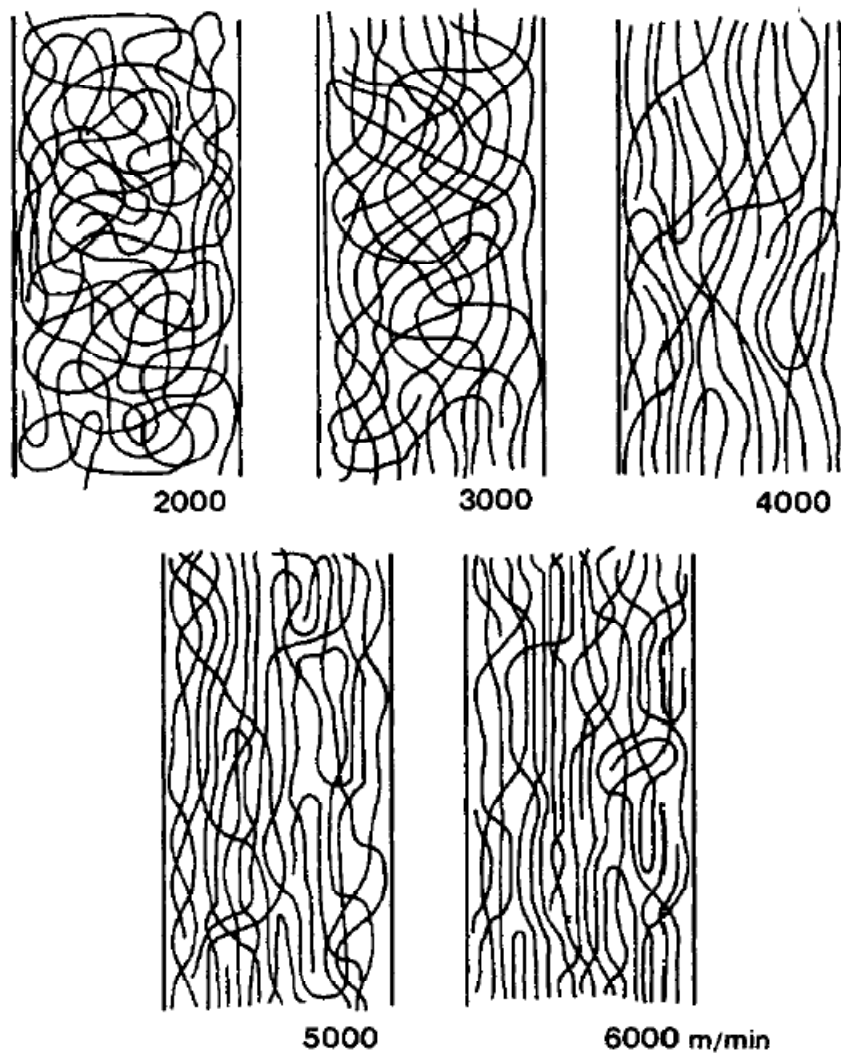


Figure 6. Effect of take-up speed on the morphological development of PET fibers (From Ref. 27)

2.3.5 Molecular orientation and flow-induced crystallization in high-speed spinning

From the numerous experimental studies involving PET, it is clearly evident that the crystallization occurring at higher spinning speeds is much faster than that for quiescent crystallization process. The crystallization rate in the high-speed spinning line (4000-6000 m/min.) has been estimated to be about 10^3 - 10^5 times faster than under no take-up.

This has been attributed to the effect of orientation and high stresses attainable at high speeds [58].

Higher orientation promotes the formation of parallel ‘bundles’ of chains. Therefore the oriented melt probably consists of bigger and more regions of ordered polymer molecules, leading to easier crystallization [62]. Heuvel et al. argued that such large bundles of ordered molecules can act as nucleation sites even at very low supercooling (close to melting temperature) because the critical temperature is higher for larger nuclei. For yarns spun at 6000 m/min., the large bundles can nucleate and grow over the entire temperature range of supercooling from below T_m to near the T_g . As spinning speed decreases the size of bundles becomes smaller and the supercooling range, in which crystal growth can occur, shrinks. Thus the smaller speeds lead to formation of smaller crystals with poorer orientation as compared to those formed at large speeds. More molecular orientation also leads to higher degree of supercooling resulting in a large increase in the rate of crystallization. The degree of crystallinity achieved in as-spun filaments is primarily affected by spinning speed and filament radius [58].

George et al. [64] studied the thermodynamics and kinematics of spinline crystallization of PET spun at 3000-6000 m/min. According to George, classical nucleation rate theory is unable to explain the non-isothermal and time-dependent crystallization behavior at high speeds. They proposed an alternative “nucleative collapse” theory which involves a homogeneous transformation across the material at a faster rate than nucleation and growth [65]. This mechanism becomes effective when the critical nucleus size is on the

order of crystal unit cell dimensions, due to the presence of high stresses and high supercooling.

2.3.6 Necking deformation in high-speed spinning

It has been widely recognized that the concentrated (or neck-like) deformation occurring in high-speed spinning of PET melts (take-up speeds > 5000 m/min.) gives rise to high tensile stresses that lead to flow- or strain-induced crystallization. The fiber diameter becomes almost constant after the necking point. The effects of necking deformation in high-speed spinning have been studied qualitatively but a satisfactory quantitative prediction of necking behavior is lacking. This may be because in a high-speed spinning line fiber cross-section changes continuously depending upon speed, cooling intensity etc. Thus there is no sharp definition of a neck point in a continuous spinning line [58]. The necking of solid polymers is observed mainly at infinitesimally small deformation rates and in nearly isothermal conditions. However the necking during high-speed spinning is apparently dominated by dynamic, not static, behavior of the polymer.

It has been proposed that the heat released during crystallization causing a local temperature elevation in the necking region might lead to a decrease in elongational viscosity and result in a neck-like deformation. Another reason for occurrence of necking has been speculated to be the existence of an ordered ‘mesophase’ which is responsible for a reduction in elongational viscosity. According to Ziabicki [58] necking intensity is higher if the axial gradient of elongational viscosity in the crystallization zone is higher. Also the inertia and air drag both reduce the necking effect.

Doufas [66, 67] and McHugh [68, 69] gave a constitutive description of the kinetics of SIC by modeling the melt as a modified Giesekus fluid and the solidified phase as orienting rigid rods. Their predictions from the model were close to experimental observations. According to this model the elongational viscosity sharply falls after reaching an initial peak, then again rises due to SIC. Since there is no temperature rise predicted under these conditions, they concluded that necking is caused by decrease in elongational viscosity.

It has been conclusively shown in some experimental works that occurrence of strain-induced crystallization results in large gains in the spinline viscosity leading to rapid solidification. Also big upturns in the density and birefringence are observed due to this phenomenon. But there has been disagreement about whether the strain-induced crystallization happens before necking or after it. It is widely acknowledged that necking happens before crystallization. The necking phenomenon and its effects on spinline clearly demonstrate that the PET melt behavior is strongly non-linear and can not be precisely modeled with single Newtonian or linear viscoelastic equations.

Shimizu et al. experimentally studied the necking phenomenon of PET filaments spun at speeds of 3000-6000 m/min. Neck-like deformation started at 4000 m/min. and was distinct at 5000 m/min. [61]. The position of the 'neck-point' in the spinline shifts towards the orifice with increasing speed, whereas increasing throughput (mass flow per unit time) causes neck-point to move to the take-up device. The intensity of necking also decreased with increasing mass flow.

2.4 Crystallization behavior during drawing

The stress-strain response of PET during deformation will obviously be a function of the conformational and configurational changes in its microstructure. So we look at the fundamental processes during the deformation of PET. The hot drawing process involves deformation of the polymer at a temperature above the glass-transition. The intrinsic structural features and the associated properties of the polymer will determine the response to strain of the polymer [18]. The structural description of a semicrystalline polymeric material is generally afforded by the typical two phase model: the crystalline and amorphous phases. The crystalline phase is present as rigid blocks dispersed within a sea or matrix of a “soft” amorphous material. This phase acts as physical cross-links which bind the whole structure together.

2.4.1 Important processes during drawing

The basic molecular changes occurring during a drawing process are listed below.

- a) Orientation by applied force~ $f(\dot{\epsilon})$
- b) Molecular relaxation or disorientation by random thermal motion~ $f(T)$
- c) Thermal crystallization~ $f(T)$
- d) Strain-induced crystallization (SIC) by alignment of polymer chains~ $f(\text{net orientation})$

Note that since net orientation is a factor of T and $\dot{\epsilon}$, SIC is expected to depend on T and $\dot{\epsilon}$.

It is apparent that the strain rate $\dot{\epsilon}$ and temperature T are the most significant factors [21, 33]. The magnitude of net orientation and orientation-induced crystallization is controlled

by the time available for the molecules to relax which, in turn, depends upon the rate of deformation as well as the temperature. It is worth noting that SIC differs from isothermal crystallization in its origin and kinetics [8]. Strain-induced crystallization has been found in numerous morphological studies to be largely dependent upon entropic factors due to the orientation of the material.

Strain rate affects the time available for disorientation of molecules, whereas draw temperature affects both the rate of crystallization and molecular relaxation. Although the effects of temperature and strain rate are extremely complex because of the close correlation, clearly the critical factor is the relative magnitude of the rates of molecular relaxation and strain-induced crystallization. Thus focusing on the two factors – T and $\dot{\epsilon}$, we can further elaborate the crystallization process during drawing of PET fibers. It's our goal to determine the conditions where crystallization - due to high temperature exposure or due to strain-induced (SIC) - is kept to a minimum level during drawing of PET.

2.5 Aspects of stress-strain behavior of PET

Now the experimentally observed effects of temperature and strain rate on crystallinity development in PET, as described in the previous works, will be studied.

2.5.1 Role of Temperature

2.5.1.1 Drawing under T_g (Cold Drawing)

Napolitano et al. [12, 13] and Allison and Ward [23] showed that cold drawing of amorphous PET fibers involves a strain-induced crystallization occurring with

simultaneously increasing orientation of both the crystalline and amorphous phases. Weakening of the glass transition peak and its finally being obscured by the cold crystallization exotherm with increasing draw ratio was observed in the DSC traces as shown in *Figure 7*. A heterogeneous molecular network with very small imperfect crystals was proposed to model the structure of the fibers spun at this speed range.

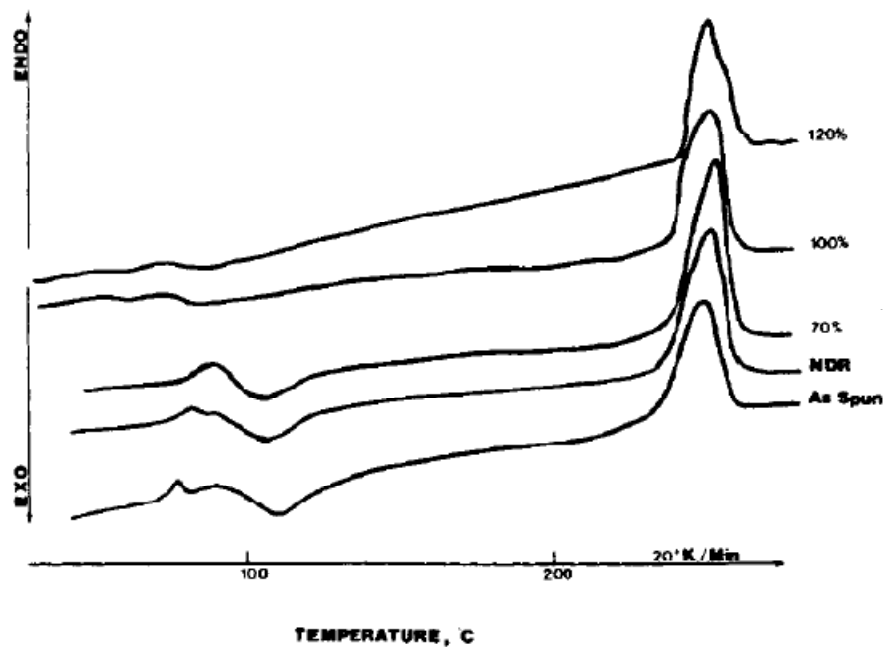


Figure 7. DSC thermograms at 20°C/min of PET fibers drawn to different draw ratios (From Ref. 12)

Similar studies by DSC of the cold crystallization behavior of PET have been done by others [70-72]. Interestingly Napolitano et al. could observe three distinct regions in the stress-strain behavior at room temperature. An initial Hookean region at very low elongations was followed by yielding whereby multiple necking was observed. Then a single continuous neck propagates through the fibers at a constant load. Finally a sharp

increase in the load at the natural draw ratio leads to strain hardening until failure. This behavior is similar to the proposed mechanism for necking of an amorphous PET fiber. The initial modulus of the fibers increased monotonically with draw ratio. The birefringence was found to increase from an as-spun value of 0.0415 to a limiting value of 0.20. Though no specific details were given in Napolitano et al.'s work about the molecular network, the mechanism of extension of a molecular network was successfully applied to account for optical and mechanical anisotropy development in drawn fibers by Allison et al. [23].

Spruiell et al. [21] found that stress-strain response of PET drawn below glass transition consisted of yield followed by necking. The crystallinity increased with strain rate but did not change with temperature below the T_g . Shirataki et al. [73] performed cold drawing on PET fibers with a wide range of molecular orientation and crystallinity levels in a temperature-controlled water bath. They used the network draw ratio to uniquely characterize the molecular network of PET as well as its tensile properties during cold drawing. They showed that the stretching behavior of the intrinsic PET network at room temperature is similar to extension of an ideal rubber network irrespective of the initial level of molecular orientation.

In another work Misra et al. [2] analyzed the microstructure development of PET films during uniaxial stretching both below and above the glass transition using small angle light scattering (SALS), optical microscopy, wide angle X-ray scattering (WAXS), birefringence and crystallinity (density gradient column). The samples drawn below T_g

were shown to have a necking region with high crystallinity and orientation. A high degree of internal stress remained in the sample drawn below T_g , which cannot be relaxed owing to low molecular mobility. Their small-angle light scattering and optical microscopy results showed that cold drawing produces a 'rodlike superstructure in which the rods are preferentially oriented in the stretching direction'. They showed that annealing under tension does not affect the rodlike superstructure and extended-chain crystallites. However, during free annealing, ellipsoidal spherulites nucleate along the long axis of each rod and produce rows of ellipsoids. Annealing the necked portions of the samples that were stretched to 200% below T_g (25°C) resulted in considerable crystallinity. Wide-angle x-ray patterns obtained for undrawn and drawn PET films, as shown in *Figure 8*, clearly demonstrated the increase in orientation and crystallinity with cold drawing and annealing.

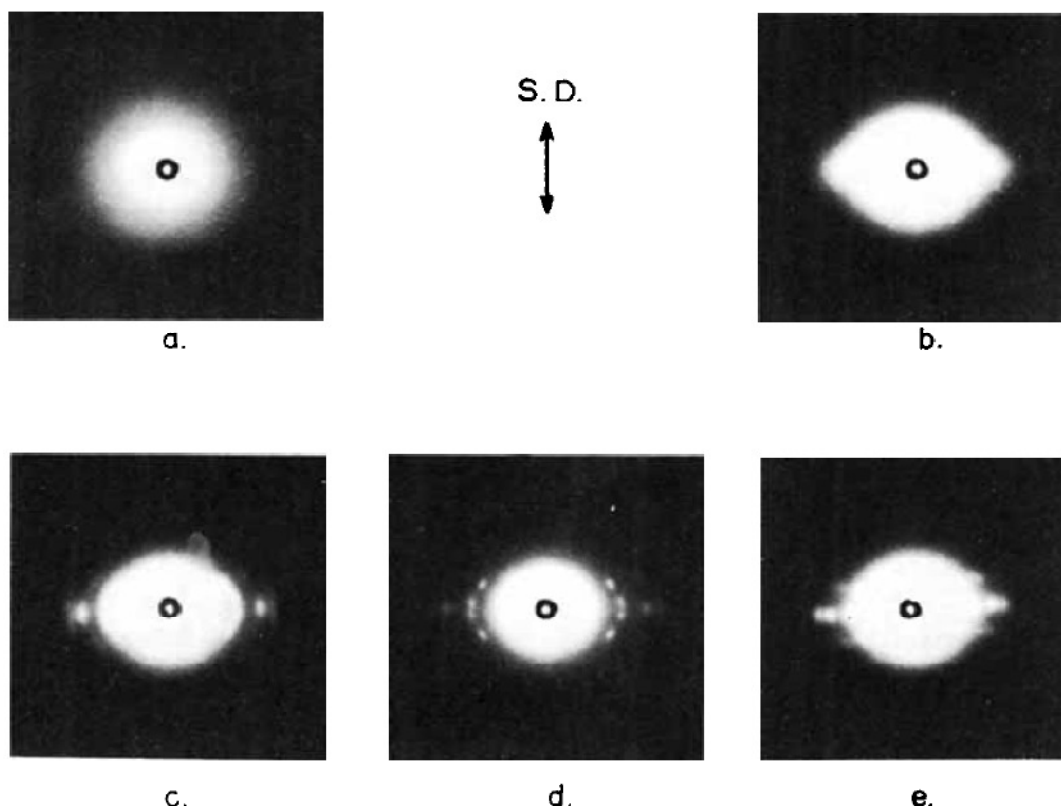


Figure 8. Wide-angle x-ray patterns of (a) Amorphous; (b) Cold-drawn (necked portion); (c) Cold-drawn sample annealed at 140°C for 10 min at constant length; (d) Cold-drawn sample annealed at 140°C for 10 min without constraint; (e) Cold-drawn sample stretched another 20% at 90°C (From Ref. 2)

2.5.1.2 Drawing above T_g (Hot Drawing)

A large number of studies have been done on the effect of high deformation temperatures on the orientation and crystallization behavior of PET. It has been proposed [35] that above a critical temperature, the intermolecular forces no longer exist, resulting in slipping of polymer chains past each other and flowing individually, such that even a very large deformation does not cause any molecular orientation and crystallization just like the flow of a simple liquid. Peszkin et al. [14] showed that increasing the temperature reduces the crystallization half-time ($t_{1/2}$) rapidly and orientation of the amorphous phase

is an important factor. High temperatures around 200°C lead to crystallization half-time of about 50 milliseconds. Thus thermal crystallization effects are expected to be more pronounced at higher temperatures.

Misra et al. in their study showed that for the samples tested above T_g and subsequently quenched to 0°C, crystallinity was found to increase considerably after a strain of 0.8 at a test temperature of 80°C and a strain rate of 300% min⁻¹. The WAXS patterns (see *Figure 9*) indicate that at low elongations PET has a rodlike superstructure that is oriented transversely to stretching direction, but does not contribute to crystallinity. However for larger strains the rods change into ‘ellipsoidal spherulites’ which are elongated along the direction normal to stretching.

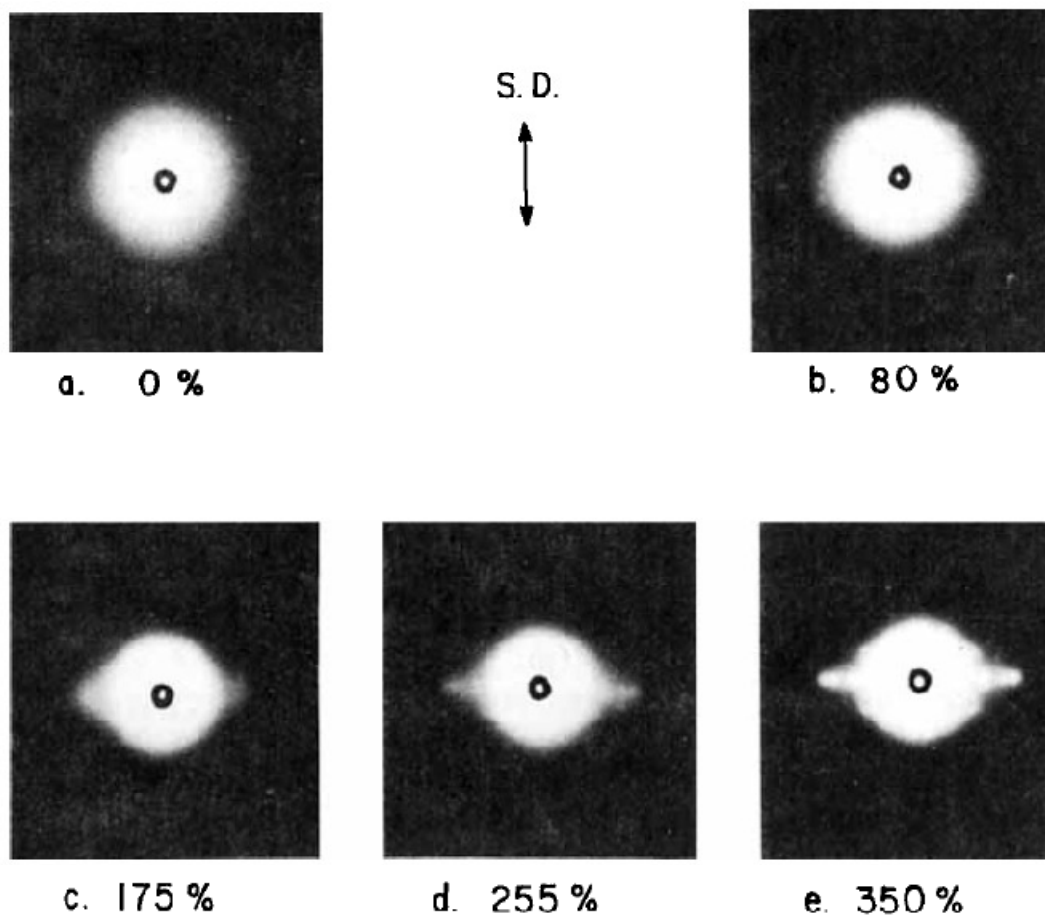


Figure 9. Wide-angle x-ray diffraction patterns for PET stretched at 80°C to different strains: (a) undrawn, 0%; (b) 80%; (c) 175%; (d) 255%; (e) 250% (From Ref. 2)

Mahendrasingam et al. [10, 11] studied the changes in orientation and nature of strain-induced crystallization during uniaxial drawing of amorphous PET films. In their draw experiments at high strain-rates ($\sim 10 \text{ s}^{-1}$), several draw ratios and various temperatures between 85 and 130°C found that it is required to reach a certain critical level of chain orientation for SIC to occur. The critical value depends upon draw temperature. At temperatures greater than 125°C, fast molecular relaxation prevents significant strain-induced crystallization. SIC occurred only in drawing at temperatures below 125°C since it was much faster than isothermal crystallization.

In similar work Spruiell et al. [21] studied the crystallization behavior of PET as a function of deformation conditions. They found that increasing temperature reduced the development of crystallinity in the deformed sample, but only at smaller strain rates. It was shown that a flow draw above glass transition temperature without necking is possible at low strain rates (also see *Figures 2 and 3*). If the strain-rate is sufficient to induce a critical stress level on the molecules, necking accompanied by crystallization and high degree of orientation occurs at that draw temperature. More importantly they found that the critical strain rate was lower at lower temperature.

This shows that the interactions of temperature and strain-rate during the drawing process are extremely complex. As it will be shown in the following section, they profoundly affect the stress-strain behavior of PET during drawing. We will consider the studies by other researchers of the effects of temperature on PET in two regimes- ‘low’ strain rates and ‘high’ strain rates. The precise definition of ‘low’ and ‘high’ shall be considered later in this section.

2.5.1.3 Effect of temperature - strain rate regimes

The effect of temperature is invariably superimposed with the effect of strain-rate. Therefore the deformation process should be considered as a combination of those two critical factors: temperature and time-scale of deformation. The second factor is the same as the strain rate or speed of testing.

Salem [15, 17, 31, 32] has done extensive studies on the drawing behavior of amorphous PET films. He found that at lower strain rates (less than $\sim 1 \text{ s}^{-1}$) increasing temperature

delays the onset of crystallization to higher draw ratios. Two crystallization regimes during draw were identified by Salem: First in which crystallinity increases faster and draw stress increases slowly. In the second regime, rate of crystallinity increase is much slower. In either of regimes the rate of crystallization depends upon the draw temperature. Except at a strain rate of 1 s^{-1} , the relationship between the two is non-linear. At higher strain rates, the opposite is observed i.e. the critical orientation for crystallization is decreased. At temperatures below T_g only the strain rate comes in to play- with almost negligible role of temperature. So a higher stretching speed, which allows molecules less time to relax back to the random configuration after they are once aligned under stress, causes an increase in crystallinity of the tested sample. As temperature is increased above the glass transition, higher temperature reduces the critical orientation required for inducing crystallization by way of increasing both the molecular relaxation and crystallization rates at a given level of amorphous orientation. As shown in *Figure 10*, when strain-rates are in the smaller range there is sufficient time available for relaxation; higher temperatures are more effective at reducing the rate of crystallization. At high strain rates time for relaxation is short and therefore crystallization dominates. So there is a decrease in critical draw ratio for onset of crystallization (λ_c) with increasing temperature.

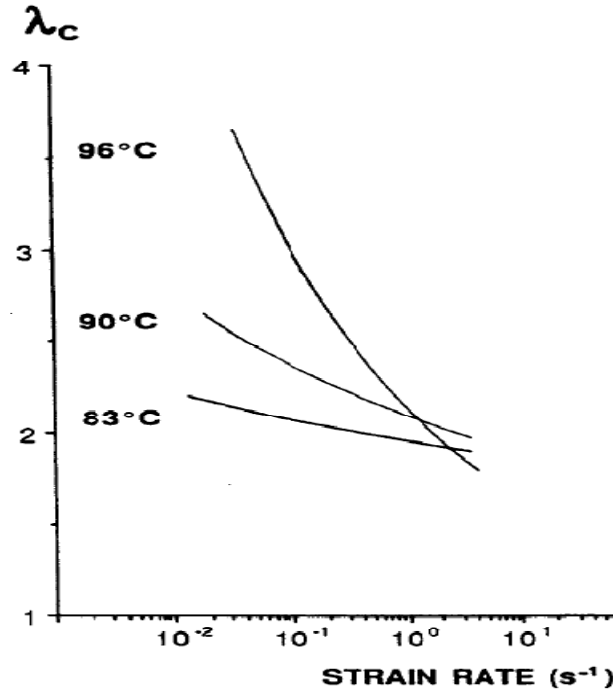


Figure 10. Critical draw ratio for onset of strain-induced crystallization versus strain in different strain rate regimes (From Ref. 17)

The competition between molecular relaxation and crystallization during drawing of PET, as mentioned in the previous section, becomes apparent at high strain rates ($> 1 \text{ s}^{-1}$) and has been discussed by Peszkin et al. [14] and Hamidi et al. [6].

2.5.2 Role of strain rate

Since the effects of strain rate and temperature on PET stress-strain behavior are well known to be mixed or dependent on each other, the description in this section closely follows that in the previous one.

For PET strain rate has a significant effect on crystalline content even at low rates. At a given temperature if we increase the strain rate the time available for relaxation becomes short and molecules have to get aligned in the stretch direction favoring crystallization

and hence crystallinity increases. By similar reasoning i.e. the time-dependence of orientation development causes strain-rate dependence of crystallization onset- we can expect that onset of crystallization will shift to lower draw ratios with increasing strain rates at a given draw temperature; since a certain molecular orientation is required to induce crystallization and the molecular relaxation would become less effective than crystallization at high rates.

Salem [17] studied the constant rate extension of amorphous PET films at strain rates in the range $0.01\text{-}2.1\text{ s}^{-1}$ and temperatures of $83\text{-}90\text{-}96^{\circ}\text{C}$. It was shown that crystallinity increased with draw ratio and strain-rates as shown in *Figure 11*. Interestingly he found that two regimes of crystallinity development were obtained at various strain rates. In the low stress regime (I) increase in crystallinity is fast and draw stress slowly rises with draw ratio. In the high-stress regime (II) crystallinity grows slowly in comparison to draw stress.

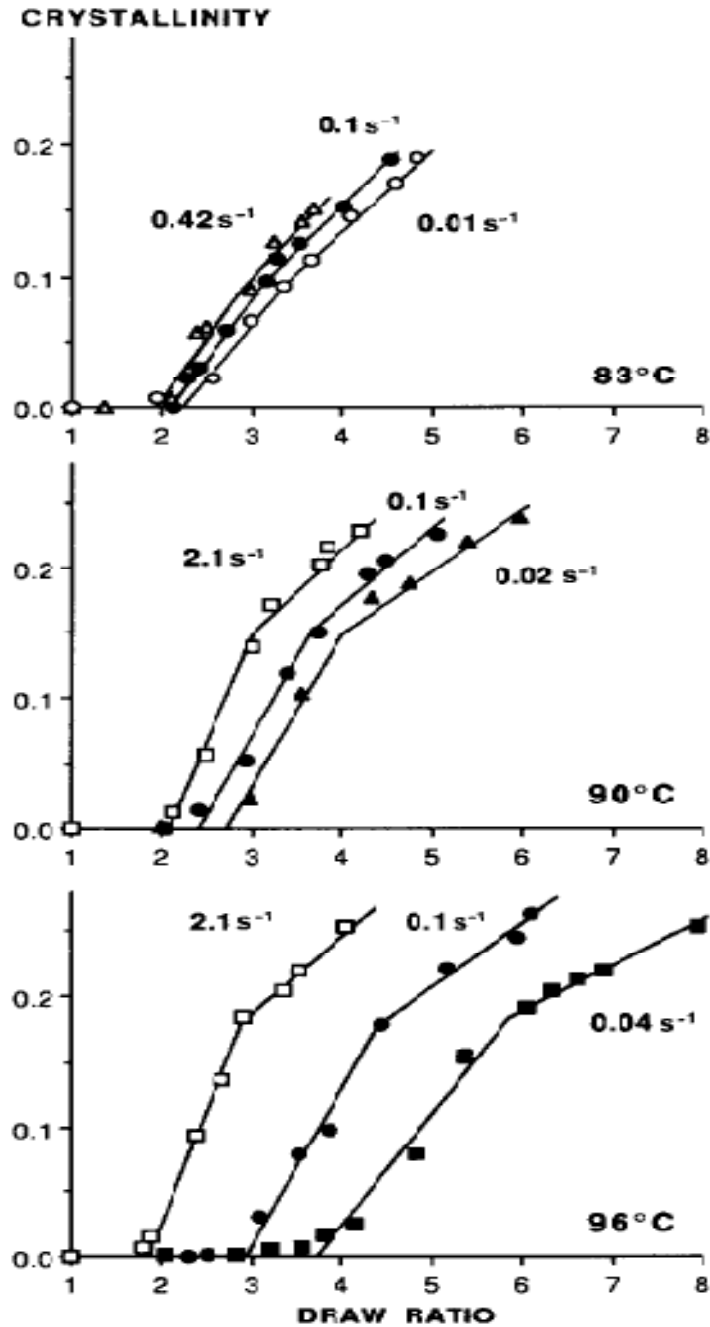


Figure 11. Crystallinity versus draw ratio at different temperatures and strain rates (From Ref. 15)

Salem [15] showed that with decreasing strain rate at one draw temperature the rate of increase in crystallinity with draw ratio decreased whereas the onset of crystallization shifts to higher draw ratios. More importantly, as is evident in *Figure 11*, the change in

slope from regime I to regime II occurs at higher level of crystallinity and is more pronounced with increasing temperature. This observation again reinforces the complexity of the interplay of temperature and strain rate that influences the mechanical behavior of PET during deformation. In this paper Salem also deduced from the draw time versus crystallinity curves that strain rate actually shifts the curves along the log-time axis and calculated a shift factor-strain rate relationship.

Swallowe et al. [1] performed experiments on amorphous PET at strain rates in the range 10^{-3} to 10^4 s^{-1} and temperatures from -10°C to 180°C . They found that the degree of crystallinity increased with strain rates from 10^{-3} to 10^3 s^{-1} . At 10^{-3} s^{-1} SIC occurred during the test. At strain rates greater than 10^3 s^{-1} , SIC did not occur in the short time scale (milliseconds) of the test. They also suggested, like others, that crystallization occurs only after imposing a certain critical level of stress on polymer chains. Spruiell et al. found that crystallinity of PET increased with strain rate in the range 10^{-4} to 10^{-1} s^{-1} . They concluded that a large amount of strain-induced crystallization (SIC) occurs when the necking deformation takes place. However, necking happens at a given temperature only if the strain rate is high enough to induce a critical stress level within the molecules.

G'sell et al. [74] studied the stretching of amorphous PET at just above the glass transition (90°C) and found that there occurs a significant strain hardening which increased with strain. The kinetics of SIC was found to become faster with increasing strain rate. Similarly Ajji et al. [75, 76] performed tensile drawing of amorphous PET films and sheets and showed that the onset of SIC depends upon the rate of tensile

stretching. They concluded that the strain rate, along with temperature, is the most critical parameter in the drawing of PET.

Ladouce et al. [77] deformed the amorphous and crystalline PET samples over five decades of strain rates and found a considerable influence of strain rate and microstructure on the stress-strain curves of PET. The high strain-rate deformation involved large inelastic deformation of the structure.

It is also worth noting that temperature rise due to work of plastic deformation during the adiabatic drawing process promotes thermal crystallization. The amount of temperature rise, given by the equation:

$$\Delta T = \frac{\int \sigma d\varepsilon}{\rho C_p}$$

depends upon factors such as draw speed.

Any significant temperature rise occurs only at very high strain rates such that heat dissipation can not take place during the short time-scale of the test.

Jabarin and Chandran [78-80] investigated the crystallization behavior of amorphous PET films during biaxial stretching at temperatures above the glass transition (80-105°C) and strain rates in the range of 5% to 200% s⁻¹. The occurrence of strain-induced crystallization was demonstrated under these conditions. It was found to happen at a level of strain that is independent of temperature and strain rate, defined as the strain hardening parameter. They also observed flow drawing at slow stretching rates owing to dominant

relaxation phenomena and low strain hardening modulus. The evolution of structure in PET from amorphous to semi-crystalline with finite deformation was demonstrated by following the crystallinity (based on density measurements) and orientation (from birefringence) development.

2.5.3 Role of amorphous phase orientation

Because the modulus of a 100% crystalline PET material is approximately an order of magnitude greater than that of any PET filament synthesized, the amorphous orientation is believed to play important role in determining the strength and stiffness of this semicrystalline polymer [28]. The amorphous phase orientation f_{am} is also a significant factor in crystallization as discussed by Swallowe et al.[1]. As stretching progresses, f_{am} increases by chain slippage and conformational changes (e.g. C-H bending). With increasing f_{am} , configurational and conformational entropy decrease, favoring crystallization. They suggested that crystalline structure grows by placement of chains into favorable position onto existing nuclei (frozen during quenching or formed by thermal fluctuations).

LeBourvellec et al. [8] proposed a critical level of amorphous orientation $\langle P_2(\cos\theta) \rangle_{cr}$ at which SIC starts to happen. They found that $\langle P_2(\cos\theta) \rangle_{cr}$ decreased with draw temperature. Also crystallinity increased with $\langle P_2(\cos\theta) \rangle$ at one draw temperature and vice-versa. At one strain rate and draw ratio, crystallinity decreased with draw temperature. Interestingly they concluded that critical orientation is associated with a critical draw ratio and is independent of strain rate at a given draw temperature.

The role of chain entanglements in the amorphous phase was proposed and the influence of entanglement density on the draw ratio for polyethylene considered in earlier studies [81]. The structure of the amorphous phase of oriented polymers was discussed by Murthy et al. and Keum et al. [82-84]. It was suggested that the average interchain distance in the amorphous phase could have two different values corresponding to the chains in the tilted planes within the layers of the transient structure.

Murthy et al. showed that the order of the amorphous phase can be expressed by the oriented and unoriented components. Murthy also proposed that since the local orientational order does not significantly affect the size (R_g) of the polymer chains, the spatial configurations of the chains in amorphous domains in semicrystalline polymers could differ from those of the unperturbed chains in the melt state, even if their R_g 's are the same.

Structural relaxation in drawn PET samples was studied by Matthews et al. [30] using IR spectroscopy, DSC and online spectrographic techniques. Crystallinity of samples drawn at 80°C was found to increase dramatically after reaching a draw ratio of 2.3 (see *Figure 12*) at a strain rate of 0.007 s⁻¹. The crystallization behavior of samples drawn at 80°C and several strain rates was studied with DSC thermograms (see *Figures 13 and 14*). The DSC scans showed an exotherm at 90–120°C related to the crystallization of oriented amorphous material. With increasing draw ratio the peak became less prominent, because more crystallization of the oriented material occurs during drawing.

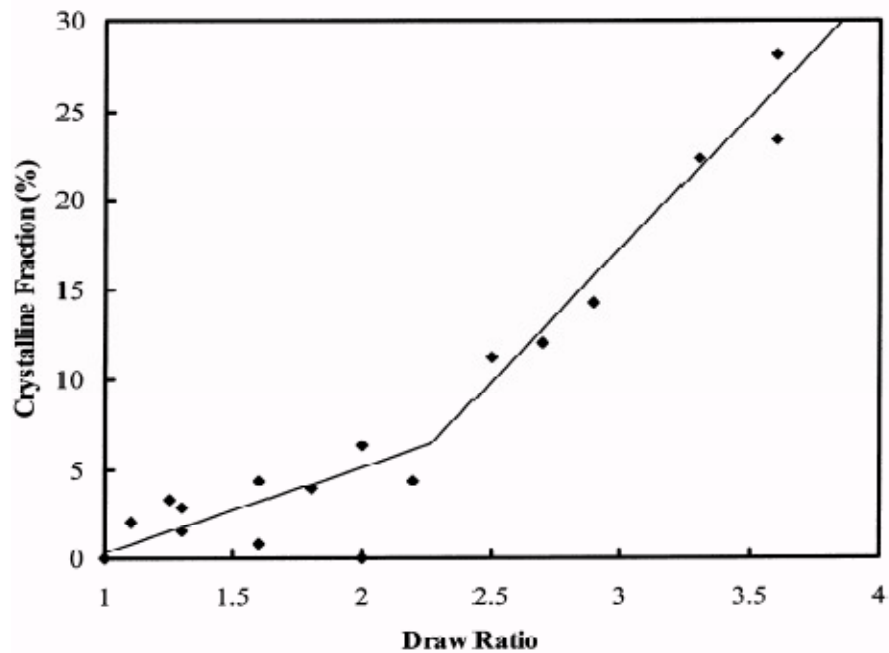


Figure 12. Increase in fractional crystallinity with draw ratio for PET drawn at 80°C and 0.007 s^{-1} (From Ref. 30)

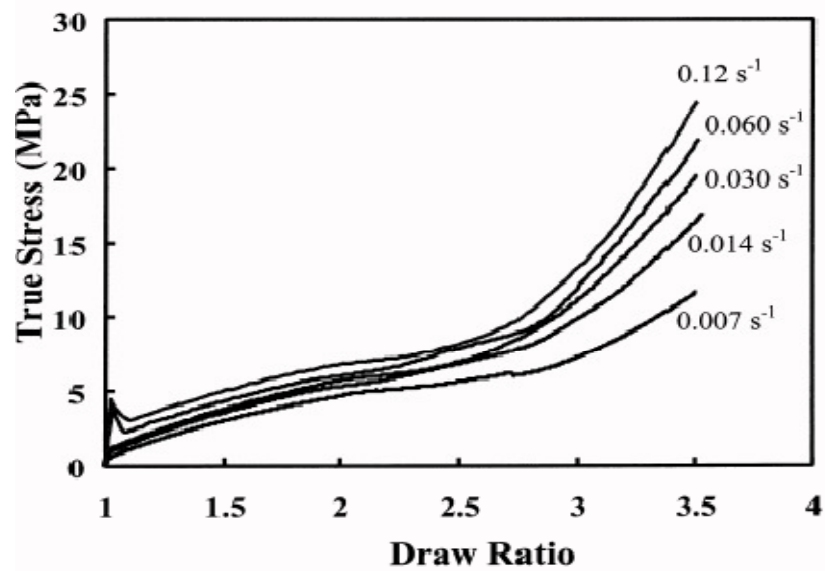


Figure 13. True stress–strain curves from drawing amorphous PET at 80°C at different initial strain rates (From Ref. 30)

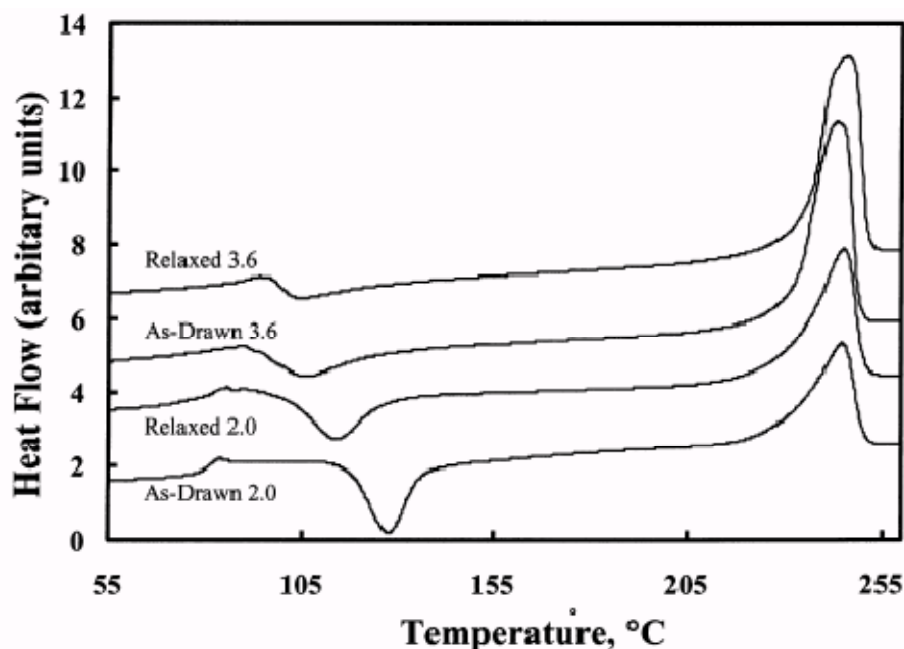


Figure 14. DSC scans for as-drawn and relaxed PET samples drawn at 80°C and 0.007 s^{-1} to draw ratio of 2.0 and 3.6 (From Ref. 30)

The crystallization temperature was lower as well as exhibited a smaller magnitude of crystallization exotherm for relaxed samples (kept at the drawing temperature for 30 min. after drawing, before cooling below T_g). This was attributed to conversion of the oriented amorphous material into crystalline material during the relaxation process. Birefringence was shown to decrease and then level-off for high draw ratios as compared to a continuous decrease at low draw ratios. This was attributed to a higher crystallinity owing to strain-induced crystallization present at draw ratios larger than 2.3. The crystallite formation accompanying this strain-induced crystallization causes an arrest of the molecular relaxation.

In related work, Alves et al. [85] recently determined the relaxation times of the cooperative conformational rearrangements of the amorphous phase of semi-crystalline

PET. When the crystalline phase is induced by annealing and is small in amount, they distinguish two different fractions in the amorphous phase with two different conformational mobilities. One of the phases that showed similar glass transition range as the amorphous material was ascribed to ‘conformational rearranging regions in the amorphous phase far from the crystallites’. The other phase, with higher glass transition temperatures, was attributed to the chains lying ‘close to crystalline lamellae’.

In an experimental study of the strain-induced crystallization of initially amorphous poly (ethylene terephthalate), Zaroulis et al. [86] performed uniaxial compression tests in both glassy (25-60°C) and glass transition (T_g) regime (60-76°C) at strain rates ranging from 0.005 to 0.5 s⁻¹. They reported a decrease in the yield stress and flow stress and a small decrease in the strain hardening modulus, with an increase in temperature and a decrease in strain rate. On the basis of DSC curves that yielded essentially temperature invariant cold crystallization exotherm area, it was concluded that network orientation without strain-induced crystallization occurs for deformation up to true strain of the order of -1.5. They also reported that the extreme sensitivity of the strain hardening behavior to strain rate in the transition region may cause an erroneous measurement of strain-induced crystallization behavior.

2.6 Studies of the crystallization behavior of PET

A large number of studies have been done on the experimental determination of the crystallization and yielding behavior of PET at temperatures below, close to or above its

glass transition. There is only limited experimental data concerning the deformed crystallization of PET.

One of the first comprehensive studies of the crystallization kinetics of PET was reported by Cobbs and Burton [4]. They followed the crystallization of amorphous PET films over the range 120- 240°C by observing changes in the infrared spectra at 972 cm^{-1} . The changes in absorption were correlated with density changes to obtain a measure of crystallinity. Half-times for crystallization were found to decrease to a minimum as the processing temperature was increased from 120 to about 210°C and then decreased again over the range of 220-240°C. The shortest half-time was reported at about 190°C. An activation energy of 20 kcal./mole, based on induction times, was reported. The kinetic data were fitted to a modified Avrami equation and the Avrami exponent k was determined at various temperatures. The value of k was interpreted as an indication of shape of growing crystallites. The growth mechanism for PET was reported as plate-like from 120°C to 180°C.

Chaari et al. used a high intensity synchrotron x-ray source for studying the evolution of crystallinity in PET with tensile strain [87]. The drawing of PET samples was carried out at 95°C and x-ray diffraction pictures were recorded at different draw ratios as the deformation progressed. For example *Figures 15* and *16* show the stress as a function of draw ratio along with x-ray photos at different points on the curve for two strain rates:

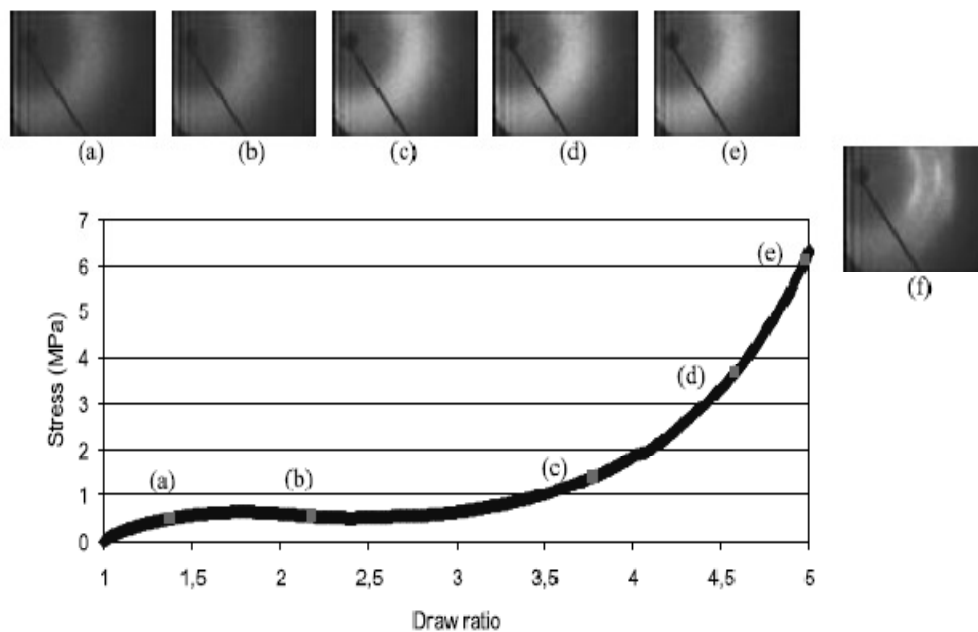


Figure 15. Tensile stress as a function of draw ratio at 0.06 s^{-1} and 95°C (From Ref. 87)

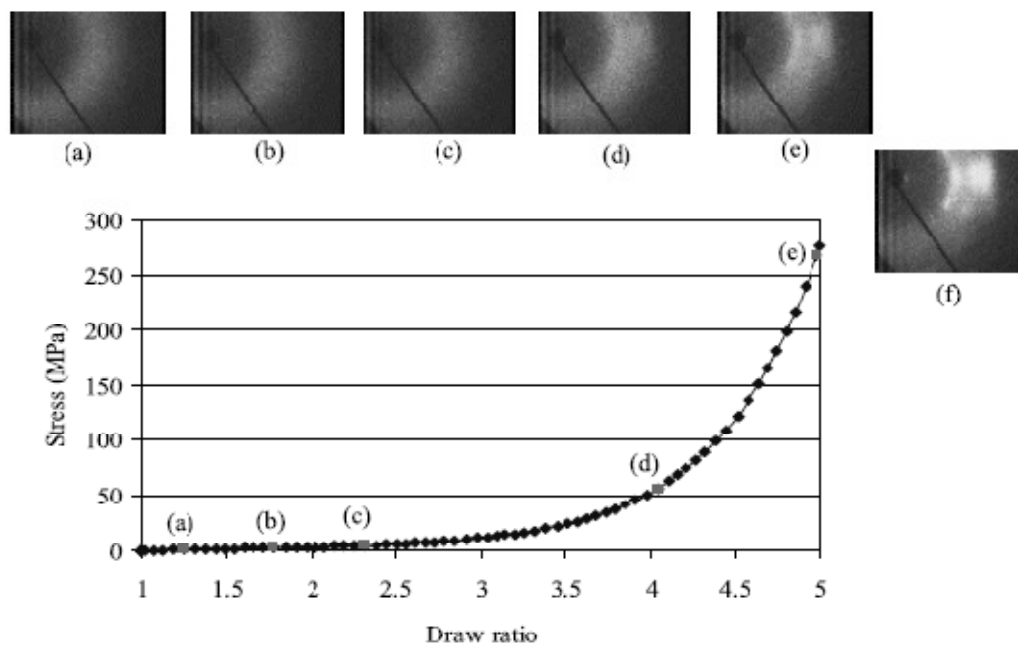


Figure 16. Tensile stress as a function of draw ratio at 0.75 s^{-1} and 95°C (From Ref. 87)

From these measurements they proposed the presence of three different regimes in crystallization. At very small extension rate of 0.06 s^{-1} , crystallinity development is negligible during the deformation. For intermediate strain rates, crystallization occurs during the deformation process itself. At 0.75 s^{-1} , however, the crystallization process started during the deformation and ‘continued under isothermal and constant strain conditions’ after drawing was stopped. In another paper Chaari and Chaouche investigated the crystallization behavior of PET at different temperatures and strain rates [88]. The optical dichroism measurements revealed a qualitatively different evolution behavior from that of the birefringence development as shown in *Figure 17*. Based on those results they proposed that there are three stages of crystallization. The first stage consists of increasing birefringence and stress essentially caused by increased molecular orientation. The dichroism and crystallinity ratio show a significant rise in the second stage. This was attributed to the nucleation phase, in which ‘anisotropic nuclei spread over the medium’, during the second stage. The final stage entails those nuclei acting as elastomeric crosslinks, which causes a rapid rise in the growth rate of the crystallites. But the crystallite growth was assumed to be less anisotropic since dichroism was found to decrease during this last stage.

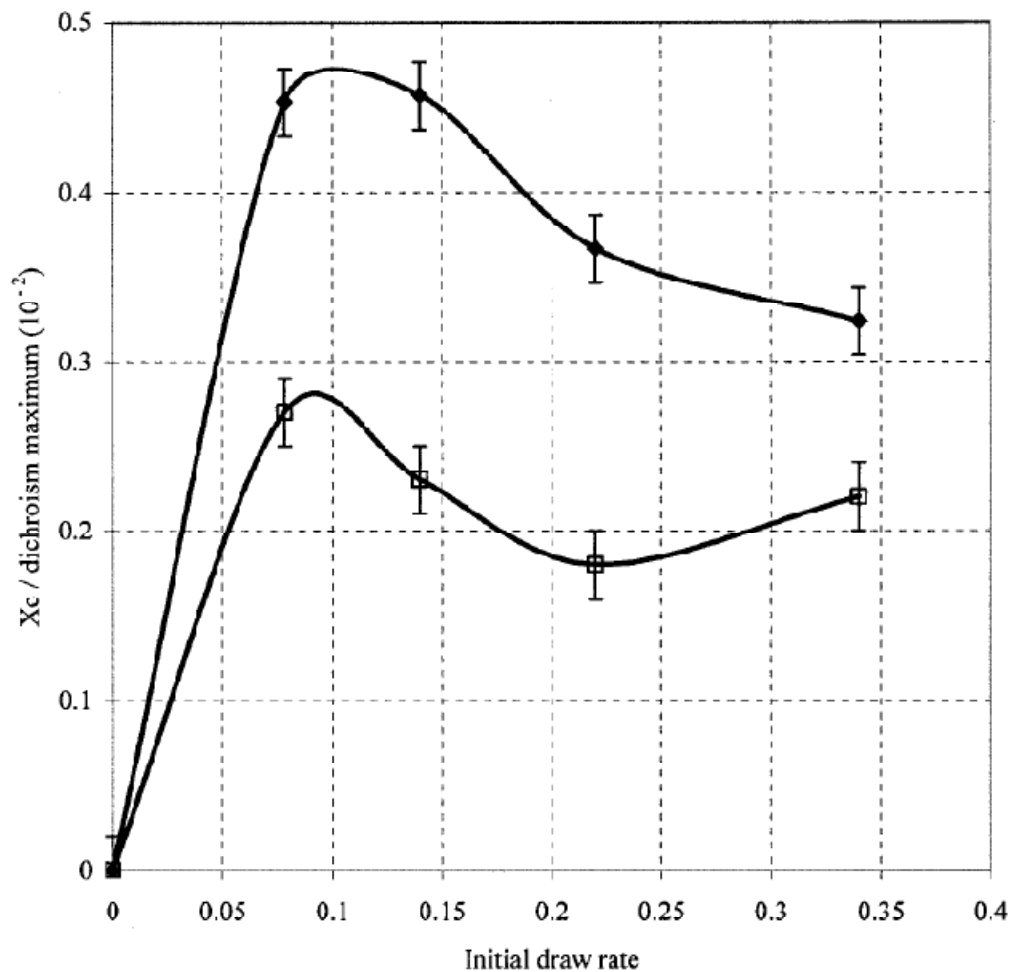


Figure 17. Comparison of the evolution of the maximum dichroism (blank squares) versus the initial strain rate at 90°C and the evolution of the final value of the crystallinity (filled blocks) ratio (From Ref. 88)

Myung et al. [89] studied the SIC behavior of PET at different temperatures and shear rates using rheometry combined with x-ray diffraction studies. The dynamic mechanical behavior as well as the morphology of PET was experimentally determined. *Figures 18* and *19* show the effect of shear rate on G' (storage modulus) and η' (dynamic viscosity) at 220°C. It is clear from *Figure 18* that G' reaches the same plateau value at all frequencies and temperatures; whereas the plateau value of η' is decreased with

increasing frequency, as evident from *Figure 19*. The reduction in viscosity was associated with ‘destruction of the ordered crystallite particle structure’.

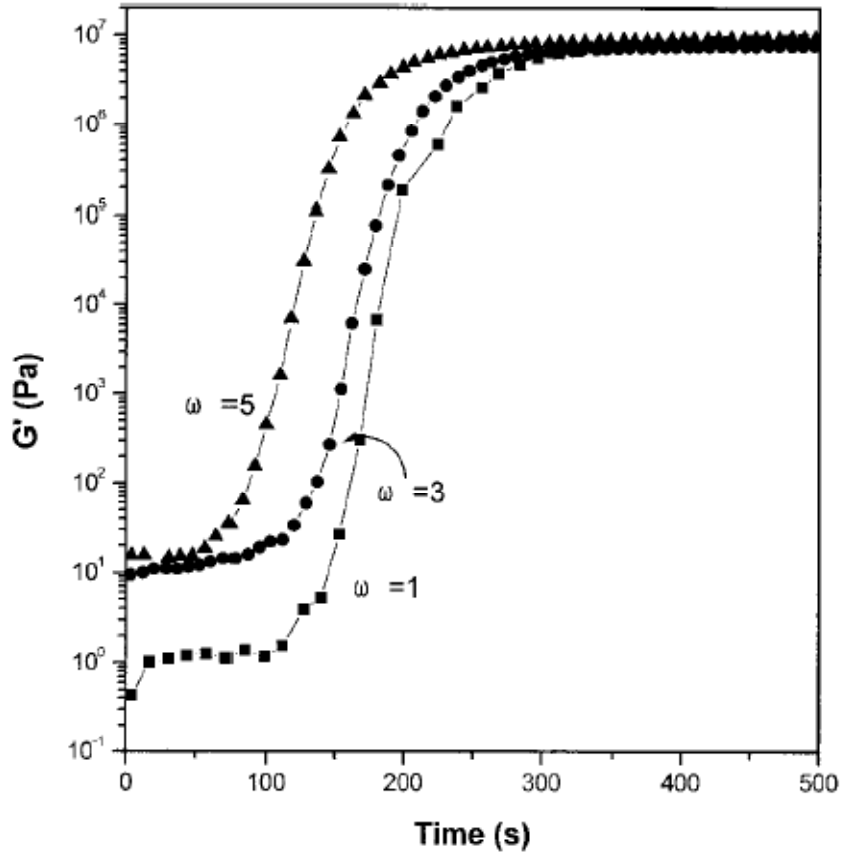


Figure 18. Change in storage modulus (G') versus time at 220°C for PET at frequencies of 1, 3 and 5 rad/s (From Ref. 89)

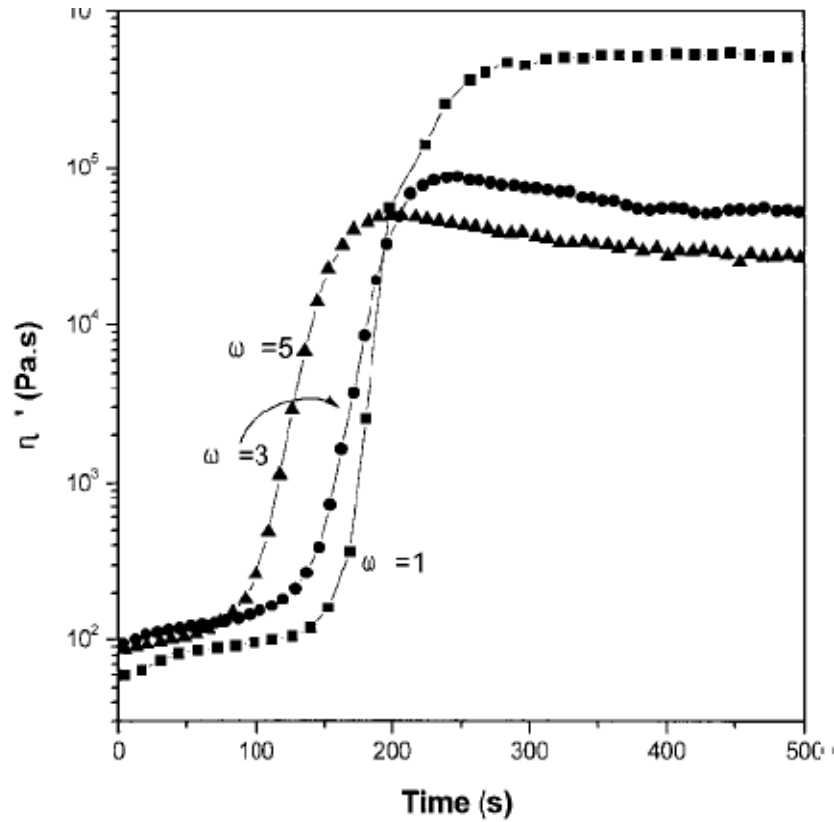


Figure 19. Change in dynamic viscosity (η') versus time at 220°C for PET at frequencies of 1, 3 and 5 rad/s (From Ref. 89)

Their optical measurements indicated that a larger number of smaller spherulites formed at higher frequencies. This means that nucleation rate and therefore the crystallization rate increases with increasing frequency. This result also explains the decreased induction time of crystallization with frequency. Their x-ray data showed that crystallite size and ‘perfectness’ decreased with frequency for PET crystallized isothermally at 240°C. The dimensions of the unit cell lattice of PET also increased with increasing frequency.

Chan and Isayev [90] measured the isothermal and non-isothermal crystallization isotherms for PET for both the cold-crystallization (heating from below T_g) and melt-crystallization (cooling from melt). For PET they found that the rate of isothermal

crystallization is much higher at temperatures between 125 and 210°C than below 112°C or above 224°C. The rate of non-isothermal crystallization was found to depend upon the heating or cooling rate. During cold crystallization, a higher heating rate results in slower apparent rate of crystallization; similarly during melt crystallization, a higher cooling rate would lead to a slower apparent crystallization rate. They stressed the importance of induction time, temperature lag as well as time lag (time taken by system to reach isothermal condition) in measuring isothermal crystallization data using DSC. They argued that measurement of precise crystallization rate would be difficult using DSC. But if all those factors are taken care of the extrapolated isothermal crystallization data from DSC can be safely applied to describe non-isothermal kinetics.

Radhakrishnan and Kaito [91] reported the analysis of crystallization behavior of oriented films of PET using in-situ FTIR, WAXD, and SAXS studies. Evolution of dichroic ratio was followed using polarized in situ FTIR and correlated with changes in orientation with time. WAXD measurements were used to study the development of fine crystal structure. As an example, *Figure 20* shows that the absorption intensity of the 971 cm⁻¹ band decreases and that of the 1370 cm⁻¹ band increases, when heated from room temperature to the crystallization temperature. Based on their studies they proposed a structural evolution consisting of three regimes. The first regime involves molecular relaxation, immediately above the T_g. The second regime involves rearrangements in the oriented amorphous structure, leading to large increase in orientation with time and the *gauche* conformation is transformed into the *trans* conformation. The third stage is the stacking

of oriented molecular chains into the crystal lattice to form crystallites. The degree of orientation and the *trans* content were found to be constant in this stage.

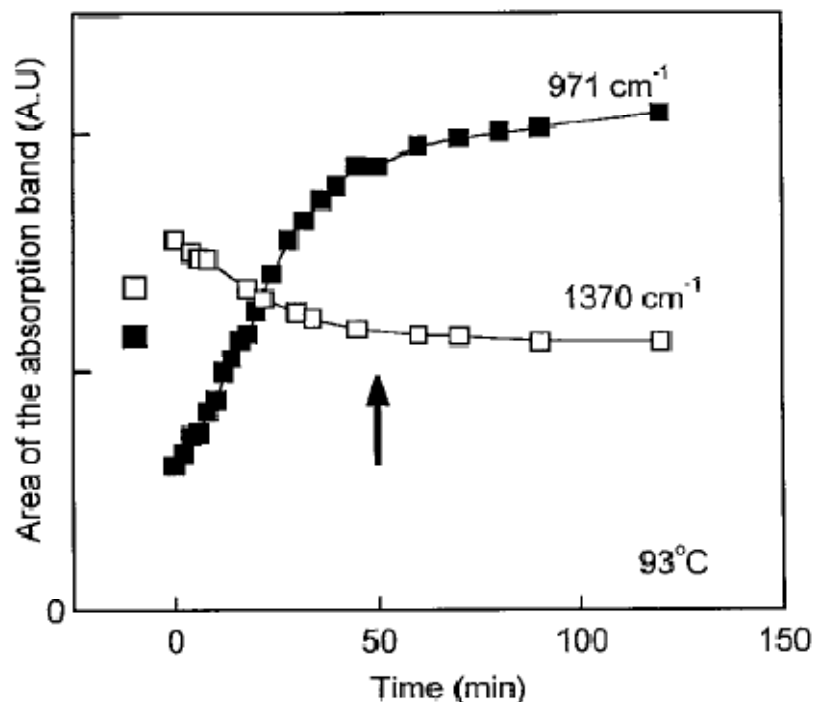


Figure 20. Areas of the 971 cm^{-1} (*trans*) and 1370 cm^{-1} (*gauche*) bands as a function of time during isothermal crystallization at 93°C (From Ref. 91)

Ordering of the polymer chains during the induction period was suggested based upon those results.

Mayhan et al. [92] followed the isothermal crystallization of amorphous films of poly(ethylene terephthalate) in the range $25\text{--}240^{\circ}\text{C}$ by recording the change in amount of light ($\lambda=400\text{ nm}$) transmitted with time. Crystallization half-times decreased and rate constants were found to increase exponentially over the range $96.5\text{--}119.5^{\circ}\text{C}$. The half-life values obtained by them were in good agreement with those reported by Cobbs and Burton, as shown in *Figure 21*.

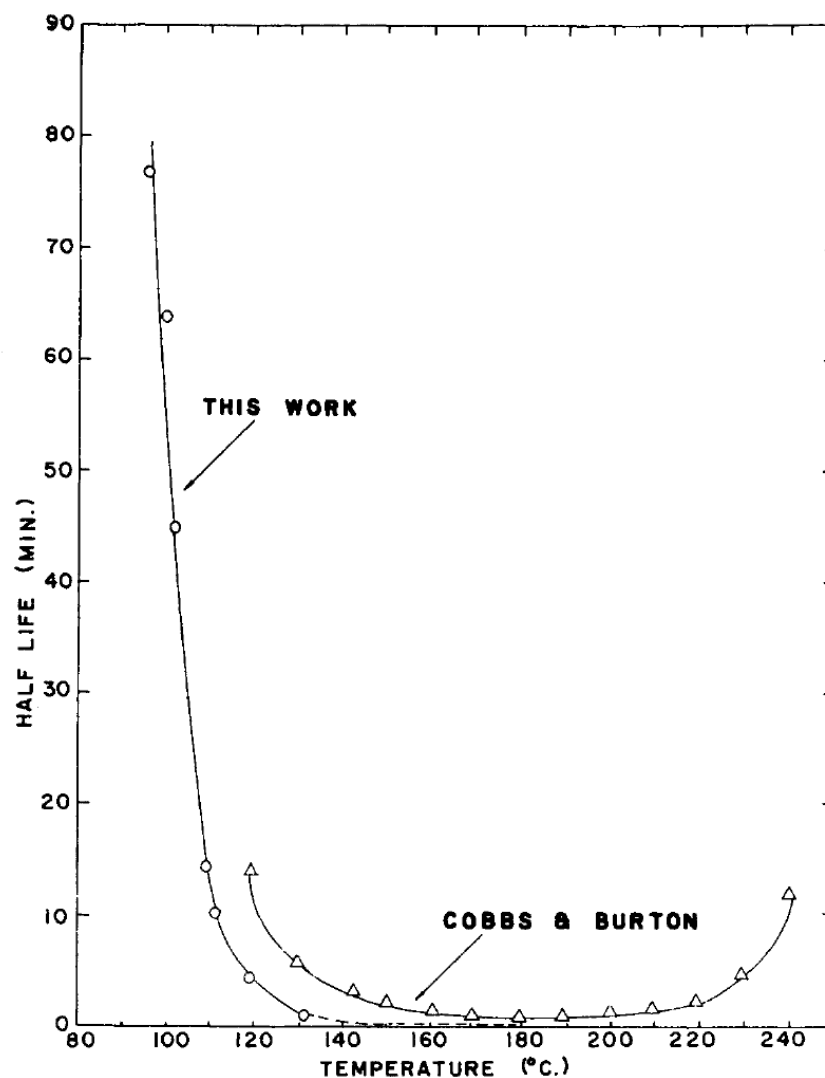


Figure 21. Comparison of crystallization half-time values obtained in two works (From Ref. 92)

The apparent activation energy for the primary crystallization process determined from their work (37 kcal./mole of segment crystallized) was considerably higher than the 20 kcal./mole reported by Cobbs and Burton. Similarly their conclusion based on the Avrami constants was that a preferred linear growth occurs; whereas Cobbs and Burton suggested a favored platelike growth in poly (ethylene terephthalate). These differences were

assumed to be caused by the use of induction times by Cobbs and Burton and a slightly different temperature span covered in the two works.

Jabarin studied the isothermal [93] as well as non-isothermal [94] crystallization behavior of PET during cooling from the melt, as a function of molecular weight and catalyst system. It was shown that crystallization rates as well as mechanism of crystallization are dependent on molecular weights, temperature, and the catalyst system used during polymerization of PET. The isothermal crystallization kinetics was analyzed on the basis of Avrami expression and various kinetic constants were determined. A lot of qualitative information can be obtained from Avrami exponent, n , about the nature of nucleation and the growth processes (see *Table 1*).

Table 1. Various types of nucleation and growth processes and its relation with Avrami exponent (From Ref. 93)

n	Crystallization mechanism
4	Spherulitic growth from sporadic nuclei
3	Spherulitic growth from instantaneous nuclei
3	Disc-like growth from sporadic nuclei
2	Disc-like growth from instantaneous nuclei
2	Rod-like growth from sporadic nuclei
1	Rod-like growth from instantaneous nuclei

It was also suggested that the rate constant, k , depends not only upon $t_{1/2}$ but also is function of the Avrami exponent n . Thus crystallization rate cannot be directly measured from the values of only $t_{1/2}$, particularly when n is also changing. In their dynamic crystallization study (non-isothermal crystallization at a constant cooling rate) it was

found that the non-isothermal crystallization kinetics is similar to the isothermal case. Also it was shown that the minimum cooling rate required to produce amorphous PET is dependent on both the molecular weight and the polymerization catalyst system.

Similar studies were performed by Ozawa by observing DSC curves of crystallization of PET during cooling at constant rates [95]. His analysis revealed the possible presence of a “primary (Avrami)” crystallization followed by a slower secondary crystallization (“post-Avrami”) process. Avrami equation was applied in an extended or modified form to describe the non-isothermal crystallization kinetics.

Effect of molecular orientation on the crystallization rate in PET was investigated by Alfonso et al. [96] in the temperature range 95-115°C. Samples with different amorphous phase orientation (f_a) were obtained by spinning at speeds from 1250-3000 m/min. The isothermal crystallization rate was empirically expressed as:

$$\left(\frac{1}{t_{1/2}}\right) = \left(\frac{1}{t_{1/2}^*}\right) \exp\left(\frac{-4\ln(2) \cdot (T-T^*)^2}{D^2}\right) \exp(Af_a^2) \quad (3)$$

where $t_{1/2}$ is the half-time of crystallization, $t_{1/2}^*$ is the minimum half-time corresponding to maximum crystallization rate at the temperature T^* , and D is the half-width of the Gaussian curve. The parameter A consists of the sensitivity of crystallization rate towards amorphous orientation factor f_a . The values for PET were reported as: $t_{1/2}^* = 42$ sec; $T^* = 190^\circ\text{C}$ and $D = 64^\circ\text{C}$. The dependence of constant A on temperature was empirically expressed and its value increased with temperature. As shown in *Figure 22*, the crystallization rate increased (or crystallization half-time decreased) with increasing molecular orientation.

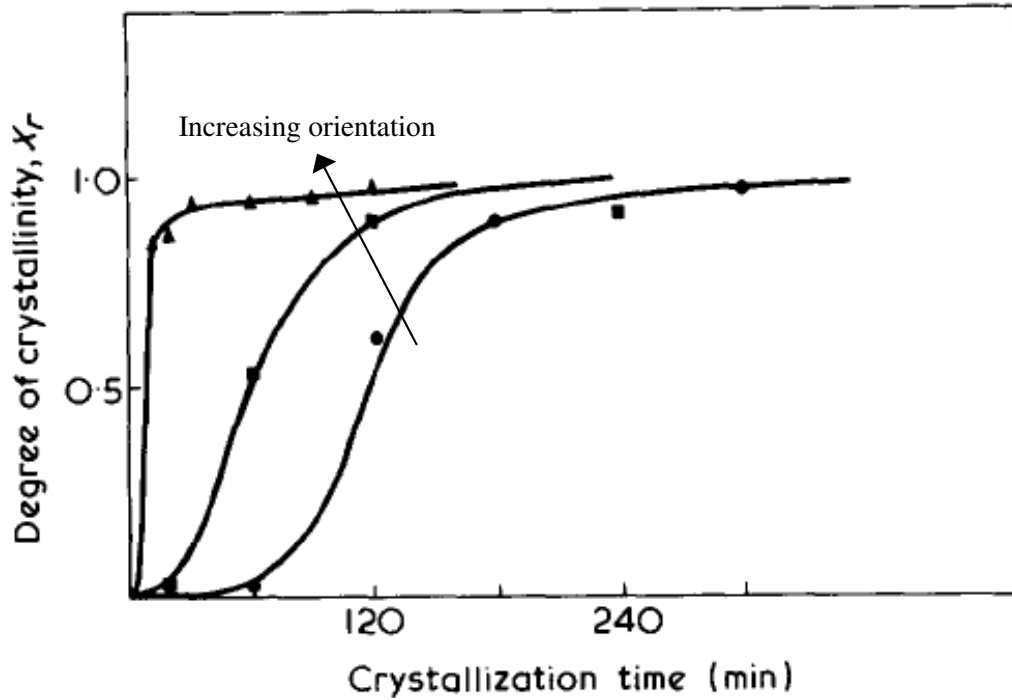


Figure 22. Fractional crystallinity as a function of time at $T_c = 100^\circ\text{C}$ for PET with f_a (from left to right) = 0.123, 0.044, 0.023 (From Ref. 96)

2.7 Rate of crystallization

The effects of crystallization rate (in the presence as well as absence of stress) and the transport of heat generated during crystallization must be considered to understand SIC phenomena.

2.7.1 Homogeneous nucleation of unoriented melts

For a surface nucleated process in absence of stress, stability and growth of an embryonic nucleus is determined by the balance of surface energy required to form the nucleus and the free energy change per unit volume for the liquid to solid transformation. It is based upon the change in Gibb's free energy by creation of new crystal surfaces during the nucleation step of crystallization at a given temperature T : $\Delta f = \Delta h - T\Delta s$

with Δh and Δs being the enthalpy change and the entropy change respectively. Assuming that the spherical nuclei are being formed, it is natural to assume that Δf will decrease if more molecules ‘join’ the nuclei. But Δf is increased due to additional surface energy as nuclei are formed. The net change in free energy depends upon the crystal size. When the nuclei size is small, the surface area per unit volume is high and f increases with increasing nuclei radius because of dominant surface energy effect. But the surface area per unit volume decreases as the radius becomes larger. Thus there is a critical nuclei radius above which the net change in f is negative. This critical nuclei size represents the energy barrier that must be overcome to form stable nuclei. At this condition a dynamic equilibrium exists between the melt and the crystals.

The homogeneous nucleation rate is obtained by Turnbull and Fisher equation [97]:

$$I = K \left(\frac{NkT}{h} \right) \exp \left[\frac{\Delta S^*}{k} \right] \exp \left[\frac{-\Delta H^*}{kT} \right] \exp \left[\frac{-\Delta \phi^*}{kT} \right] \quad (4)$$

where k is Boltzmann’s constant, h is Planck’s constant, ΔS^* is entropy of formation of crystallite, ΔH^* is enthalpy of formation of crystallite, K is a constant, T is the crystallization temperature and $\Delta \phi^*$ is the free energy of formation of a nucleus of critical size. For a spherical nucleus of radius r and surface free energy σ_s , the total free energy of nucleus is the difference between surface and volume free energy changes required to form the sphere:

$$\Delta \phi = 4\pi r^2 \sigma_s - \frac{4}{3} \pi r^3 (\Delta G) \quad (5)$$

where ΔG is the bulk free energy of fusion per unit volume.

A critical radius r^* , at which the free energy $\Delta\phi$ goes through a maxima ($\Delta\phi^*$), can be found by differentiating $\Delta\phi$ with respect to r and equating to zero.

$$\frac{d(\Delta\phi)}{dr} = 8\pi r\sigma_s - 4\pi r^2(\Delta G) = 0 \quad (6)$$

at $r = r^*$ which can be solved to give

$$r^* = \frac{2\sigma_s}{\Delta G} \quad (7)$$

The maximum of $\Delta\phi$ is confirmed by seeing that its double-derivative is negative at r^* .

Substitution into equation (5) gives

$$\Delta\phi^* = \frac{16}{3}\pi \frac{\sigma_s^3}{(\Delta G)^2} \quad (8)$$

It can be clearly seen that total free energy of an embryonic nucleus increases with increasing r until it crosses the size r^* after which it starts to decrease. Note that $\Delta\phi$ is positive for radius smaller than r^* . Such a nucleus is unstable and will not grow to a crystallite. On the other hand, a nucleus greater than the critical size has a negative total free energy and is therefore thermodynamically stable and grows with time.

Substitution into Equation (5) gives

$$I = I_0 \exp\left[\frac{-\Delta H^*}{kT}\right] \exp\left[-\frac{16}{3}\pi \frac{\sigma_s^3}{(\Delta G)^2 kT}\right] \quad (9)$$

where I_0 is a constant containing all temperature independent terms. The above expression for spherulitic growth can be generalized for a rectangular parallelepiped of length l and transverse dimensions a and b :

$$I = I_0 \exp\left[\frac{-\Delta H^*}{kT}\right] \exp\left[-\frac{32\pi\sigma_s^2\sigma_e}{(\Delta G)^2 kT}\right] \quad (10)$$

where σ_s is the lateral surface free energy and σ_e is the end surface free energy [65].

In absence of external stress fields, the bulk free energy ΔG depends only upon the supercooling $\Delta T = T_m^0 - T$, where T_m^0 is the equilibrium melting temperature of the polymer crystal:

$$\Delta G = \frac{\Delta h_f \cdot \Delta T}{T_m^0} \quad (11)$$

where Δh_f is the latent heat of fusion per unit volume.

Thus the final expression for homogenous nucleation rate of an unoriented polymer melt is arrived at as follows:

$$I = I_0 \exp \left[\frac{-\Delta H^*}{kT} \right] \exp \left[- \frac{32\pi\sigma_s^2 \sigma_e (T_m^0)^2}{(\Delta h_f)^2 (\Delta T)^2 kT} \right] \quad (12)$$

The nucleation rate, not surprisingly, is inversely dependent on degree of supercooling; because with increasing supercooling the critical nucleus size decreases leading to the formation of a large number of relatively small nuclei all growing with time into crystallites. Also due to the squared supercooling term, the crystallization rate is strongly dependent upon temperature. It has been observed that crystallization rate actually goes through a maximum with increasing supercooling and becoming zero near the glass transition temperature. The activation energy of transporting the material across the liquid-solid interface hinders nucleation and decreases the rate of crystallization [65]. This effect is significant at large supercooling. Reduced mobility of chains with decreasing temperature leads to a decrease in rate of crystallization. Limited segmental motion near glass transition explains why the rate of crystallization approaches zero near the glass transition.

2.7.2 Kinetics of quiescent crystallization

For a nucleation-dominated crystallization process such as in a polymer, the most widely used model for kinetics of crystallization is the differential form of modified Avrami equation known as Nakamura model [98]:

$$\dot{y} = \frac{dy}{dt} = mK(T)[- \ln(1 - y)]^{\frac{m-1}{m}} (1 - y) \quad (13)$$

Here m is the Avrami exponent, y is the fractional crystallinity, T is the draw temperature and K is the non-isothermal rate constant. The temperature dependence of the rate constant in the Nakamura model is captured by the Hoffman-Lauritzen expression:

$$K(T) = [\ln 2]^{\frac{1}{m}} \left(\frac{1}{t_{1/2}} \right)_0 \exp \left(\frac{-U^*/R}{T - T_\infty} \right) \exp \left(\frac{K_k}{T \cdot f \cdot \Delta T} \right) \quad (14)$$

Here K_k is the nucleation exponent, U^* is the activation energy for the segmental jump and equal to 6284 J mol^{-1} [44, 45], R is the universal gas constant, $(1/t_{1/2})_0$ is the pre-exponential term taking care of all different crystallization process variables except the temperature and f is the correction factor:

$$f = \frac{2T}{T_m^0 + T} \quad (15)$$

Here the presence of f accounts for the decrease in latent heat of fusion with decreasing temperature, with

$$T_\infty = T_g - 30 \text{ and } \Delta T = T_m^0 - T \quad (16)$$

where ΔT is called the “supercooling” and T_m^0 the equilibrium melting temperature of the unoriented polymer.

2.7.3 Nucleation rate under applied stress

Under the application of tensile stress to the melt, the resulting entropy reduction also means that the free energy change required for liquid to solid transformation is larger. Therefore the nuclei of smaller size are stable enough to grow at a given degree of supercooling as compared to the same nuclei which are unstable in an unoriented melt. As a result the nucleation rate is increased. In other words, the ordering of chains in the melt causes them to fall in a parallel arrangement or aligned state eventually found in a crystal and thus promotes crystallization. For oriented melts the higher nucleation rate can be expressed through a modification of the bulk free energy ΔG :

$$\Delta G = \frac{\Delta h_f \cdot \Delta T}{T_m^0} + \Delta f_E \quad (17)$$

where $\Delta f_E = \beta F$ is the contribution of stored elastic free energy to the thermal energy [65].

Here F is the applied tension or spinline stress and β is a constant of the order of unity.

Yeh et al. proposed a theory for strain-induced crystallization and its effect on crystallization kinetics and crystal size of polyethylene at 130°C [99]. Their model is based on the effects of macroscopic molecular strain on the crystallization behavior, without any assumptions about chain conformations or crystal morphology (extended chain nuclei, fringed-micelle or folded-chain crystals). According to them the defects present in the amorphous state of the melt in the form of folds are responsible for the observed hindered growth of crystallite thickness in the c -axis direction in SIC. They assumed that originating primitive structure is similar for both QC and SIC since chain-folds are already present in both instances. Therefore a nucleation rate theory was developed by taking equal values of σ_s and σ_e for both cases.

According to Yeh et al. the fundamental driving force for nucleation of polymers is the difference in free energies between melt and crystal [99]. For QC, $\Delta f = \Delta H - T\Delta S$ is the free energy difference between melt and crystal, whereas for SIC $\Delta f^0 = \Delta H^0 - T\Delta S^0$ is the free energy difference between oriented melt and crystal; with ΔH and ΔS , and ΔH^0 and ΔS^0 being the corresponding changes in enthalpy and the entropy respectively. Thus the driving force for SIC is greater than that for QC by an amount

$$\Delta f^0 - \Delta f = (\Delta H^0 - \Delta H) - T(\Delta S^0 - \Delta S) = T \cdot \Delta S'$$

assuming that $\Delta H^0 - \Delta H$ is negligible. Since $\Delta S' = \Delta S - \Delta S^0$ is positive, the free energy change is higher and favors crystallite formation for SIC.

Finally, assuming a limited diffusion transport at high temperatures, Yeh et al. gave the expression for enhanced nucleation rates for SIC (N^0) compared to QC (N):

$$\frac{N^0}{N} = \exp \left[\frac{A\sigma_s^2\sigma_e}{kT} \right] \cdot \left[\frac{1}{(\Delta f)^2} - \frac{1}{(\Delta f + T\Delta S')^2} \right] \quad (18)$$

where A is a geometric constant. The degree of entropy reduction $\Delta S'$ reflects the orientation enhancement that leads to nucleation rate increase:

$$\Delta S' = \frac{k\tilde{N}}{2} \cdot \left(\frac{24\mu}{\pi} \right)^{1/2} \cdot (\alpha - 1) \quad (19)$$

Thus entropy decrease is directly related to the macroscopic stretch ratio α (assuming affine deformation), μ is the number of statistical segments per network chain and \tilde{N} is the number of network chains per unit volume.

2.7.3.1 Failure of nucleation theory under large stress and supercooling

The homogeneous nucleation theory is a continuum model assuming that there are well-defined macroscopic phases with sharp boundaries between them. But for very large

values of ΔG , as happens under large spinline stresses or at large supercooling, the critical nucleus size becomes comparable to the dimensions of the unit cell of crystal lattice. Under these circumstances, the nucleation and growth theory involving sporadic transformation and growth is not applicable. Instead the mechanism for crystallization is a more continuous process occurring throughout the material, like spinodal decomposition, limited only by the diffusion [65]. This mechanism has a much faster rate than predicted by the equation (12) and leads to fine grained crystallization called ‘nucleative collapse’.

A crystallization process in the absence of any external stress fields is essentially comprised of two steps: nucleation (formation of ‘embryo’) and growth of nuclei. But the presence of flow fields or externally applied stresses such as shearing or uniaxial extension has been shown to lead to formation of “thread-like pre-cursors” prior to the nucleation [100]. Therefore the kinetics of crystallization is different when deformation forces are present.

2.7.4 Kinetics of strain-induced crystallization (SIC)

In SIC, the critical nucleus size and the free energy required to form a critical nucleus, both are reduced. The former thermodynamically favors nuclei formation (a larger population of finer crystallites) while the latter kinetically promotes the rate of nucleation. The application of external stresses helps alignment of the molecules along the direction of applied stress and packing them in to favorable position for nuclei formation. Thus the induction period is shortened, resulting in a different kinetics than

quiescent crystallization [100]. It is assumed that after the completion of nuclei formation, the growth of nuclei proceeds unaffected by the presence of stress.

The thermodynamic theory of crystallization, originally due to Flory [101], predicts that the reduction in entropy ΔS_{el} due to alignment of molecules caused by orientation of the network leads to an increase in the equilibrium melting temperature of an oriented network. For crystallization under stress (SIC) the equilibrium melting temperature, T_m , is given by:

$$T_m = \frac{\Delta H}{\Delta S} = \frac{\Delta H}{\Delta S^0 - \Delta S_{el}} \quad (20)$$

Thus the increased melting temperature of an oriented polymer is obtained as:

$$\frac{1}{T_m} = \frac{\Delta S^0}{\Delta H} - \frac{\Delta S_{el}}{\Delta H} = \frac{1}{T_m^0} - \frac{\Delta S_{el}}{\Delta H} \quad (21)$$

where ΔS_{el} is the additional entropy change of the network due to stress and ΔH is the change in enthalpy of crystallization.

The entropy change, as predicted by rubber-elasticity theory, was given by Krigbaum and Roe [50] as:

$$\Delta S_{el} = \frac{k\tilde{N}}{2} \cdot \left(\alpha^2 + \frac{2}{\alpha} - 3 \right) \quad (22)$$

Flory [48] also gave an expression for ΔS_{el} as below

$$\Delta S_{el} = \frac{k\tilde{N}}{2} \cdot \left[\left(\frac{24\mu}{\pi} \right)^{1/2} \cdot \alpha - \left(\alpha^2 + \frac{2}{\alpha} \right) \right] \quad (23)$$

Kim et al. [45] applied the same thermodynamic theory of entropy reduction in stressed systems to study the flow-induced crystallization during injection molding of crystallizable polymers. They determined the value of enthalpy change from the difference between heat released by crystallization per unit mass and the created interfacial energy per unit mass:

$$\Delta H_f = \Delta H_f^m - \Delta H_f^A = f_{cr} \cdot \Delta H_f^m \quad (24)$$

Here f_{cr} is the crystallization factor and depends upon interfacial energy created during crystallization. f_{cr} is defined as the ratio of crystallization enthalpy change and heat of crystallization and its value was 0.03 for PET [44]. The melting temperature elevation for an oriented polymer melt including the effect of heat released during crystallization was then obtained as:

$$\frac{1}{T_m} = \frac{1}{T_m^0} - \frac{\Delta S_{el}}{f_{cr} \cdot \Delta H} \quad (25)$$

Interestingly Kim et al. expressed the reduction in entropy as a function of the Finger strain tensor C :

$$\Delta S_{el} = \sum_k \frac{\mu_k}{T\rho} [I_C^k - 3] \quad (26)$$

where $I_C^k = C_{11,k} + C_{22,k} + C_{33,k} = \lambda_k^2 + \frac{2}{\lambda_k}$ is the first invariant of the k^{th} mode of C_k and

obtained from solving the governing equations for C_k . It represents change in volume per

unit volume for infinitesimal strains. Also μ_k is the modulus of the k^{th} mode: $\mu_k = \frac{\eta_k}{2\theta_k}$

where η_k is the shear viscosity and θ_k is the relaxation time of the k^{th} mode. Due to the

crystallization, the viscosity and relaxation time were assumed to be dependent upon fraction of crystallinity.

For an oriented polymer system during stretching at a temperature T above the glass transition, crystallization will occur as soon as T_m reaches the local temperature. Thus the elevation of melting temperature has the effect of supercooling and acts to increase the crystallization rate. This effect of enhanced rate of crystallization was then incorporated into the rate constant $K(T, \dot{\gamma})$ of the non-isothermal crystallization equation by use of the elevated melting temperature of the oriented melt (T_m) instead of the isotropic (T_m^0) melt as originally suggested by Ishizuka and Koyama.

Thus the rate of phase transformation is expressed again based upon the non-isothermal Nakamura equation and following the work of Kim and co-workers [44, 45]:

$$\dot{y} = \frac{dy}{dt} = mK(T, \dot{\gamma})[-\ln(1 - y)]^{\frac{m-1}{m}}(1 - y) \quad (27)$$

where $K(T, \dot{\gamma})$ is the modified non-isothermal crystallization rate constant:

$$K(T) = [\ln 2]^{\frac{1}{m}} \left(\frac{1}{t_{1/2}} \right)_0 \exp\left(\frac{-U^*/R}{T - T_\infty}\right) \exp\left(\frac{K_k}{T \cdot f \cdot \Delta T}\right) \quad (28)$$

$$\text{with} \quad f = \frac{2T}{T_m(T, \dot{\gamma}) + T} \quad (29)$$

$$\text{and} \quad T_\infty = T_g - 30 \text{ and } \Delta T = T_m(T, \dot{\gamma}) - T \quad (30)$$

Note that equations (29) and (30) are based upon the elevated melting temperature T_m of the polymer, unlike the equations (15) and (16) which utilize equilibrium melting temperature T_m^0 .

2.7.5 Governing transport equations

By considering the conservation of polymer mass, momentum conservation and energy balance in crystallization, the following equations can be obtained.

Equation of continuity (mass conservation):

$$\frac{D\rho}{Dt} = -\rho \frac{\partial u}{\partial x} \quad (31)$$

Equation of energy conservation:

$$\rho C_p \frac{DT}{Dt} = k \frac{\partial^2 T}{\partial z^2} + \dot{\phi} + \dot{H}_v \quad (32)$$

where ρ is the density, C_p is the specific heat capacity, k is the thermal conductivity, $\dot{\phi}$ is the viscous dissipation, \dot{H}_v is the rate of crystallization heat released per unit volume, and D/Dt is the material derivative.

The term \dot{H}_v in equation (32) accounts for the heat released during crystallization and given as:

$$\dot{H}_v = \rho \Delta H_f \frac{Dy}{Dt} = \rho X_\infty \Delta H_c \frac{Dy}{Dt} \quad (33)$$

where ΔH_f and ΔH_c are the heat of melting per unit mass for the current crystalline state and the perfect 100% crystalline state of the polymer, respectively. This term captures the effect of volume and surface crystallization kinetics upon the thermomechanical behavior of the sample.

The viscous dissipation can be obtained as:

$$\dot{\phi} = \eta \dot{\gamma}^2 \quad (34)$$

where $\dot{\gamma}$ is the strain rate applied.

2.8 Models to describe the mechanical behavior of PET

2.8.1 Background

The intense interest in predicting the large strain and high temperature deformation of amorphous poly (ethylene terephthalate) PET owes to its importance as a commodity polymer. For example hot drawing is an integral feature of many industrial processes, including thermoforming, bottle stretch-blow molding and biaxial film drawing. Secondly, the huge advances made in computational capabilities have led to the modeling being an important part of the design process. The constitutive models can be described as being based on either of two approaches: molecular or phenomenological. In the former approach one seeks a physically based model based on thermodynamic and statistical mechanical parameters from the molecular level interactions of the polymer. In the latter a data fitting approach is considered that relies on the existing experimental data.

The experimental data presented in the previous sections demonstrated that the stress–strain behavior (and corresponding evolution in molecular orientation and crystallinity) of PET strongly depends on rate and temperature. This complicated non-linear time-dependent behavior of PET at temperatures above the glass transition has four distinct features: an initially stiff elastic response (slope = E), followed by yielding and flow at low stress level (σ_{yield}), followed by a gradual increase in stress with strain (with initial stiffening modulus h_i), and finally the very large increase in stress with strain at very

large strains (strain hardening). All the above described features were shown to depend upon strain, strain rate and temperature. For PET the strain hardening behavior is more pronounced due to the occurrence of strain-induced crystallization. Therefore strain-induced crystallization is thought of as a mechanism of strain hardening acting in addition to the molecular orientation [102].

It has been documented that the physics of deformation of amorphous PET close to the glass transition involves a flow process constrained by the elastic deformation of an entangled molecular network [103]. This has led to many analytical models of amorphous polymers near T_g based on the assumption that the free energy (and hence stress) consists of two additive components. One is due to local inter- and intra-molecular interactions, and relaxes on an experimental time-scale in the glass transition region (α -relaxation). The other is due to the conformational entropy of the chain molecules. The former dominates volume change at all temperatures and shape change in the glassy region at temperatures below T_g . The latter dominates shape change in the rubbery region immediately above T_g . The entropic stress due to rubber-elasticity does not relax on an experimental time-scale in the glass transition region. Thus, even though not crosslinked, the polymer is rubbery because topological constraints ('entanglements') act as physical crosslinks [104].

This dual form of behavior was first expressed, in one-dimensional form, through a 'glass/rubber' constitutive model by Haward and Thackray [105]. They combined the yield/flow theory with the rubber elastic model to give a unified constitutive description

of yield, drawing and strain stiffening of amorphous polymers. The Haward-Thackray model was extended by Boyce and co-workers to successfully predict the three-dimensional deformation of amorphous polymers in the glassy/rubbery region [106, 107]. In this work they replaced the Eyring yield theory by the Argon ‘double-kink’ model of flow [108].

Subsequently a number of other research attempts to model the stress-strain behavior of amorphous polymers over a large range of strain and temperatures have appeared in the literature [108-114].

2.8.2 Constitutive relationships proposed on basis of molecular structure

The molecular models for all polymers are built upon the idealized underlying structure of randomly oriented polymer chains arranged as a network which resists deformation. In rubbery materials or elastomers, the network is formed by chemical crosslinks between the polymer molecules. In thermoplastics or semi-crystalline polymers such as PET, the network is created by physical entanglements. Since these entanglements are not covalent bonds, the polymer chains exhibit movement by ‘slipping’ through their entanglements under an applied load at elevated temperatures because of increased mobility. The process is called entanglement slippage or reptation [115]. The constitutive models of rubber elasticity were reviewed by Boyce [116] in a comprehensive article. The basic features of stress-strain behavior of elastomeric materials can be modeled either by statistical mechanical treatments as well as by continuum mechanics (invariant-based and/or stretch-based) theories. On the other hand, the physical models capture the intrinsic strain softening by some form of phenomenological law. Some examples of

phenomenological models can be found in the works of Duan et al. [117], G'Sell-Jonas [74] and Zairi et al. [118].

We would not describe every model in detail, but will focus on the models proposed for PET above its glass transition temperature.

Buckley et al. modeled the biaxial hot-drawing of amorphous PET films [104, 108] at fast rates ($> 1 \text{ s}^{-1}$) of stretching. They represented PET as a rubbery network polymer at temperatures of 75-120°C. The basis of their constitutive model was the separation of total free energy in to two contributions: one from the perturbation of intermolecular potentials and the other from conformational entropy. The viscous flow process was modeled on the basis of Eyring yield theory of activated rate process whereas the conformational free energy function was obtained in the form of Edwards-Vilgis expression. Their model could adequately describe only the features of stress-strain behavior for lower temperatures and at intermediate strains. It could not successfully capture the dramatic strain stiffening at large strains or the flow at higher temperatures. This discrepancy between predicted stresses and observed stiffening was identified as originating from a reptation (entanglement slippage) process at higher temperatures and larger draw ratios.

In a later work Adams et al. [119] improved the above model by incorporating an additional component of stretch superposed with the elastic network stretch. This 14 parameter three-dimensional constitutive model could more precisely describe the rate

and temperature dependence of mechanical behavior of PET from glassy region through the rubbery plateau to the terminal region. They observed that the entanglement slippage in their model ceases due to occurrence of strain-induced crystallization at a principal network stretch λ_{max}^n of about 2. However conflicting evidence from online X-ray diffraction data led them to the conclusion that increased topological constraints resulting in the arrest of reptation appear due to the presence of “structural entities” that lack the long-range order of crystals (and, thus, are not crystallites).

In a model for PVC above and below T_g (90°C and 84°C) Sweeney et al. [120] incorporated the Ball network model [121] with a rate dependence by assuming that the number of sliplinks varied with strain rate. In a similar work Matthews et al. [122] for PET above T_g (85°C) described its biaxial drawing by assuming the chain entanglement density to be a linear function of the logarithmic shear strain rate. However their model only worked well until reaching a draw ratio of about 2.2, because of the inability to account for strain-induced crystallization occurring at large strain levels. A model by Vigny et al. [123], for plane-strain stretching of PET at 90°C, employed a power-law type viscoplastic element in addition with an orientational rubber elasticity contribution. The effect of crystallization was accounted for by requiring the apparent number of crosslinks to increase with strain-induced crystallization. The network chain density was expressed as a sum of the density of chains linked at entanglements and chains linked at crystallites, with the latter being a function of strain and strain rate.

More recently, successful molecular constitutive models for the behavior of PET above T_g were proposed by Boyce et al. [102] and Ahzi et al. [124, 125]. These models built upon the assumption that the resistance to deformation of the polymer comes from two molecular mechanisms: a barrier due to intermolecular interactions and an anisotropic resistance due to stretching and orientation of an entropic molecular network. The decomposition of total resistance is schematically represented as shown in *Figure 23*.

The first network (A) represents the intermolecular part and captures the equilibrium response of the material. It was composed of a linear-elastic spring and a viscous element. This resistance contributes to the initial elastic response (spring) and then yielding (viscous dashpot). Yielding was modeled as a thermally activated process [106].

The second network (B) captures the time-dependent flow behavior of the material. It consists of the macromolecular network resistance which causes the strain-hardening behavior resulting from molecular alignment under continued application of stress. The stiffening behavior is captured through a multiplicative decomposition of network resistance into network orientation (non-linear/ Langevin spring element) and molecular relaxation (viscous element) contributions. This means that only a portion of the total applied deformation goes into orienting the macromolecules and the rest is relieved by time and temperature dependent relaxation process. The Langevin spring was modeled on the basis of eight-chain model of Arruda and Boyce [126], while the dashpot captured relaxation in the form of reptation as suggested by Bergstrom and Boyce [127].

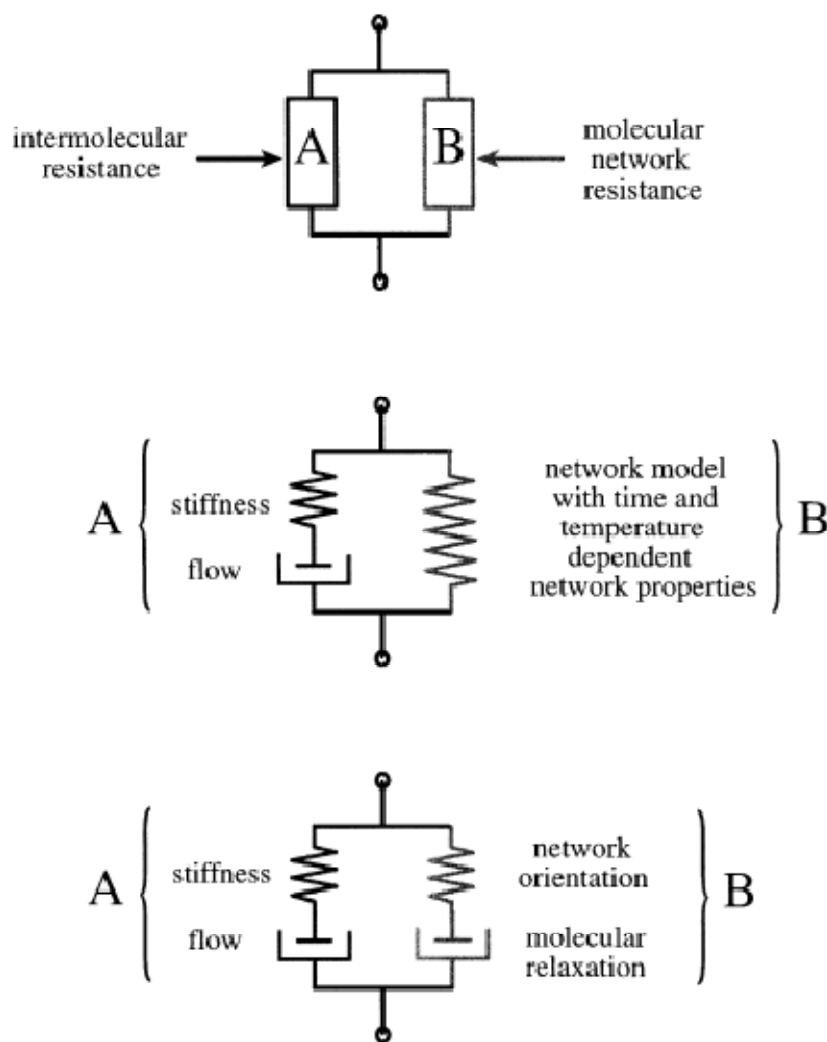


Figure 23. Schematic representation of the breakdown of the total resistance into an intermolecular resistance A occurring in parallel with a network resistance B. The network resistance was modeled as consisting of a molecular relaxation process in addition to a network orientation process (From Ref. 102)

These models incorporated strain-induced crystallization by identifying a level of stretch at which crystallization would occur [128, 129]. In this scheme network A was modeled as increasing with the strain-induced crystallization. Resultantly, reptation ceased and the material exhibited strain hardening. This stiffening is captured by either the evolution of shear resistance [102] or through the evolution of a separate crystalline phase [124].

In their model Ahzi et al. [124, 125] employed a decomposition of intermolecular resistance into amorphous and crystalline phases acting either in series or in parallel with each other as shown in *Figure 24*. The resistance to flow of each of these phases was modeled to increase in the form of a viscoplastic power law. Also the degree of transformation of material from amorphous to crystalline phase with the progress of strain-induced crystallization was explicitly modeled by use of a non-isothermal phenomenological expression based on the modified Avrami equation.

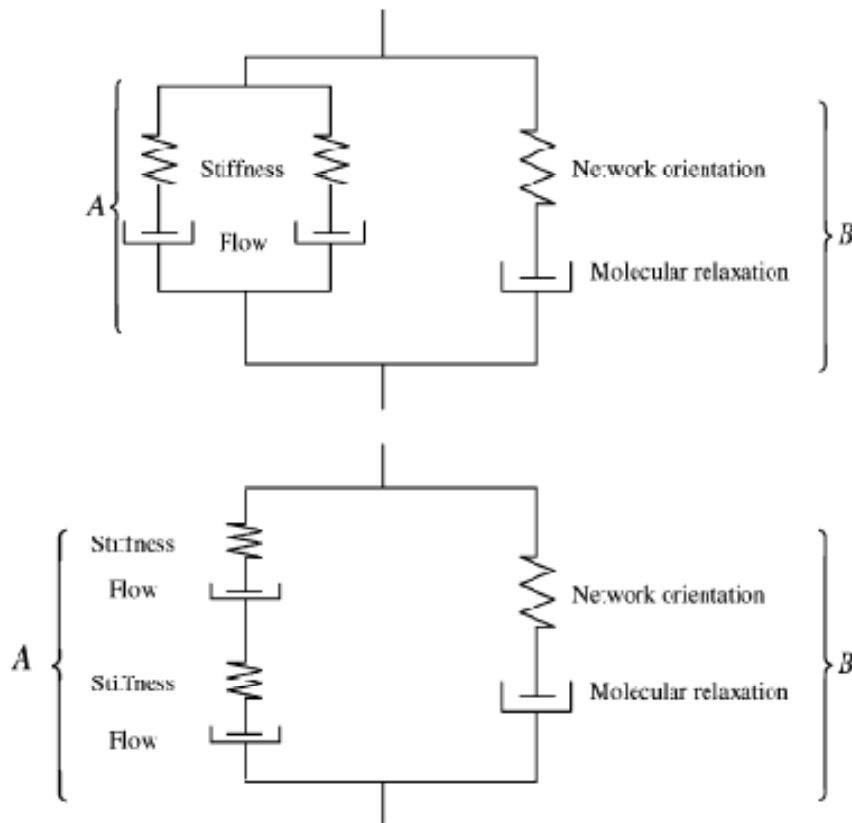


Figure 24. Schematic showing the decomposition of total polymer resistance into an intermolecular resistance (A) acting in parallel with a network resistance (B): (a) Upper bound- intermolecular resistance as a parallel combination of amorphous and crystalline phase stiffness and flow; (b) Lower bound- intermolecular resistance as a series combination of amorphous and crystalline phase stiffness and flow (From Ref. 124)

The above described three-dimensional models were able to successfully capture data over a range of temperatures (all above T_g) and strain rates in different deformation modes.

2.8.3 Mathematical formulations

Based upon the elastic–viscoplastic analog system of *Figure 23* formed with an intermolecular resistance acting in parallel with a network resistance the deformation gradient on each resistance (\mathbf{F}_A and \mathbf{F}_B) is equal to the total deformation gradient (\mathbf{F}) applied to the system:

$\mathbf{F}_A = \mathbf{F}_B = \mathbf{F}$, where the deformation gradient is defined as $\mathbf{F} = \frac{\partial \mathbf{x}}{\partial \mathbf{X}}$.

\mathbf{X} is the reference position and \mathbf{x} the current position of a material point. A and B refer to the intermolecular and network resistance respectively.

The total stress acting on the system (Cauchy stress tensor \mathbf{T}) is equal to sum of the molecular stress \mathbf{T}_A and the network stress \mathbf{T}_B :

$$\mathbf{T} = \mathbf{T}_A + \mathbf{T}_B \quad (35)$$

2.8.3.1 Intermolecular resistance

The molecular resistance to deformation was modeled as a linear spring in series with a viscous element in the above model. The initial linear response is attributed to van der Waal interactions between chain molecules. After a certain critical stress level, the energy barrier to molecular chain segment rotation is overcome and flow starts. This led to the decomposition of the deformation gradient into elastic and plastic components:

$$F_A = F_A^e F_A^p; F_A^e = V_A^e R_A^e; F_A^p = V_A^p R_A^p \quad (36)$$

where V and R are the left-stretch and the orthonormal rotation tensors, respectively, for each constituent.

The velocity gradient of resistance A is $L_A = \dot{F}_A F_A^{-1}$

$$L_A = \dot{F}_A^e F_A^{e^{-1}} + F_A^e \dot{F}_A^p F_A^{p^{-1}} F_A^{e^{-1}} = L_A^e + \tilde{L}_A^p \quad (37)$$

where \tilde{L}_A^p is formed by using the transformation rule for a tensor $[K][M][K]^{-1} = [\tilde{M}]$

and noting that $L_A^p = \dot{F}_A^p F_A^{p^{-1}}$. Let $\tilde{L}_A^p = \tilde{D}_A^p + \tilde{W}_A^p$ where \tilde{D}_A^p is the rate of stretch tensor and \tilde{W}_A^p is the spin tensor for the plastic component. If the spin tensor is assumed to be zero i.e., $\tilde{W}_A^p = \mathbf{0}$ there will be rotation in both the elastic and plastic deformation gradients.

The rate of plastic stretching was expressed as:

$$\tilde{D}_A^p = \dot{\gamma}^p \frac{\dot{T}_A}{\sqrt{2}\tau_A} \quad (38)$$

Here \dot{T}_A is the deviatoric part of the total network stress T_A and τ_A is the effective shear stress on the crystalline phase as below:

$$\tau_A = \left[\frac{\dot{T}_A \cdot \dot{T}_A}{2} \right]^{1/2} \quad (39)$$

The rate of viscous flow for element A was assumed to be a thermally activated process following an Arrhenius type relationship:

$$\dot{\gamma}_A^p = \dot{\gamma}_{0,A} \exp \left[\frac{-\Delta G \left(1 - \frac{\tau_A}{s} \right)}{k\theta} \right] \quad (40)$$

where $\dot{\gamma}_{0,A}$ is the reference shear rate, ΔG is the activation energy of flow, k is the Boltzmann constant and θ is the absolute temperature.

The constitutive relationship between stress and deformation was given as:

$$\mathbf{T}_A = \frac{\mathbf{C}^e}{J_A} [\ln(\mathbf{V}_A^e)] \quad (41)$$

Here \mathbf{C}^e is the fourth order tensor of elastic constants, $\ln V_A^e$ is the Hencky strain and $J_A = (\det F_A^e)$ is the volume change.

2.8.3.2 Network resistance

The equations for this resistance were obtained in a manner similar to the intermolecular resistance:

$$\mathbf{F}_B = \mathbf{F}_B^N \mathbf{F}_B^F, \mathbf{F}_B^N = \mathbf{V}_B^N \mathbf{R}_B^N \text{ and } \mathbf{F}_B^F = \mathbf{V}_B^F \mathbf{R}_B^F \quad (42)$$

The rate kinematics for resistance B was then prescribed similar to A.

The velocity gradient of resistance B: $\mathbf{L}_B = \dot{\mathbf{F}}_B \mathbf{F}_B^{-1}$

$$\mathbf{L}_B = \dot{\mathbf{F}}_B^N \mathbf{F}_B^{N^{-1}} + \mathbf{F}_B^N \dot{\mathbf{F}}_B^F \mathbf{F}_B^{F^{-1}} \mathbf{F}_B^{N^{-1}} = \mathbf{L}_B^e + \tilde{\mathbf{L}}_B^F \quad (43)$$

where $\tilde{\mathbf{L}}_B^F = \tilde{\mathbf{D}}_B^F + \tilde{\mathbf{W}}_B^F$. Again the spin tensor $\tilde{\mathbf{W}}_B^F$ was assumed to be zero. The rate of molecular relaxation is contained in $\tilde{\mathbf{D}}_B^F$.

The stress on molecular network is based upon the non-Gaussian eight-chain network model proposed by Arruda-Boyce [126]. In this model each chain deforms by a stretch $\bar{\lambda}_N$ as a function of the applied distortional stretches:

$$\bar{\lambda}_N = \left[\frac{1}{3} \text{tr} \left(\bar{\mathbf{F}}_B^N \bar{\mathbf{F}}_B^{NT} \right) \right]^{1/2} \quad (44)$$

where $\bar{\mathbf{F}}_B^N = \frac{\mathbf{F}_B^N}{(J_B)^{1/3}}$ and $J_B = (\det \mathbf{F}_B^N)$.

The total network stress was expressed as:

$$\mathbf{T}_B = \frac{1}{J_B} \frac{nkT}{3} \frac{\sqrt{N}}{\bar{\lambda}_N} L^{-1} \left[\frac{\bar{\lambda}_N}{\sqrt{N}} \right] \left[\bar{\mathbf{F}}_B^N \bar{\mathbf{F}}_B^{NT} - (\bar{\lambda}_N)^2 \mathbf{I} \right] \quad (45)$$

where N is the limiting stretch ratio on each chain (or the number of ‘rigid links’ between entanglements), n is chain density and L^{-1} is the inverse Langevin function $L(x) = \coth(x) - 1/x$. The term $nkT/3$ represents the initial strain hardening modulus of a rubbery network. The origins of network resistance can be found in the classical rubber elasticity theory for crosslinked rubbery networks. In case of PET, the entanglements act as physical tie points or crosslinks.

The rate of molecular relaxation was described as

$$\tilde{D}_B^F = \dot{\gamma}_B^F N_B \quad (46)$$

where N_B is the normalized deviatoric stress on element B:

$$N_B = \frac{T'_B}{\sqrt{2}\tau_B}; \quad \tau_B = \left[\frac{T'_B T'_B}{2} \right]^{1/2} \quad (47)$$

T'_B is the deviatoric part of the total network stress \mathbf{T}_B and τ_B is the effective shear stress.

The network relaxation rate for element B is given by

$$\dot{\gamma}_B^F = C \left[\frac{1}{\lambda_F - 1} \right] \tau_B, \quad \lambda_F = \left[\frac{1}{3} \text{tr}(\mathbf{F}_B^F \mathbf{F}_B^{FT}) \right]^{\frac{1}{2}} \quad (48)$$

and C is a parameter that contains temperature dependence of relaxation through an Arrhenius type relation. Here the effective relaxation rate was obtained from the theory presented by Bergstrom and Boyce in their work [127]. They described the relaxation process as a stress-assisted Brownian motion of elastically inactive chain segments of the network molecules. They defined ‘inactive segments’ as those parts of the long network chains which can undergo non-recoverable deformation under applied stress. Based on this mechanism, relaxation of the network was considered to be energy activated process and therefore contains the parameter C as defined below:

$$C = D \exp\left(\frac{-Q}{RT}\right) \quad (49)$$

where T is the absolute temperature, R is the universal gas constant and D and Q are constants determined from stress-strain data.

2.9 On the elastic moduli of the amorphous and crystalline phases of PET

The amorphous region with a smaller modulus has the prevalent influence on the macroscopic elastic modulus of the fiber than that of the crystalline region. This is because of the effect of imperfect orientation of the crystalline and amorphous regions along the fiber axis, as well as the number and fraction of tie molecules [130].

The elastic modulus of a semi-crystalline material is generally calculated using the two-phase model assuming the homogeneous stress distribution in the material. It is based on the series coupling of crystalline and amorphous domains with the assumption that there

is no interfibrillar material present between those domains. This model is more applicable to displacement of crystals relative to each other and is essentially more precise if there are no spherulitic or rod-like entities within the microstructure [131]. In this structural model the crystalline and amorphous phases lie alternately along the fiber axis, and the fiber compliance can be obtained from the additive rule as [132]:

$$\frac{1}{E_f} = \frac{X_c}{E_{c\equiv}} + \frac{1-X_c}{E_a} \quad (50)$$

where E_f is the fiber modulus, $E_{c\equiv}$ is the crystal modulus along the fiber axis, E_a is the amorphous modulus and X_c is the volume crystallinity. It is clear from the above expression that fibers may possess a different E_a value although they might have the same crystallinity, the individual fiber microstructure affecting its magnitude. This expression based on the series model has been extensively used in the literature [130, 133, 134].

The use of a three-phase model has been considered by many authors, particularly for application to PET fibers spun at high speeds and PET films. In their work Peng et al. [135] used a three-phase “series-parallel” model and a two-phase “series-aggregate” model for calculating the modulus of high-speed spun PET fibers. The former was based on the properties of inter- as well as intra-fibrillar material whereas the latter was a simpler one that only indirectly considers the amorphous phase influence. In the three-phase model an amorphous phase exists both in series (intrafibrillar chains) and in parallel (interfibrillar chains) to the crystallites. In the two-phase model the fiber was modeled as a collection of “aggregates” or crystallites separated by disordered blocks and it was found to be more closely applicable to the PET fibers in question. Bin et al. [136] used the generalized orientation factors of crystallites and amorphous chain segments to

estimate the elastic modulus of PET films based on the two-phase model in which ‘the anisotropic crystal phase is surrounded by the anisotropic amorphous phase’.

The PET crystalline phase elasticity constant (E_c or crystal modulus) has been measured by various workers using different experimental techniques and different methods of calculation. Tashiro, in his review concerning the determination of elastic constants of polymer crystals, has argued that the determined value of crystal modulus varies largely due to the various types of stress-distribution models employed [137].

The value of E_c at room temperature reported in literature varies from 95 GPa to 146 GPa. The value of 110 GPa was suggested to be more accurate by Thistlethwaite [138] based on the parallel-series model which was applied to the SAXS crystal modulus and fiber modulus (E_Y) measurements:

$$E_Y = \frac{\lambda}{\frac{\varphi}{E_c} + \frac{1-\varphi}{E_a}} + (1 - \lambda) \cdot E_a \quad (51)$$

where E_c is the elastic constant of crystalline phase of PET and E_a is the elastic constant of amorphous phase of PET. The parameter φ is the ratio of the mean crystallite length (L) to the long period (LP) of the material and λ is defined as (crystallinity/ φ), as shown in *Figure 25*.

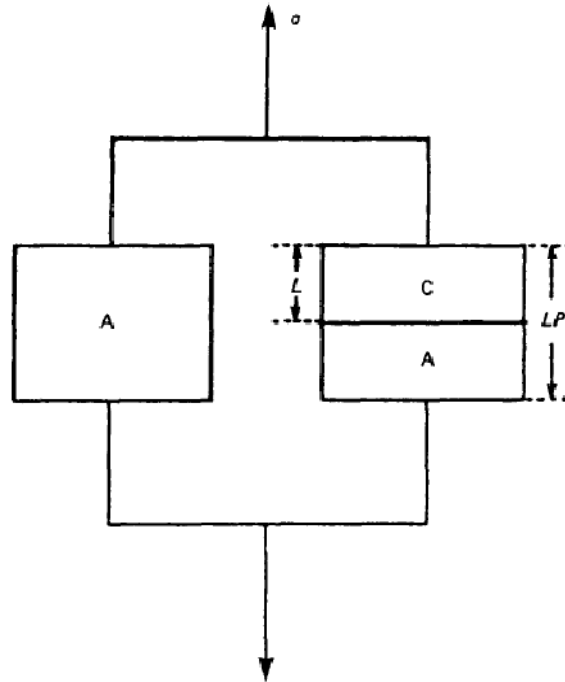


Figure 25. The schematic representation of the parallel-series model (From Ref. 138)

It is assumed that the crystal modulus of PET is a function of temperature, as demonstrated in many studies including one by Bin et al. [136] and Nishino et al. [139].

The determination of fiber modulus and its relationship with crystal modulus has been experimentally investigated by many authors. It has been demonstrated in numerous papers [130, 133, 134, 138, 140, 141] that the Young's modulus of fibers is about 15-17% of the intrinsic crystalline modulus value due to low crystallinity. The literature has also shown that the Young's modulus of amorphous phase of fibers E_a is about 50% of the overall fiber modulus E_f [130, 133, 138, 140].

2.10 Literature review summary

The formation of PET fibers via the melt spinning process was discussed. The differences between conventional and high-speed spinning were reviewed. The effects of speed of spinning on the superstructure development were reviewed in detail in relation to the mechanical properties of fibers. The necking phenomenon is an important part of the high speed spinning process and was discussed in conjunction with the strain-induced crystallization phenomenon. Literature review shows that PET in the amorphous state undergoes an entropically driven process of crystallization called stress/strain-induced crystallization (SIC) during drawing. Experimental evidence was presented to show that SIC may occur during drawing depending on the drawing conditions. The research attempts to describe SIC in quantitative and qualitative terms were reviewed. However many studies have also shown that it is possible to avoid SIC by carefully choosing drawing parameters. If SIC is negligible, the changes in structure are insignificant owing to the absence of hardening mechanisms. The resultant product is nearly similar in crystallinity and orientation to the original fiber and therefore assumed to have been superdrawn.

The effects of drawing parameters on the structural evolution were reviewed. Two parameters namely temperature and strain rate were identified as critical factors that can affect the orientation and crystallinity development in drawn samples. The effect of those two factors on the structural changes at the molecular level was discussed in detail. In this perspective, the potential regime of drawing parameters was identified, where superdrawn samples could possibly be obtained. The extensive studies in the literature,

both experimental and theoretical, concerning the crystallization behavior during drawing, stress-strain curves at different drawing conditions and dynamic mechanical behavior of PET fibers were comprehensively reviewed. It was found that a better understanding of the crystallization mechanism during superdrawing of fibers is needed. An extensive experimental work on the fiber stress-strain behavior during uniaxial extension in a large range of temperature and strain rates would enable us to pursue this goal.

The problem of crystallization rate both in the absence and presence of stress was discussed in detail. The crystallization theories for quiescent crystallization (nucleation and growth theory) were presented. The presence of large stresses, as in high-speed spinning, or large amounts of supercooling results in crystallization behavior that cannot be explained by nucleation and growth theory. This led to the development of theories of SIC which were reviewed. The description of kinetics of crystallization (quiescent and SIC) was also given. The crystallization rate largely governs the amount of crystalline domains formed in a deformed sample, e.g. a drawn fiber.

The constitutive relationships to capture the non-linear viscoelastic behavior of amorphous glassy polymers in general, and PET in particular, were discussed in detail. The successful molecular models have been formed on the basis of addition of the contributions of intermolecular resistance and network resistance to the total stress in the polymer. Both resistances are modeled as being comprised of an elastic and a plastic part. The mathematical expressions to formulate the stress-strain relationship were also

explained. Although there are several existing models (statistical-mechanics based or continuum-mechanics based) for deformation of PET, a model for fiber drawing process with *insignificant* crystallization and orientation is lacking. Thus the previous research has been modified to develop a new fiber drawing model that can best predict the stress-strain behavior under the superdrawing conditions of this study.

Finally, the methods of determination of fiber and crystal modulus of PET were discussed. The different mechanical models (e.g. series, series-parallel) used for this purpose were reviewed. It was found that a three-phase model (the parallel-series model) is able to capture the experimentally determined modulus values of PET more precisely. This fundamental form of mechanical coupling has been used in the new constitutive model to follow the evolution of fiber modulus with the occurrence of crystallization.

It is evident from literature review that a detailed study involving mechanical tests of fibers followed by microstructural analysis on the deformed samples can provide insight into the structural evolution and crystallization mechanisms in PET fibers. These tests will be used to optimize the conditions for a stable superdrawing process which can improve fiber processing efficiency in ultrafine and hollow fiber production processes. Literature review also showed that strain-induced crystallization phenomena in such a large range of fiber drawing conditions are not well characterized nor are they well modeled. Thus a new modified model will be built by adapting the existing modeling approaches to closely predict the observed stress-strain behavior under experimental conditions of this study.

CHAPTER 3

OBJECTIVES

3.1 Motivation

PET is one of the most successful polymers used as fibers in a wide range of applications from apparel to industrial yarns. In PET fiber drawing, the initial state is an amorphous, slightly oriented polymer obtained by melt-spinning at low speeds (≈ 3000 - 4000 m/min.). The drawing process causes a preferential orientation of the underlying molecular network, which, under certain conditions such as necking, leads to strain-induced crystallization. The level of molecular orientation and degree of crystallinity attained during stretching strongly depends upon rate and temperature. The dependence of the stress-strain behavior of PET on these processing parameters has been discussed in detail in literature and presented in preceding sections. It is important to fully understand the evolution in molecular alignment and crystallinity to control the quality and properties of the end-product.

3.2 Research plan

3.2.1 Scope of study

Though a lot of research has been done to study the crystallization behavior of amorphous PET during stretching, limited amount of work has been done to find the exact range of temperature (T) and strain rate ($\dot{\epsilon}$) suitable for superdrawing of fibers. In

particular, the mechanism of crystallization (or the lack thereof) during superdrawing of fibers is not fully understood. The drawing behavior of fibers has been shown by various researchers to be dependent upon temperature and strain rate. However, the complex role that these two factors play during fiber drawing is not fully understood. Salem [15-17, 31, 32, 142] has shown that effect of temperature greatly depends upon the range of strain rate being used. He predicted that temperature will help crystallization to occur if the strain rates are high enough ($\approx 10^0 \text{ s}^{-1}$). But this phenomenon was observed in a relatively narrow range of temperature (83-96°C) and has never been verified by other authors. This study is an attempt to experimentally determine the role of strain rate and temperature in strain-induced crystallization phenomena, over a large range of strain rate and temperature, which has not been reported in earlier work.

Moreover it is important to study the regime of strain rate where temperature effect is to minimize crystallization, so that flow drawing can happen. Therefore one of the objectives of this research is to fully understand and model the effect of temperature in different strain rate regimes during drawing of amorphous PET fiber. Literature review also showed that temperature induced crystallization above the glass transition is a process driven by the tendency of underlying molecular network to return to a maximum entropy state and it will always happen during drawing limiting the final draw ratio. In order to obtain very large draw ratios it is critical to find how cold crystallization behavior of PET changes under different temperature-strain rate conditions. This is another objective of this research.

Literature review showed that constitutive relationships for predicting the large strain stress-strain behavior of PET at different temperatures above the glass transition are well developed and successfully modeled. However the absence of crystallization and orientation, inherent to superdrawing, still needs to be modeled explicitly. Therefore the other objective of this research is to model the superdrawing behavior as well as to predict the large strain mechanical behavior observed under the large range of processing conditions employed in this study.

3.2.2 Process conditions for superdrawing

We must deal with several technical issues in order to realize an efficient and smooth superdrawing process. Also we need to fully understand many fundamental factors such as the constitutive equations relating stress-strain and the effect of temperature and strain rate on these relationships. Even though these factors have been investigated by many authors, there is not yet a clear, established mechanism of superdrawing process. Therefore it will be very useful to study the relations between these factors and be able to predict the superdrawing behavior based upon those factors. If drawing occurs through necking the associated strain-induced crystallization (SIC) causes strain hardening during deformation during which alignment of polymer chains occurs, giving rise to higher overall crystalline content as well as orientation. Evidently a process with negligible SIC is needed to obtain superdrawn samples.

As shown in earlier works, a fiber with low initial orientation has a molecular configuration of random interpenetrating coil-like chains. There are a lot of entanglements between molecular segments of the coils. If the applied force is low and

the temperature sufficiently high, deforming such a fiber at a slow rate will cause disentanglement and the coils will move apart [29]. After continued deformation, more and more molecular chains will physically separate leading to a ductile failure of the material. This behavior will cause the fiber draw to proceed without any significant orientation or crystallization. If molecular mobility is decreased by decreasing the temperature or increasing deformation rate, the disentanglement can not occur in all coils leading to retractive forces. With higher strain rates, the disentanglement will become even scarce, thereby leading to a large-scale cooperative motion. Such conditions will possibly favor crystallization and eventually lead to a brittle failure. In other words the conditions for superdraw must be such that amorphous orientation remains below a certain level, f_{am}^0 , so that there is very little strain-induced crystallization. By increasing the temperature, we can avoid significant segmental orientation, but thermal crystallization (“cold crystallization”) rate would be higher too. Thus, a trade-off between the two parameters will give us a critical deformation rate-temperature combination at which the drawing of PET fiber results in little or no crystallization.

3.3 Specific Goals

The first goal of this study is to understand the role of temperature and strain rate in the drawing of PET fibers. The second objective of this study is to understand the mechanisms of crystallization of PET fibers during superdrawing. The third goal of this project is to develop a stable superdrawing process for PET fibers. The fourth goal of this study is to model the stress-strain behavior of PET fibers. Specifically this research has the following objectives:

- (a) Determination of the range of temperature and strain rate (parameter window) to achieve superdrawing of amorphous PET fibers.
- (b) Elucidating the deformation mechanism during superdrawing and establish a unified physical mechanism of superdrawing process.
- (c) Understanding drawing kinematics of fibers- for a range of temperatures and strain rates.
- (d) Developing a constitutive model to capture the stress-strain behavior of amorphous PET at large strains above T_g at various rates of deformation.
- (e) To capture the highly non-linear strain softening/hardening features observed in the experimental results.

These objectives are achieved by:

- Conducting uniaxial drawing tests at a wide range of strain rates and temperatures.
- Performing a differential scanning calorimetry (DSC) study on drawn samples to investigate their cold crystallization behavior and to confirm that structure has not changed significantly.
- Performing birefringence measurements with a polarized microscope to deduce the orientation development in drawn samples.
- Developing a model for PET based on different approaches in the literature.
- Determining the validity of the constitutive model for PET by comparison with the uniaxial tensile data over the range of experimental parameters involved in this study.

CHAPTER 4

EXPERIMENTAL STUDIES

Since the mechanical response (the stress-strain curve) of a material is a direct manifestation of the intermolecular interactions during the process of drawing above T_g , it is useful to study the structural development from the stress-strain curves at different conditions. These tests were followed by DSC and birefringence measurements. The types of samples used and their important properties are summarized in *Section 4.1*. *Section 4.2* first examines the set up of uniaxial drawing tests and then the stretching behavior of PET under regimes of strain rates and temperatures. In the next section the superdrawing behavior is analyzed by thermal studies made on the DSC. Based on those results, a ‘window’ of superdrawing of PET is proposed in terms of temperature and strain rate. In *Section 4.4* results of birefringence measurements are analyzed and utilized as an evidence to confirm the boundaries of superdrawing determined by tensile and thermal studies.

4.1 Materials

The materials used for this study were PET fibers spun at a spinning speed of 500 m/min. with an intrinsic viscosity of 0.65 dL g^{-1} in o-chlorophenol at room-temperature (see Table 2). The glass transition temperature (T_g) of the as-spun material is 79°C , as measured by DSC at 10°C/min . The small birefringence value shows that the PET filaments have very little molecular orientation. The slow spinning speed also leads to the formation of a disordered structure in absence of large spinline stresses.

Table 2. Description of the fiber samples used

Spinning speed	Avg. denier/filament	I. V. (dL/g) [±]	Mean Diameter (μ m)	Birefringence
500 m/min.	41	0.60	65	0.0025

±: 25°C, OCP

The tensile properties of the fibers at 25°C were measured on Instron tensile tester. The results were averaged over five tests on five different samples and are summarized in Table 3. As evident from the elongation at break, the fibers have a poorly organized, amorphous network of chains.

Table 3. Tensile properties of the as-spun fibers at room-temperature and strain rate of 0.083 s⁻¹ (5 inches min⁻¹)

Break Strain, %	Break Load, g/d	Break Stress, MPa	E, GPa	Yield Stress, MPa	Yield Strain, %
948.4 (190.5) [±]	0.82 (0.004) [±]	99.07	1.17	58.09	3.25

±: quantity in brackets is standard deviation

The thermal properties of the as-spun fibers were studied with Seiko 220 DSC differential scanning calorimeter and are summarized in Table 4.

Table 4. Thermal properties of the as-spun fibers measured on Seiko 220 DSC at a heating rate of 10°C min⁻¹

T _g (°C)	T _{c_onset} (°C)	T _c (°C)	ΔH _c (J/g)	X _c (%)	T _{m_onset} (°C)	T _m (°C)	ΔH _m (J/g)
79	122	141	26.64	6.28	240.1	255.9	35.43

The low crystallinity value and the presence of a prominent cold crystallization peak indicate that the PET filaments are amorphous.

4.2 Stress-strain curves during uniaxial stretching of amorphous PET fibers at different temperatures and strain rates

4.2.1 Methodology

To understand the drawing kinematics, uniaxial drawing experiments were performed at constant strain rates on an Instron tensile testing machine inside a specially designed temperature chamber, as shown in Figure 1. The temperatures of 120, 115, 110, 105 and 90°C and eight strain rates ranging from 8×10^{-3} to $4.25 \times 10^{-1} \text{ s}^{-1}$ were used. The data reported here is an average of five tests. The drawn samples were classified as superdrawn or non-superdrawn based upon a study of their molecular structure by analyzing their crystallinity and orientation.

4.2.1.1 Drawing apparatus

An Instron tensile testing machine was employed for measuring the load-strain curves. An insulated hot chamber was fabricated for hot drawing of samples and fitted to the Instron machine. The precision control of temperature was achieved by a PID controller with feedback loop connected to a heating element. The temperature inside the drawing zone was maintained with an accuracy of $\pm 1.5^\circ\text{C}$ up to 150°C . The chamber was fitted horizontally for drawing with the Instron machine (see *Figure 26*). Each sample was prepared as a fiber bundle consisting of 68 single filaments since a single PET filament has too low a strength to be tested. Each end of the sample was glued to a small metal hook each of which is in turn connected to a Kevlar yarn that can freely move through the chamber by use of guide rollers. The sample was thus connected through the hooks and the Kevlar yarn to Instron load-cell at one end and fixed to the ground at other end.

Initially the sample is mounted on the hooks and kept outside the chamber. When the desired temperature reached a stable state, the sample was jogged quickly into the chamber. Then the string is fixed on the metal stand and the tensile test started immediately. As the test is finished, the sample is immediately taken out of the chamber and cooled to room temperature to preserve the structure in drawn sample.

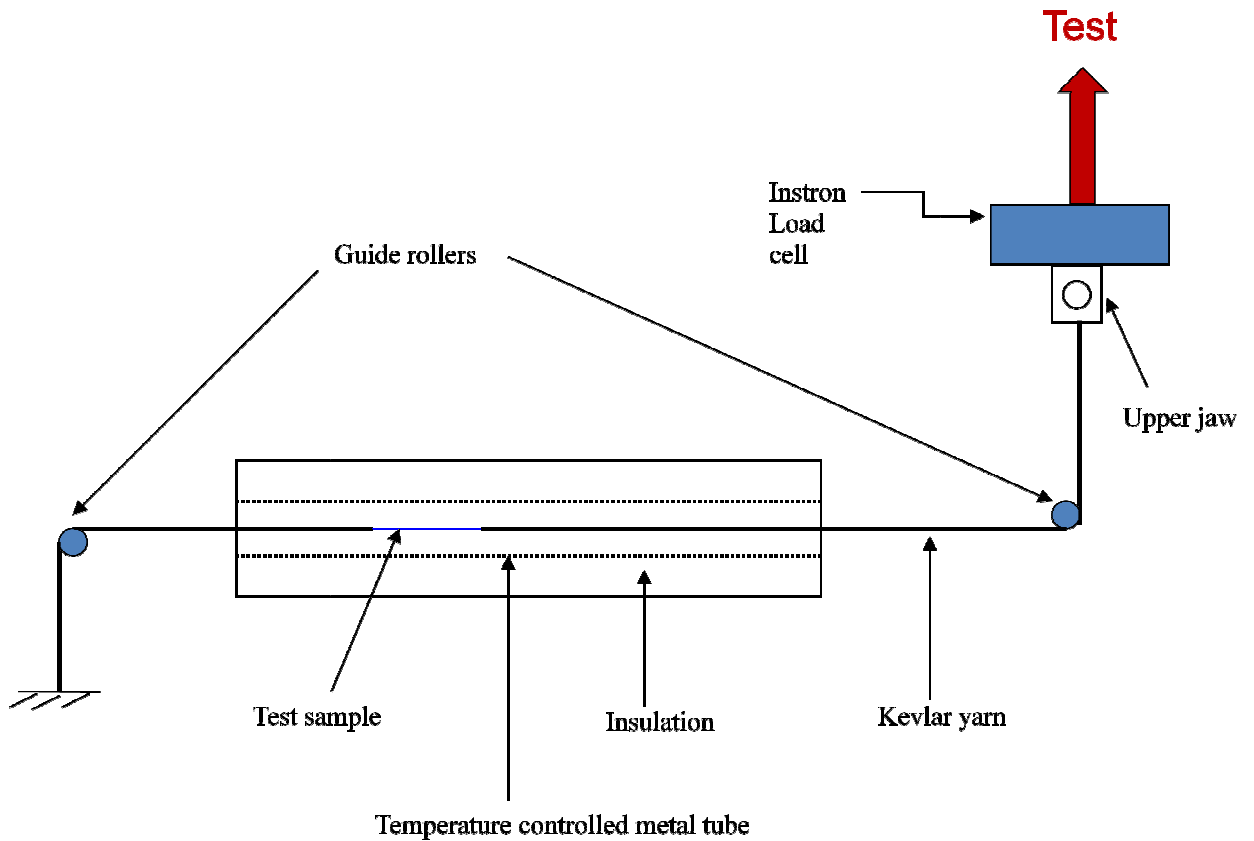


Figure 26. A schematic drawing of the insulated chamber along with the sample attached to the Instron for hot drawing of PET samples

4.2.2 Effect of temperature on the drawing behavior as a function of strain rate

During the uniaxial stretching of PET fibers, two distinct aspects of the stress-strain behavior can be observed as schematically shown in *Figure 27*. The type-I behavior is usually associated with low temperature and high strain rates while the type-II behavior is

commonly observed at relatively higher temperature and lower strain rates. The type-I deformation behavior involves strain-induced crystallization (SIC) and relatively high drawing stress with a finite extensibility. On the other hand, type-II behavior is seen as a flat curve with no distinct features except an initial linear region.

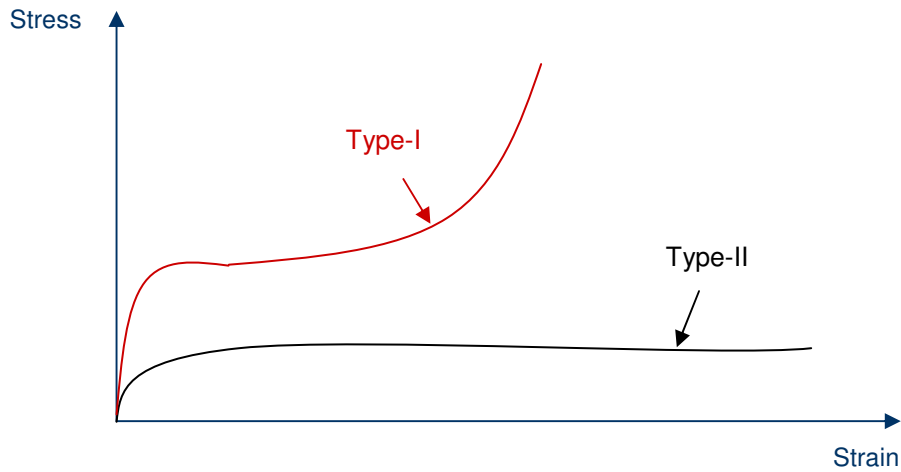


Figure 27. A schematic illustration of the types of mechanical response of PET fibers observed under different stretching conditions

Figure 28 shows the stress-strain behavior of PET at a draw temperature of 90°C and strain rates ranging from 0.008 to 0.425 s⁻¹. Three distinct regions can be identified at all strain rates: an initial Hookean region with linear stress-strain relationship followed by yield and finally a dramatic strain hardening. Thus the strain hardening in the final stages causes disruption of drawing by breakage of the sample.

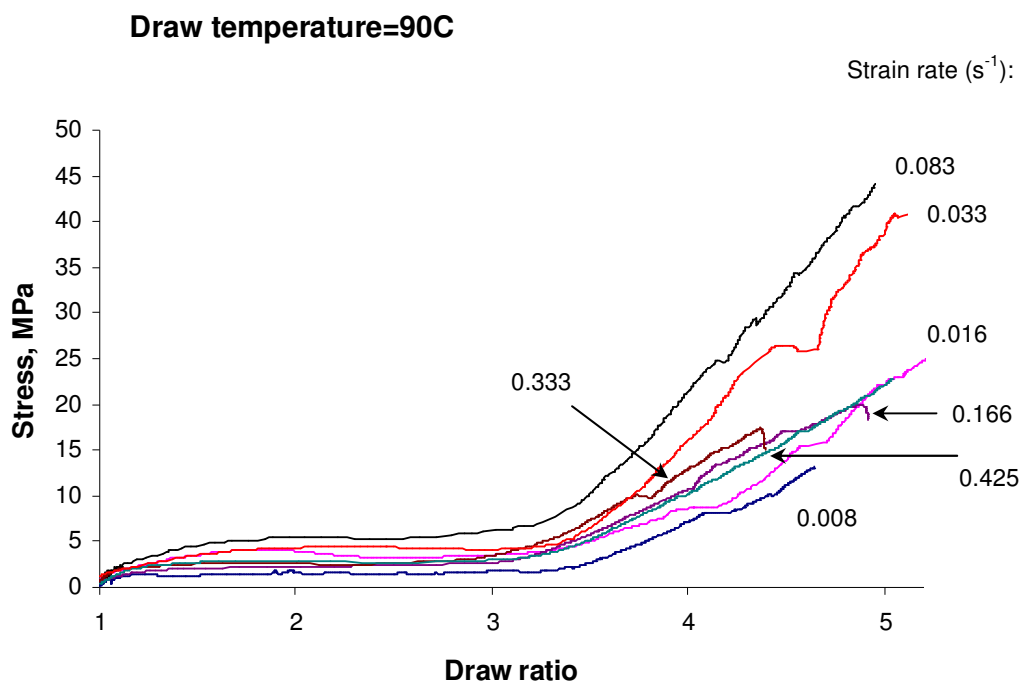


Figure 28. Stress-strain curves, until failure, at 90°C showing the type-I draw behavior that leads to non-superdrawn samples. Different strain rates are indicated

A steep rise in the drawing stress occurs at a strain equal to 2 at all strain rates, meaning the critical draw ratio is 3.0 for drawing at 90°C. This behavior is a type-I stress-strain curve. The type-I behavior is also seen in *Figure 29* at 105°C at a strain rate of 0.425 s^{-1} and in *Figure 32* at 120°C at a strain rate of 0.008 s^{-1} .

The stress-strain curves of PET obtained at a draw temperature of 105°C are shown in *Figure 29*. For 0.333 and 0.425 s^{-1} the stress-strain curves exhibit an initial elastic response followed by flow and finally dramatic upturn in stress values due to hardening, similar to that at 90°C. But for all strain rates up to 0.166 s^{-1} the mechanical behavior involves an initial elastic response followed by yield followed by flow with no stiffening.

During this type of drawing the material can be extended to very large draw ratios under a low deformation stress, without any necking since there is no SIC during the test.

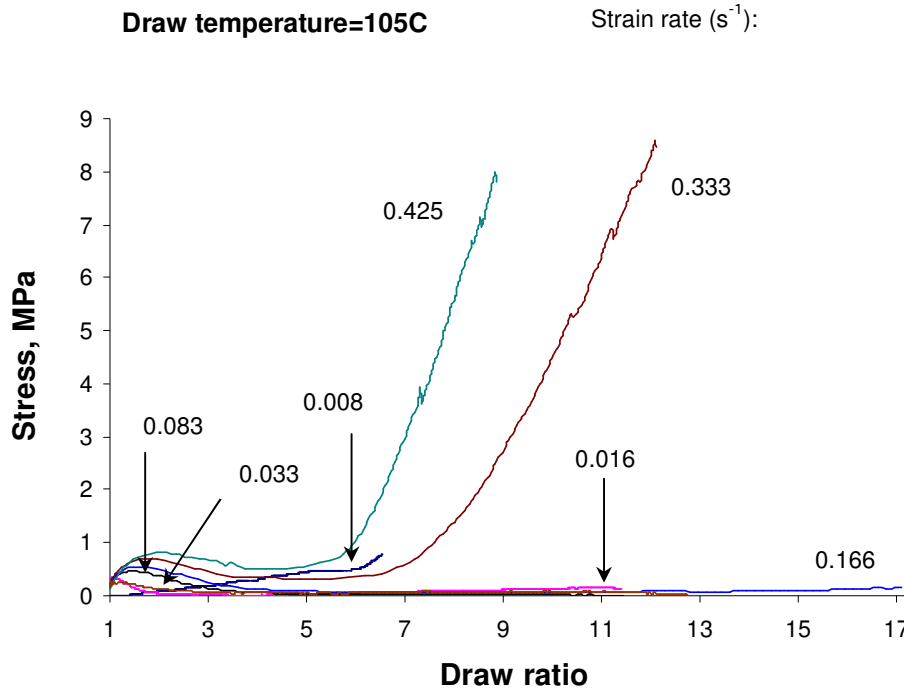


Figure 29. Stress-strain curves, until failure, at 105°C showing the type-II drawing behavior at small strain rates that leads to unoriented superdrawn samples. Type-I behavior is observed at the fastest strain rates of 0.333 s⁻¹ and 0.425 s⁻¹

Since the draw ratios obtained with type-II process are much larger than those in a conventional drawing (or type-I) process, those samples are called superdrawn samples.

The type-II drawing behavior can be explained from the well known fact that because of the very small orientation, the amorphous PET fibers can be described as a network of stochastically entangled chains with a molecular configuration of interpenetrating random coils. Since the process temperature is much higher than the glass transition of the polymer, the molecular mobility increases. The initial stage of deformation consists of entanglement slippage at a low load since rupture of physical cross links occurs in this

process. Chain disentanglement continues until yield point after which the intermolecular interactions get lower and the molecular chains can then move apart from each other. With further deformation the force on each chain causes molecules to become oriented at a certain rate. However, under these conditions it is thought that deformed chains are able to relax at a sufficiently high rate and get enough time to recover their random states, causing an offset or decrease of molecular orientation achieved until then by deformation. The SIC under these conditions is hindered because a low level of molecular orientation does not allow the configurational and conformational entropy to decrease thereby resulting in a negligible driving force for crystallization. Under the aforementioned conditions, therefore, the chains continuously undergo a physical separation or slippage resulting in a large extension of the fiber until a ductile fracture occurs [7, 29]. Note that there may be a global orientation of chains present in these samples despite a negligible local orientation as suggested by Radhakrishnan and Gupta [37].

The dramatic shift in drawing behavior with temperature and strain rate (SIC at all stretching rates at 90°C; but flow draw at all rates except at 0.333 s⁻¹ and 0.425 s⁻¹ for 105°C) is useful from the viewpoint of understanding the superdrawing mechanisms in PET. The drawing associated with SIC is expected to occur at low temperature/high strain rate and consist of the three basic features of stress-strain curves of PET as described in *Section 2.1*. The SIC that leads to high draw stresses occurred in the final stages at large deformations (at $\lambda=3$ for 90°C/0.008 s⁻¹ and at $\lambda=5$ for 105°C/0.425 s⁻¹). The molecular phenomena occurring at large draw ratios are discussed below in detail because they can help us understand the superdrawing behavior more completely.

During high temperature drawing of PET two opposite phenomena are simultaneously occurring. The applied forces cause molecular alignment by shearing them apart and the molecular chains tend to relax and return to their original coil states in order to be in the maximum entropy state. Thus it is a dynamic process involving orientation and relaxation which occurs repeatedly and instantaneously in the whole material as the drawing continues. It is safe to assume that any crystallization during drawing is driven by thermodynamic forces of entropic origin. Based on this assumption, if the rate of disorientation by molecular relaxation is fast enough to prevent molecular orientation from crossing a certain threshold value, the SIC will be suppressed. Thus at the critical large deformation stage the temperature and strain rate become the decisive factor to determine whether or not SIC takes place. The type-II behavior, for example, involves no SIC and expectedly occurs with increasing temperature *and* a low strain rate as shown in *Figure 29* at $105^{\circ}\text{C}/0.008\text{ s}^{-1}$. On the other hand, as seen in *Figure 28* at 90°C , SIC occurs if molecular alignment dominates over relaxation and comparatively smaller draw ratios are obtained. By similar reasoning the type-I behavior is also observed at a temperature higher than 90°C if strain rate is high, e.g., as seen in *Figure 29* at $105^{\circ}\text{C}/0.425\text{ s}^{-1}$.

As the drawing temperature was increased to 110°C , the draw stress went down considerably (*Figure 30*) for all strain rates. The highest strain rates resulted in somewhat higher draw stress than the lower rates. Evidently from *Figure 30* the draw behavior at 110°C could be roughly categorized into two distinct types. At the two slowest strain rates it was found that there is no yielding and an initial response that grows into gradual

stiffening. But all the faster rates show an initial elastic response followed by yield and finally flow with no stiffening.

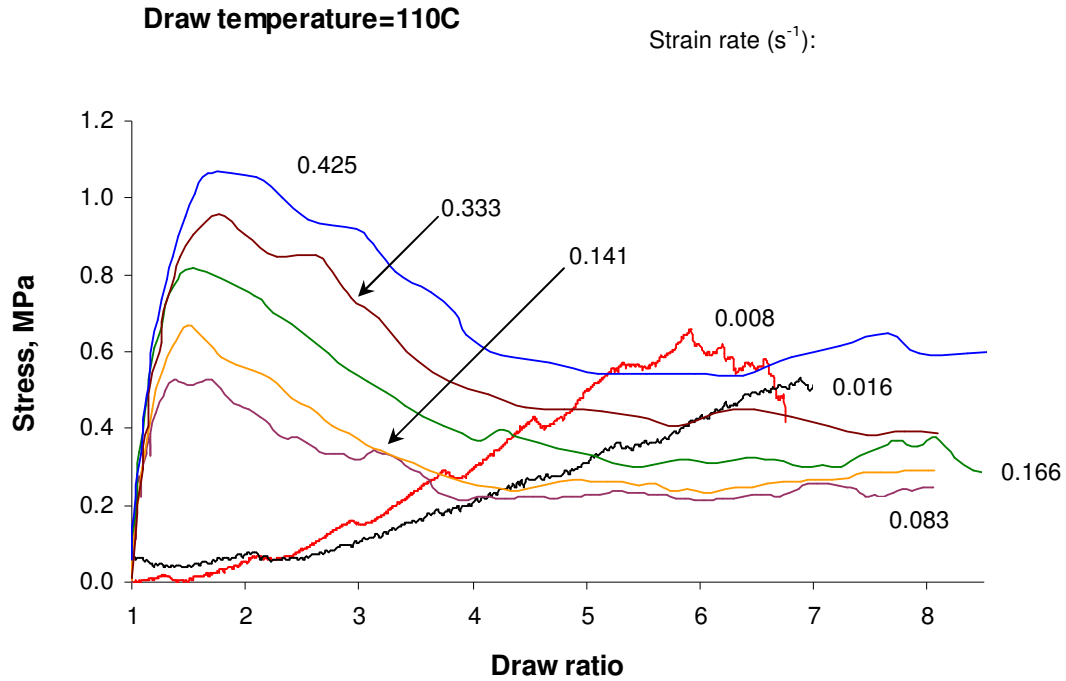


Figure 30. Stress-strain curves at 110°C at different strain rates

Based on these observations, we expected that with further increase in temperature and at the same strain rate, the drawing will result in low orientation and small crystallinity. But for samples drawn at 115°C the stress-strain curves obtained were counter-intuitive as shown in *Figure 31*. At this temperature both types of drawing behavior (superdrawing, non-superdrawing) are found depending on the strain rate.

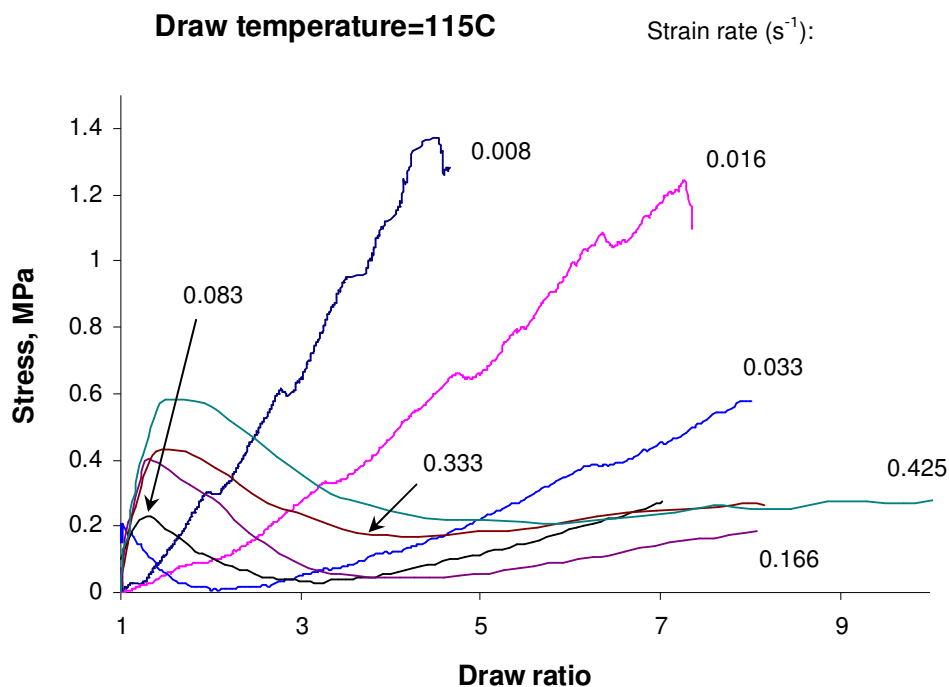


Figure 31. Stress-strain curves at 115°C. Different strain rates are indicated. Note that only the samples at 0.008 and 0.016 s^{-1} failed due to SIC

At 115°C the type-I behavior leading to high draw stress was found to be occurring at the lowest strain rates. This drawing behavior has not been reported in the literature for PET fibers. This observation suggests that there may be a complete “turnaround” in the mechanism of crystallization between the temperatures of 110°C and 115°C. To confirm the mechanism of drawing, similar tests of drawing were done at 120°C in the range of above strain rates.

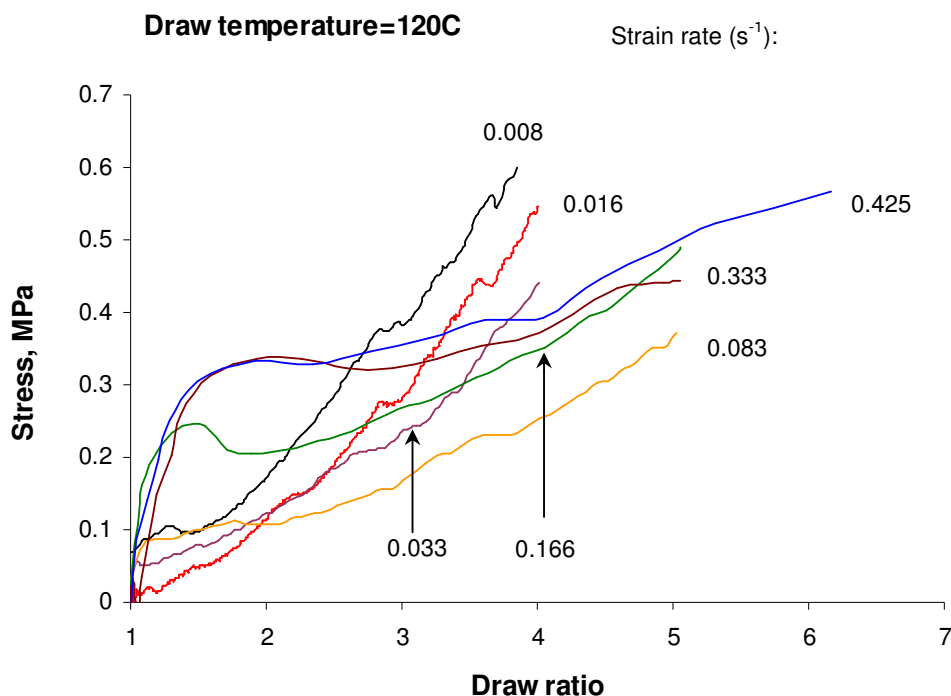


Figure 32. Stress-strain curves at 120°C at different strain rates

As seen in *Figure 32* the stress response of PET at 120°C was similar to that at 115°C. The only difference was that at 120°C, draw ratios over 6 were not possible at any strain rate. It is likely that the high temperature in combination with fluctuations inherent to the drawing process and thermal crystallization led to a sample failure before large draw ratios at 120°C. The strain rates up to 0.033 s^{-1} show no yielding and the initial linear response is difficult to differentiate from significant hardening; while for all the faster stretching rates initial elastic response is followed by yield which is followed by small to moderate amount of stiffening seen at different stages of drawing.

Because of the differences in mechanical behavior at 110 and 115°C as well as similarities in the same at 115 and 120°C, there is a reason to believe that a *crossover*

boundary exists at around 112-113°C and the *crossover* regime begins immediately above 110°C.

4.3 Study of crystallization behavior of drawn PET fibers using differential scanning calorimetry (DSC)

The uniaxial tensile tests were carried out to different draw ratios at five temperatures and different strain rates as described above. The drawn samples were quickly taken out of the chamber at the end of drawing and taken for thermal testing using the DSC. For the purpose of studying the changes in structure with drawing, the thermal transitions in non-isothermal DSC scans (cold crystallization and glass transition) of drawn samples were compared with that of undrawn (as-spun) fibers.

4.3.1 Methodology

A Seiko 220 differential scanning calorimeter was employed to perform thermal studies on the drawn samples. The procedure is as follows:

- Make a sample of fiber bundles cut into very small pieces (<1mm). Making a powdered sample helps to avoid fiber shrinkage during the test.
- Sample were of weight 5-15 mg. Run heating and cooling cycles at a rate of 10°C min⁻¹ between 25 to 280°C

4.3.2 Effect of draw conditions on the crystallization in drawn PET samples

For as-spun fibers, there is a distinct exothermic transition between 122°C and 155°C with a peak at 141°C. This transition has been attributed to the cold crystallization associated with ordering of the amorphous chain network to form crystallites due to available thermal energy. The cold crystallization exotherm is present only during the

first heating cycle and follows immediately after the glass transition endotherm as seen in *Figure 33*. In this study it was assumed that a drawn sample that has a similar cold crystallization peak as the as-spun fibers may have undergone superdrawing. Since the thermal behavior of drawn sample is similar to that of an undrawn one, the changes in structure during drawing due to thermal or strain-induced crystallization can be assumed to be insignificant.

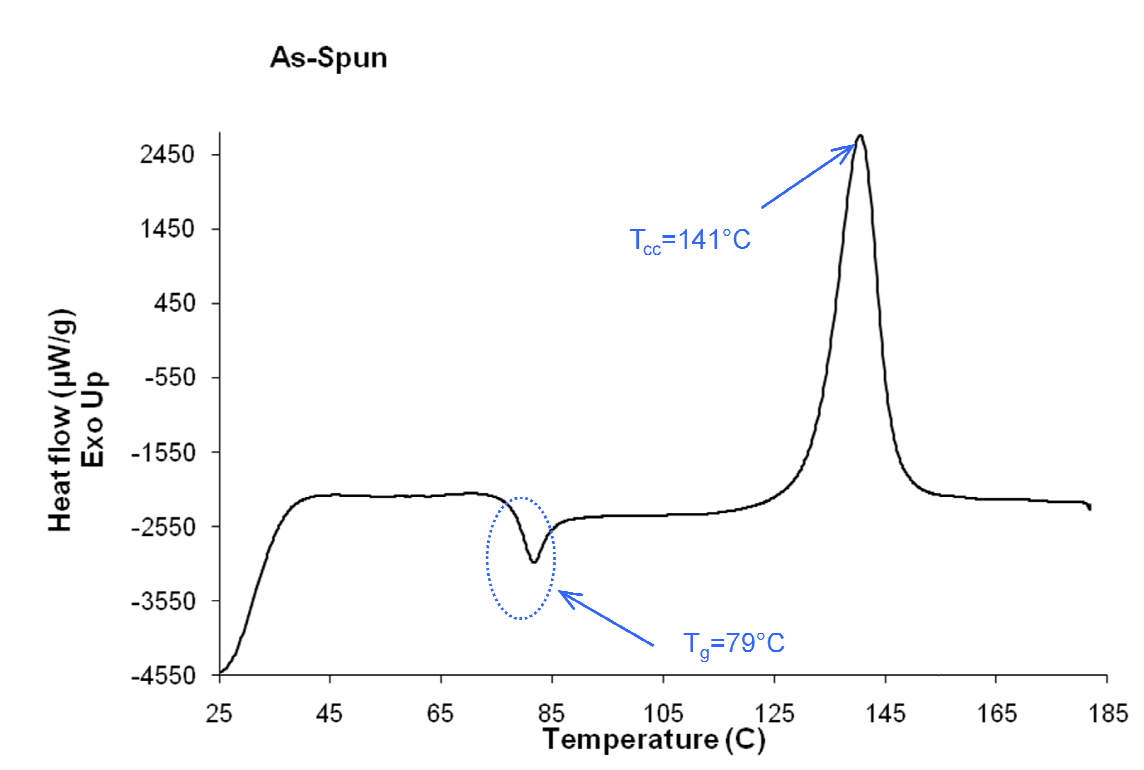


Figure 33. The primary thermal transitions during non-isothermal DSC scans ($10^\circ\text{C min}^{-1}$) of as-spun fibers

Figure 34 shows the DSC scans of samples drawn to draw ratio of 3 at 90°C . It was discussed earlier that these samples underwent type-I drawing process at all strain rates at

90°C and the associated SIC is reflected in the DSC curves. For all drawn samples the cold crystallization peak has been suppressed because of the crystallite formation undergone during the drawing process. The significant lowering of cold crystallization temperature, by as much as 36°C, indicates that drawing has caused significant orientation and accompanying strain-induced crystallization.

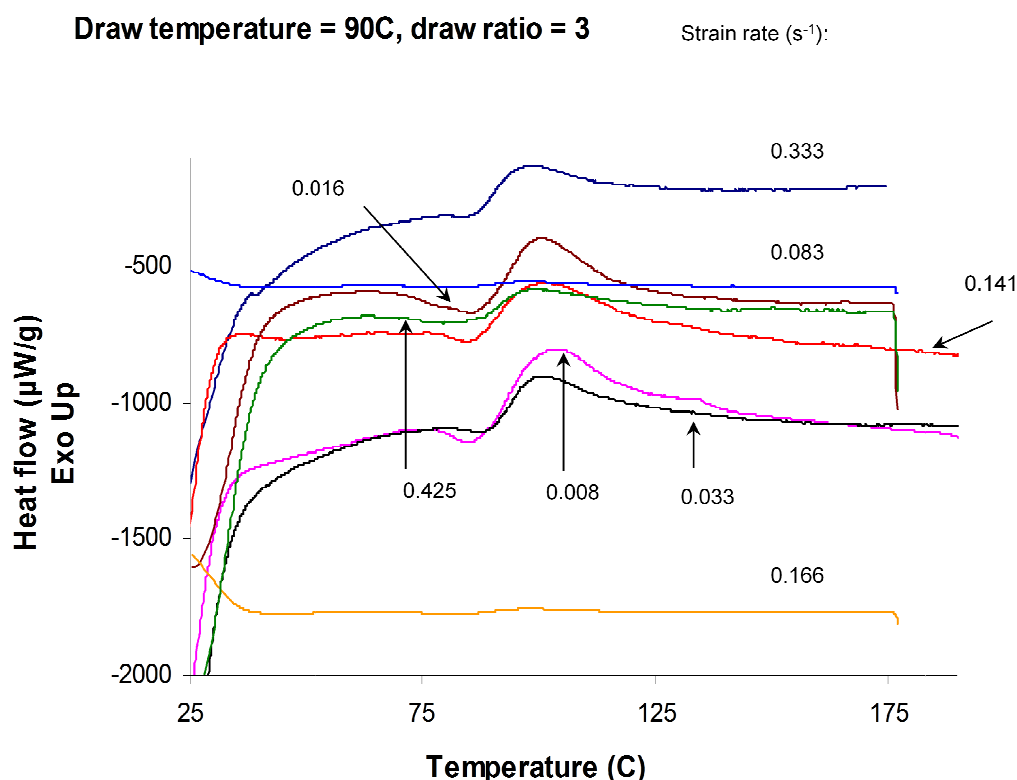


Figure 34. DSC scans (10°C min⁻¹) of samples drawn at 90°C at different strain rates

If the drawn sample is oriented and semi-crystalline, the cold crystallization peak does not appear at all, since it is associated with the reordering of amorphous chain segments above the glass transition. If the transition is visible as a feeble transition peak, as in *Figure 34* above, the temperature of onset of cold crystallization not only goes down but also tends to merge with the glass transition. The orientation of molecules caused by

drawing decreases conformational entropy of the molecules and, hence, favors the cold crystallization and hinders the occurrence of glass transition during the first heating cycle. Table 5 below summarizes the main transitions at 90°C.

Table 5. Thermal properties of the fibers drawn at 90°C to draw ratio of 3 at different strain rates

Strain rate ($\times 10^{-3} \text{ s}^{-1}$)	T_g (°C)	T_c Onset (°C)	T_c peak (°C)
8	82	88	103
33	--	90	101
141	83	86	101
333	--	87	98
As-spun fibers	79	122	141

--: peak not visible/insignificant

Figure 35 reveals the thermal behavior of samples drawn at 105°C. There is a very distinct shift in the onset and peak temperature of cold crystallization. With increasing strain rates the cold crystallization occurs closer to glass transition and finally becomes invisible at 0.333 s^{-1} . The thermal behavior in these curves shows two things: first the samples drawn at low strain rates are very close to as-spun behavior and thus superdrawn; and secondly as the strain rate increases they move farther away from their initial amorphous state. The latter is a manifestation of type-I drawing at 0.425 s^{-1} . Thus it can now be proposed that at 105°C PET undergoes superdrawing up to strain rates below 0.333 s^{-1} . Table 6 following the *Figure 35* summarizes the main transitions at 105°C.

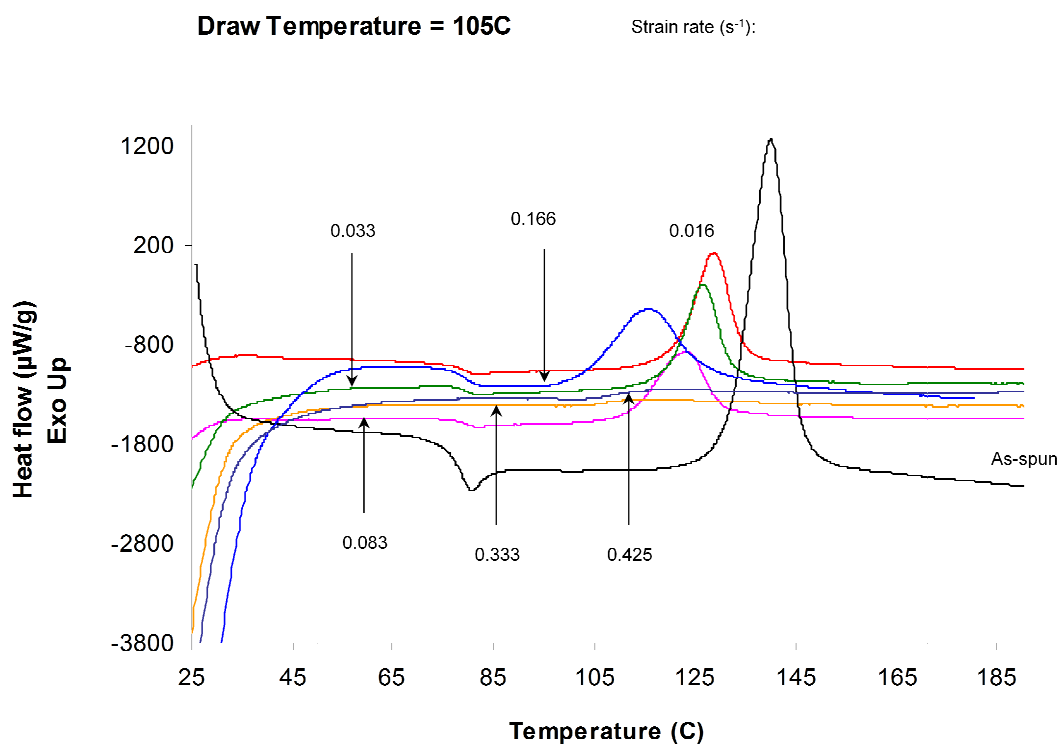


Figure 35. DSC scans (10°C min⁻¹) of samples drawn at 105°C to draw ratios greater than 10. Different strain rates are indicated

Table 6. Thermal properties of the fibers drawn at 105°C and different strain rates

Strain rate(x 10 ⁻³ s ⁻¹)	T _g (°C)	T _c Onset (°C)	T _c peak (°C)
16	79	113	130
33	79	110	126
83	79	107	123
333	--	--	--
425	--	--	--
As-spun fibers	79	122	141

--: peak not visible/insignificant

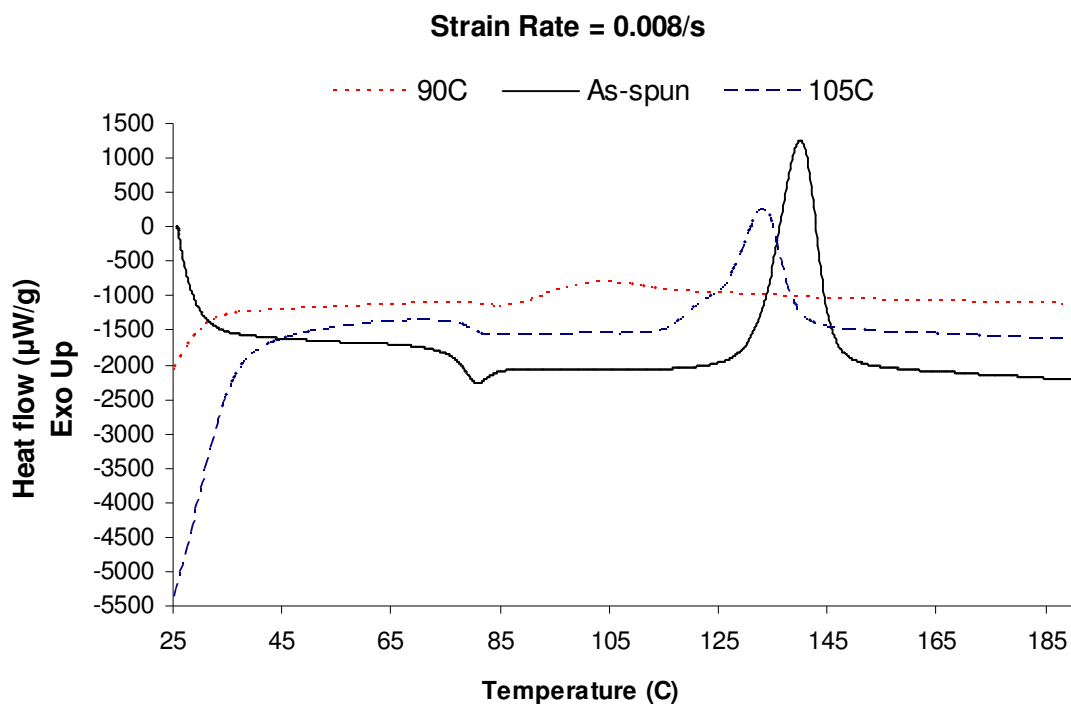


Figure 36. DSC scans ($10^{\circ}\text{C min}^{-1}$) of samples drawn to draw ratio of 3 at 0.008 s^{-1} and at 90 and 105°C as compared to undrawn (as-spun) fibers

Figure 36 closely compares the behavior during non-isothermal DSC studies of fibers drawn at 90°C and 105°C to same draw ratio of three and strain rate of 0.008 s^{-1} . The data in Table 7 lists their thermal properties, including crystallinity, below:

Table 7. Thermal properties of the fibers drawn to draw ratio of 3 at 0.008 s^{-1} and at 90 and 105°C as compared to as-spun fibers

Sample	T_g ($^{\circ}\text{C}$)	T_{c_onset} ($^{\circ}\text{C}$)	T_c ($^{\circ}\text{C}$)	ΔH_c (J/g)	X_c (%)	T_{m_onset} ($^{\circ}\text{C}$)	T_m ($^{\circ}\text{C}$)	ΔH_m (J/g)
As-spun fibers	79	122	141	26.64	6.28	240.1	255.9	35.43
105°C	81.1	114.4	134.1	26.90	7.31	240.0	254.8	37.13
90°C	80.7	88.5	103.5	22.92	11.60	240.1	254.5	39.16

The percent crystallinity (X_c) values were calculated using the following expression:

$$\%X_c = \left(\frac{\Delta H_m - \Delta H_c}{\Delta H_0} \right) \times 100 \quad (52)$$

where ΔH_c is the area under cold crystallization peak, ΔH_m is the area under melting peak and ΔH_0 is the enthalpy of fusion for a 100% crystalline PET (≈ 140 J/g). It is clearly demonstrated that the sample drawn at 105°C is essentially non-crystalline and therefore superdrawn at small strain rate.

The next step is to investigate if there is any rate at which flow draw can take place at higher temperatures. To answer the above question the crystallization behavior of samples drawn at temperatures 110°C, 115°C and 120°C and at similar strain rates was studied in the DSC. *Figure 37* shows the non-isothermal scans of fibers drawn at 110°C to draw ratio of eight at different strain rates. It is evident that for drawing at temperature of 110°C the cold crystallization behavior is quite close to the undrawn fibers at all stretching rates. Although the distinction between different rates is not sharp enough to yield a clear evidence of any difference between them, it can be said that drawing at 0.425 s^{-1} led to crystalline samples.

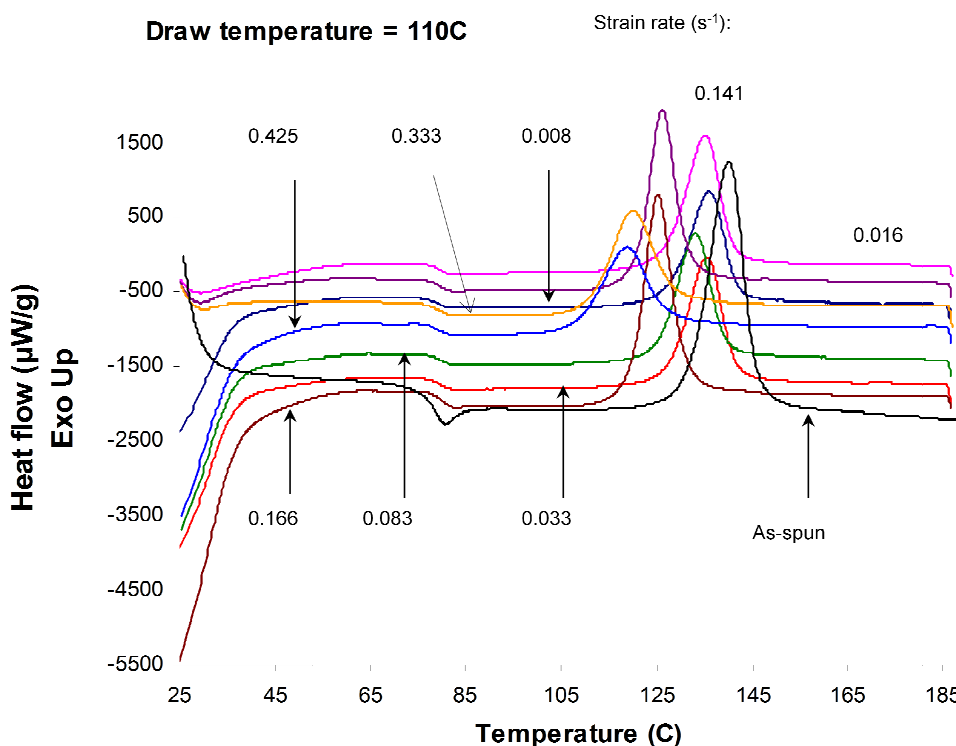


Figure 37. DSC scans ($10^{\circ}\text{C min}^{-1}$) of samples drawn to draw ratio of 8 at 110°C . Different strain rates are indicated

The thermal properties of drawn samples at 115°C have been shown in *Figure 38* along with the as-spun fibers for comparison. Table 8 lists the main transitions of cold crystallization behavior of drawn samples at different rates of stretching. Interestingly, the slowest rates (0.008 s^{-1} and 0.016 s^{-1}) appear as weak and suppressed transitions, while all higher rates are closer to the as-spun fibers.

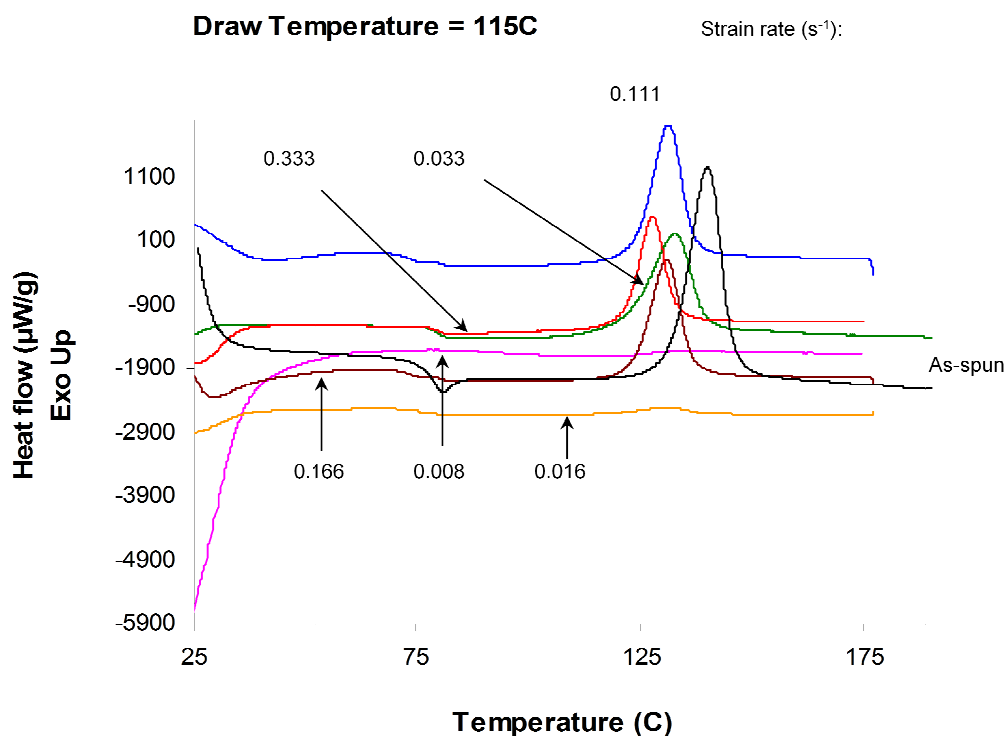


Figure 38. DSC scans (10°C min⁻¹) of samples drawn to draw ratio of 8 at 115°C. Different strain rates are indicated

Table 8. Thermal properties of the fibers drawn at 115°C to draw ratio of 8 and different strain rates

Strain rate(x 10 ⁻³ s ⁻¹)	T _g (°C)	T _c Onset (°C)	T _c peak (°C)
8	--	--	--
16	--	--	--
33	80	110	134
333	80	113	128
As-spun fibers	79	122	141

--: peak not visible/insignificant

This data of the cold crystallization behavior suggests that, if drawing occurs at 115°C, the samples drawn at rates higher than 16×10⁻³ s⁻¹ increasingly become less crystalline. Therefore, contrary to the behavior at 105°C, these samples exhibit a SIC dominated or

type-I behavior at the slowest rate ($8 \times 10^{-3} \text{ s}^{-1}$). However the faster rates lead to samples with smaller crystallinity, i.e., superdrawn samples.

Finally, to confirm the anomalous behavior at 115°C , tests were done on samples drawn at 120°C to same draw ratio of eight. The thermal behavior of samples drawn at 120°C at different rates of stretching, in comparison with undrawn fibers, can be seen in *Figure 39*.

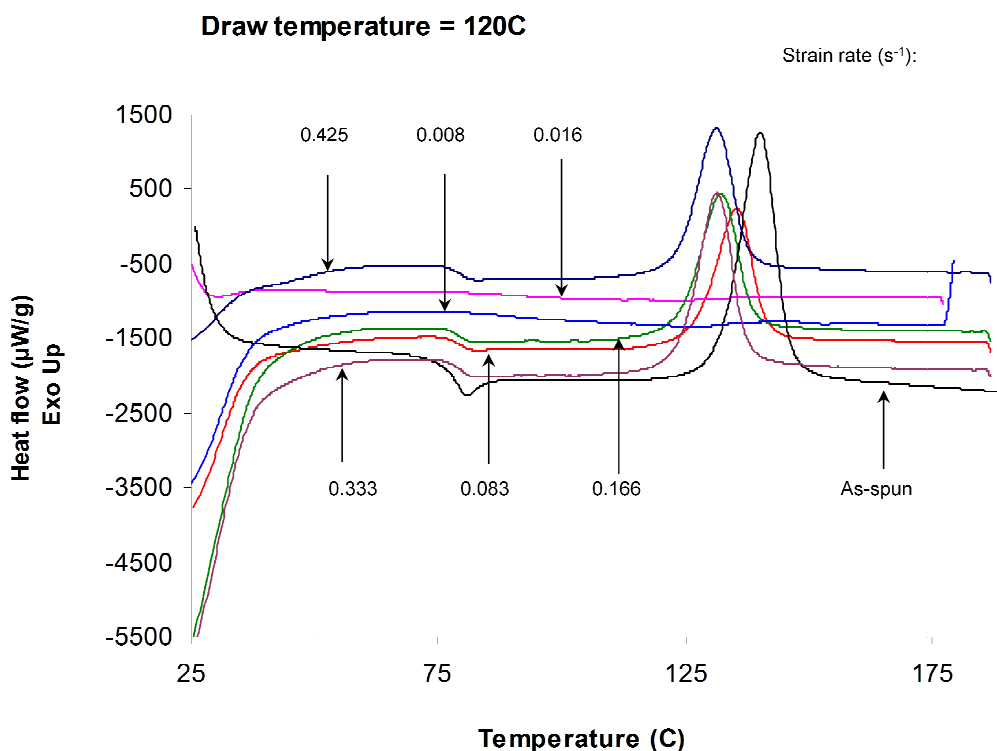


Figure 39. DSC scans ($10^\circ\text{C min}^{-1}$) of samples drawn to draw ratio of 8 at 120°C . Different strain rates are indicated

This behavior is similar to that at 115°C , i.e., all the stretching rates exhibit prominent transitions close to as-spun fibers; except at 0.008 s^{-1} and 0.016 s^{-1} for which the glass transition and cold crystallization are insignificant.

From these results it is apparent that if drawing takes place at a temperature between 112°C and 120°C, *faster* stretching rates will lead to non-crystalline drawn samples. This behavior represents a transition because for temperatures between 105°C and 110°C drawing without significant crystallization occurs at *slower* strain rates.

Earlier experimental studies [8] about crystallinity development in PET have shown that higher temperatures will reduce the critical orientation needed for onset of crystallization. According to Salem [31] this is because higher temperature not only gives rise to rapid rates of molecular relaxation but also favors crystallization. Because of these two opposing phenomena acting at the same time, the overall effect of increasing temperature on crystallinity depends on which one dominates-relaxation or crystallization. LeBourvellec et al. found in their study (temperatures between 80 and 103°C at strain rates of 0.008, 0.028 and 0.115 s⁻¹) that for a given draw ratio and temperature the crystallinity level increases with strain rate [8]. This behavior is confirmed by our data for the above range of parameters. We discovered, however, that a transition occurs at about 113°C which leads to the decrease in crystallinity with strain rate for drawing temperatures of 115°C and 120°C.

Similarly in the Salem study (strain rates between 0.01-2.1 s⁻¹ at temperatures of 83, 90 and 96°C) it was shown that up to strain rates of about 1 s⁻¹ the relaxation effect dominates and the crystallinity is higher at lower temperature for a given draw ratio and strain rate [15]. But at higher strain rates ($\sim 10^0$ s⁻¹) samples drawn at higher temperature will be more crystalline for a given draw ratio and strain rate because the effect of

crystallization dominates. We found, however, that for drawing temperatures between 110°C and 120°C the crystallization phenomenon dominates even at strain rates less than 1 s⁻¹. For strain rates up to 0.166 s⁻¹ the crystallinity decreases up to the transition point 113°C and then increases with temperature. On the other hand, for strain rates higher than 0.166 s⁻¹, our data agrees with the prevalent relaxation phenomenon as seen by Salem [15].

This interesting finding means there remains more investigation to confirm the effect of temperature on crystallization in different strain rate regimes. The orientation analysis, as described in *Section 4.4*, was carried out for this purpose. Before that it is useful to understand the kinetics of isothermal crystallization of PET fibers at different draw temperatures involved in this study, as explained in next section.

4.3.3 Effect of crystallization rate on crystallinity development

To better understand the crystallization of drawn samples in different strain rate regimes and at temperatures of 105-120°C the crystallization kinetics of PET was studied. It was assumed that the total amount of crystallinity developed in a sample during drawing depends largely upon the amount of time-of-drawing relative to the half-time of crystallization ($t_{1/2}$) for the given drawing condition. The isothermal crystallization parameters of amorphous PET were determined at temperatures of 105°C, 110°C, 115°C and 120°C. The temperature of 90°C was omitted since it is known that superdrawing is not possible at this temperature however slow the stretching rate.

4.3.3.1 Isothermal crystallization parameters of amorphous PET - Avrami kinetic analysis

The crystallization half-time ($t_{1/2}$) was determined based on the Avrami equation:

$$\log[-\ln(1-X(t))] = \log K + n \log t \quad (53)$$

where n is the Avrami exponent, K is the crystallization rate constant, t is the time of crystallization and $X(t)$ is fractional crystallinity. The Avrami plot, $\log[-\ln(1-X(t))]$ versus $\log(t)$, yields a straight line from which the parameters n and K can be calculated. *Figures 40 to 43* show the Avrami plots for 105°C, 110°C, 115°C and 120°C, respectively.

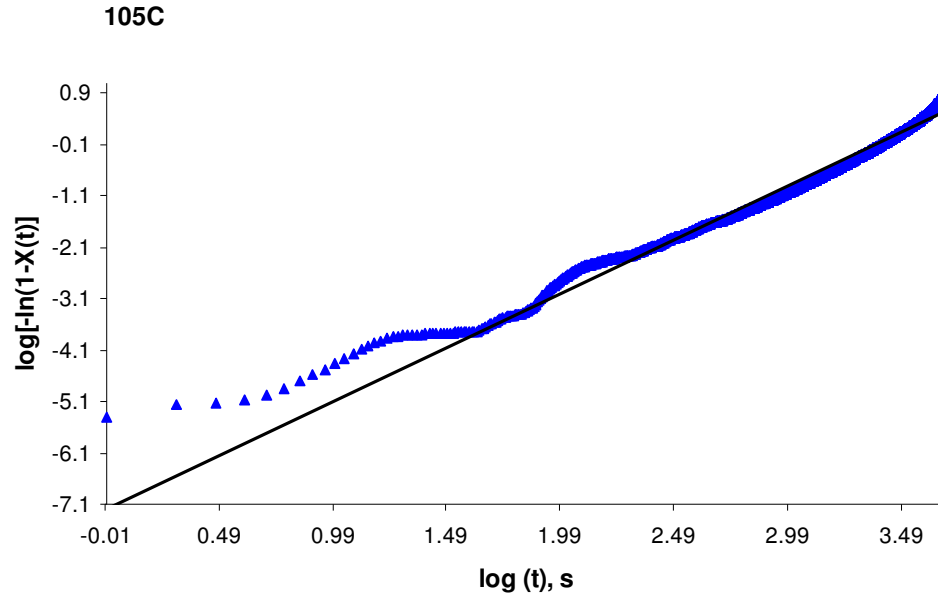


Figure 40. The Avrami plot for isothermal crystallization of amorphous PET at 105°C

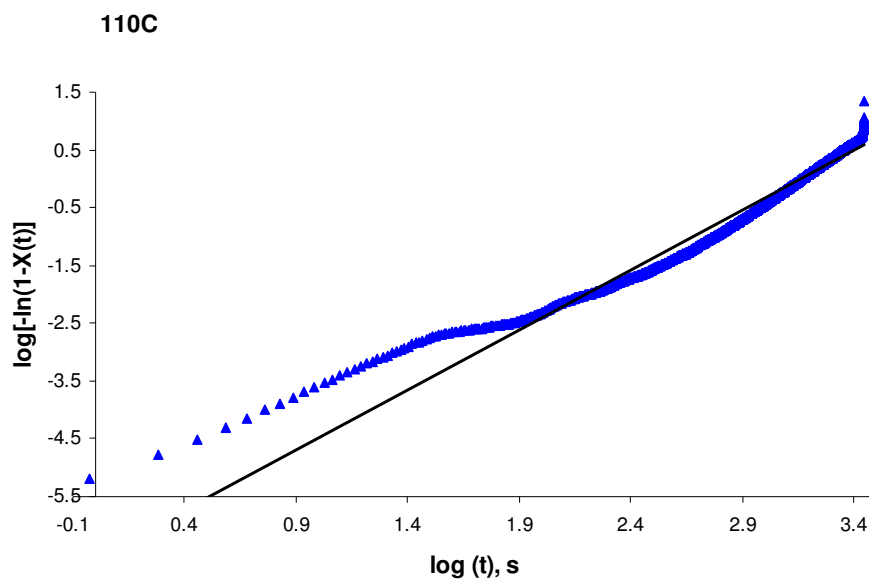


Figure 41. The Avrami plot for isothermal crystallization of amorphous PET at 110°C

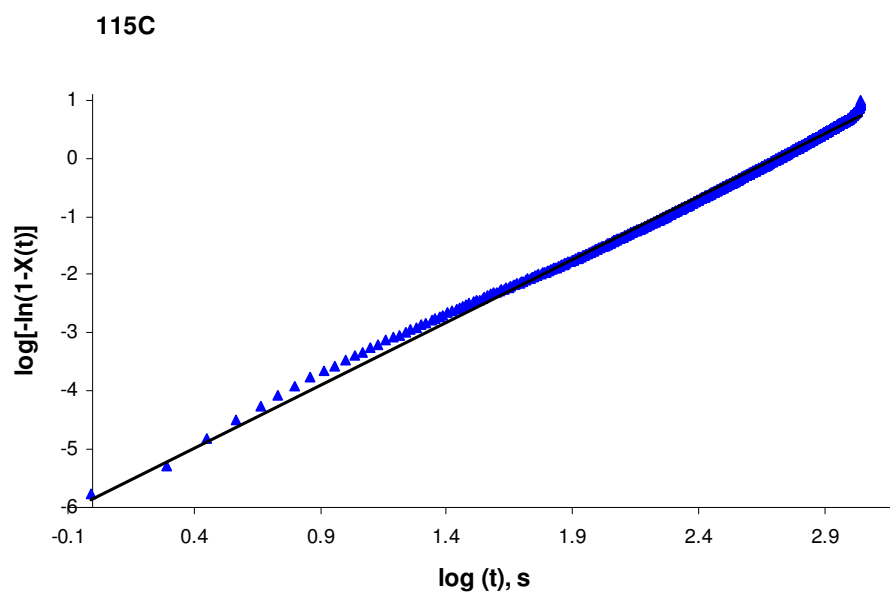


Figure 42. The Avrami plot for isothermal crystallization of amorphous PET at 115°C

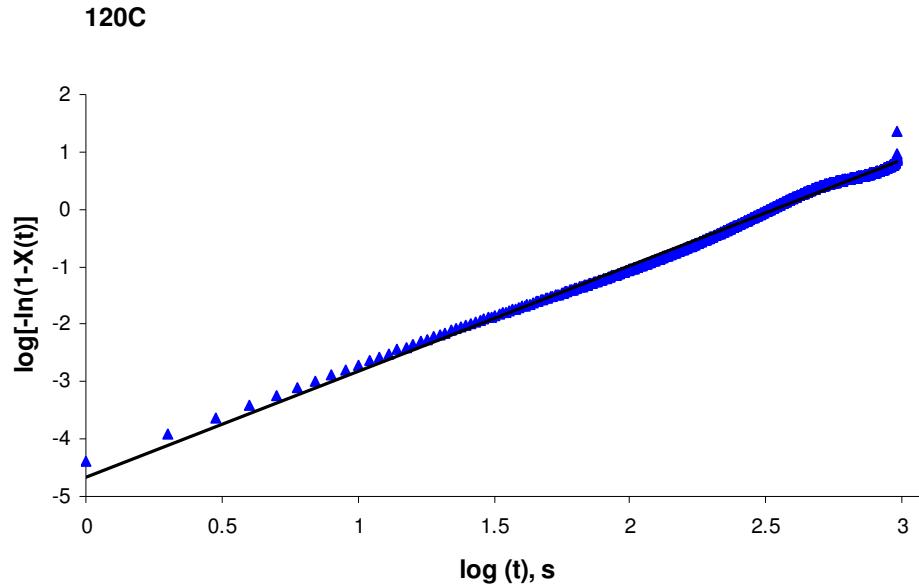


Figure 43. The Avrami plot for isothermal crystallization of amorphous PET at 120°C

The development of fraction crystallinity $X(t)$ as a function of crystallization time t at each of the four temperatures is plotted in *Figure 44*. The estimated values of n , K , the corresponding half crystallization time ($t_{1/2}$) are listed in Table 9. They were determined from the use of equation (53). It should be noted that as the temperature of crystallization increases, the value of $t_{1/2}$ decreases quite rapidly. This could explain the transition or cross-over effect in crystallization behavior during drawing at around 113°C. The rate constant K and overall crystallization rate G (the reciprocal of $t_{1/2}$) increase with the crystallization temperature due to the fact that the higher the temperature, the larger the molecular mobility, which facilitates the ordering of crystalline regions.

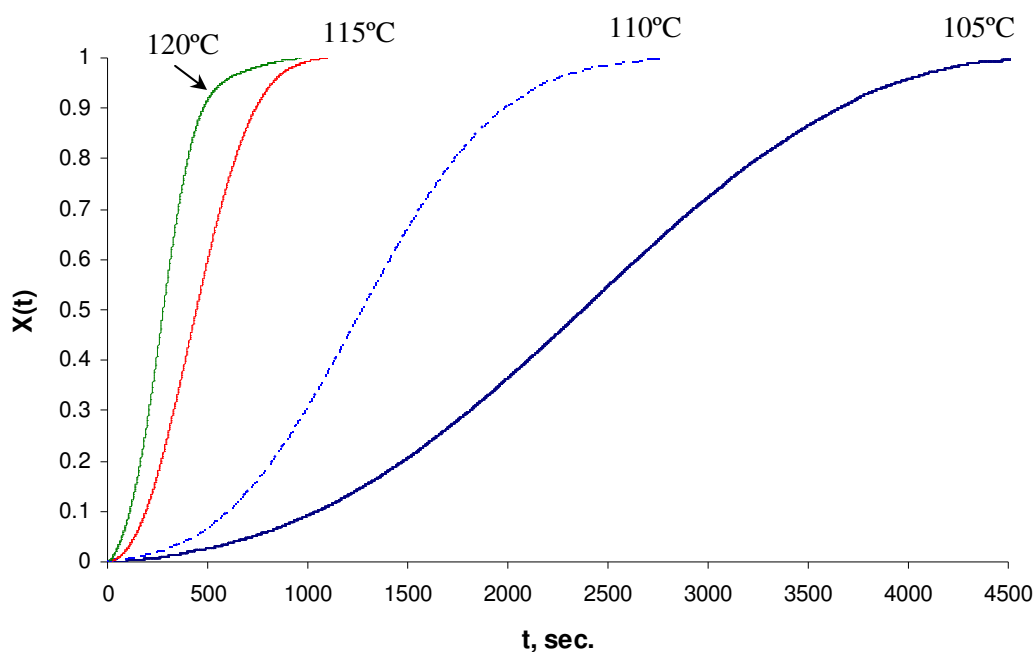


Figure 44. The development of fractional crystallinity during isothermal crystallization of amorphous PET at different temperatures

Table 9. Isothermal crystallization parameters for amorphous PET

$T_c(^{\circ}\text{C})$	n	$K \times 10^{-5} (\text{s}^{-1})$	$t_{1/2} (\text{s})$
105	2.103	0.006	2374
110	2.074	0.028	1281
115	2.165	0.141	469
120	1.842	2.214	279

The Avrami exponent n is a good indicator of the nature of nucleation and the growth mechanism. The n value is close to 2, hinting that the primary crystallization of the as-spun PET sample followed the mechanism of a disc-like growth from instantaneous nuclei [93]. In the previous study of unoriented amorphous PET by Mayhan et al. [92], their experiments covered a temperature range from 96.5 to 132°C. The values of $t_{1/2}$ at

temperatures of 110 and 120°C were reported to be 870 and 210 seconds respectively. The values of $t_{1/2}$ in our measurements are higher than those reported in Mayhan et al. but they follow a similar trend.

4.3.3.2 *Comparison of drawing time with crystallization rate and its effect on crystallinity development*

Figure 45 shows a plot between time spent by sample during drawing to a given draw ratio (3, 5 and 10) and strain rate for any drawing temperature. The cross-marks and the dotted lines on this plot represent a threshold time below which a sample is expected to have developed negligible crystallinity during drawing. If the draw time is greater than the half crystallization times ($t_{1/2}$) as shown in Table 9, then the drawing process at a given temperature and strain rate itself would entail significant isothermal crystallization. For example the samples drawn at 115°C and 120°C have undergone isothermal crystallization when drawn to ratio 5 or greater at 0.008 s⁻¹ or to a draw ratio more than 10 at strain rates of 0.016 s⁻¹ and 0.033 s⁻¹. By similar reasoning, on the other hand, the samples drawn at 105°C and 110°C spent a short amount of time in drawing relative to the large $t_{1/2}$ values at those temperatures and therefore any of those samples could not have undergone significant isothermal crystallization at any strain rate. Thus according to *Figure 20* the superdrawn samples should be obtained at slow strain rates below 110°C and at high strain rates for temperatures above 110°C.

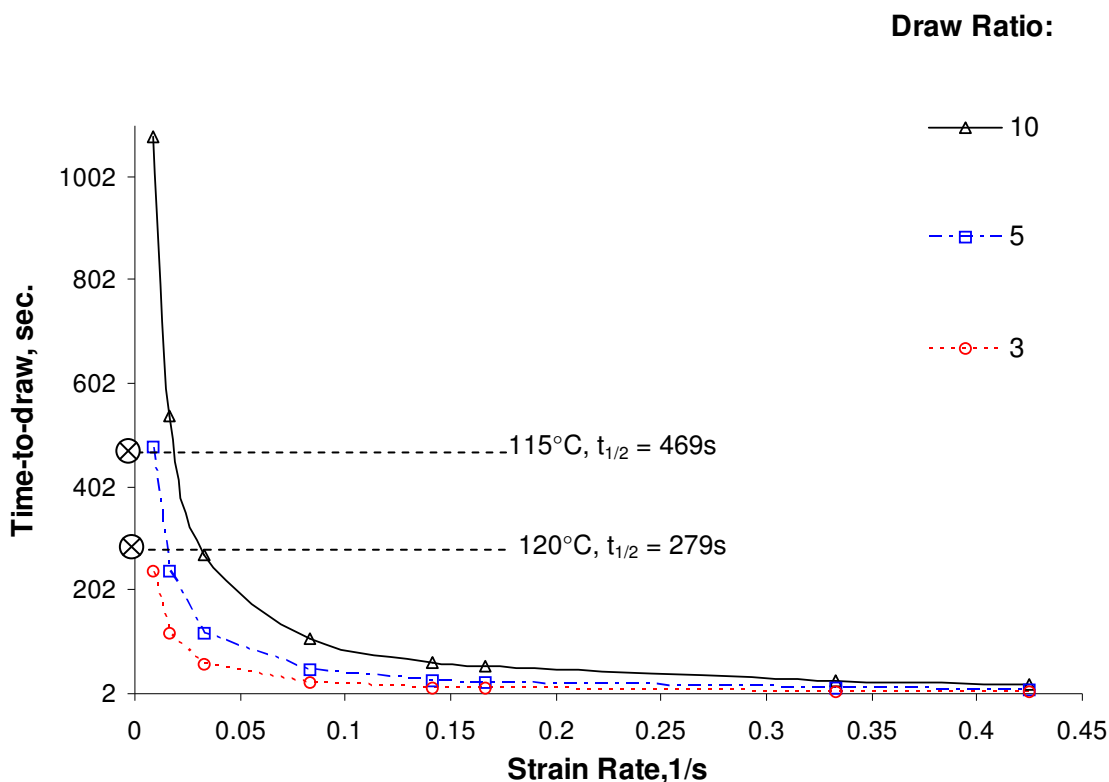


Figure 45. A graph between drawing time and strain rate at three draw ratios. The dotted straight lines mark the threshold time, shown for two draw temperatures, above which a sample undergoes thermal crystallization during drawing

4.4 Analysis of the development of orientation in drawn PET fibers using polarized microscopy

The stress-strain behavior and the thermal test analysis indicated that there is a transition in terms of overall crystallinity development for amorphous PET fibers. That transition means that the non-crystalline samples are obtained at slow stretching rate for temperatures of 105 and 110°C, but a faster strain rate is needed to get superdrawn samples at the draw temperatures of 115 and 120°C. Whether this is true can be judged

on the basis of overall orientation of those drawn fibers. This will also lead to a better picture of the morphology of PET fibers in range of our experimental conditions.

4.4.1 Methodology

Birefringence measurements were carried out on all the drawn samples using a *de-Senarmont* compensator on a Polarizing microscope. A green filter was used to obtain monochromatic light ($\lambda=551$ nm) beam. The use of the *de-Senarmont* compensator assisted in capturing the very small orders of retardation from the samples. The total birefringence is obtained from the measured retardation r (nm) and the thickness h (μm) of the sample. The thickness or the diameter of the fibers was measured after taking an image of the sample and then using the image analysis software *Image Pro-plus*.

$$r = \frac{\theta \times \lambda}{180} \quad (54)$$

where θ is the angle of extinction shown by the sample placed at 45° position between crossed polarizers.

$$\text{Birefringence} = \frac{r}{1000h} \quad (55)$$

The process was repeated, and the average of five readings was determined and reported here.

4.4.2 Effect of draw conditions on the orientation in drawn PET samples

The birefringence is a good measure of the overall orientation of fibers. It varies from 0 for a completely unoriented specimen to 1 for a highly oriented system. The undrawn fibers have a birefringence of 0.0025 which indicates they are essentially unoriented. The

drawn fibers are expected to have a higher orientation and therefore a higher value of birefringence. Orientation was studied as a function of draw temperature and strain rate for a given draw ratio. The birefringence measurements were made on samples drawn at three representative strain rates – 0.008, 0.166 and 0.425 s^{-1} . Also, in some cases, the values of birefringence were measured at various draw ratios for a given set of drawing conditions; in order to study if there is any effect of strain on structure development during drawing.

4.4.2.1 Birefringence as a function of draw temperature

The evolution of birefringence in samples drawn to draw ratio of five in different strain rate regimes with increasing temperature is shown in *Figure 46*. This graph shows that the orientation varies in opposing manner with temperature for strain rates of 0.008 s^{-1} and 0.425 s^{-1} .

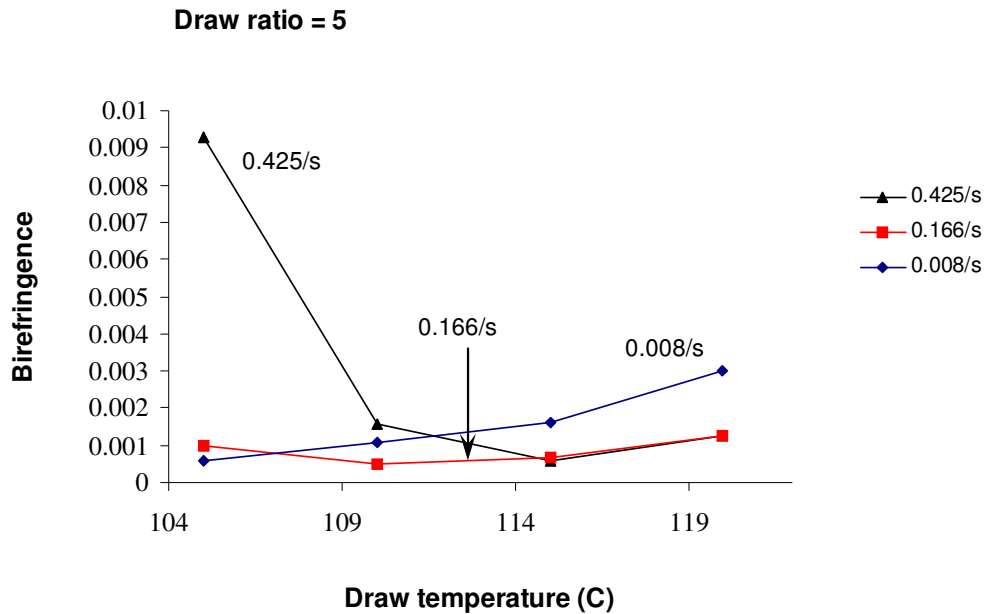


Figure 46. Birefringence for samples drawn to draw ratio of 5 versus draw temperature at three strain rates

The birefringence variation at 0.166 s^{-1} falls in between which is an indication of a transition at this rate and that there are two different regimes of orientation development on either sides of this rate. This plot suggests that the transition occurs at a draw temperature of $112\text{--}113^\circ\text{C}$. The birefringence is higher at a *slower* strain rate after this transition temperature is exceeded. *Figure 47* shows the variation of birefringence in samples drawn to draw ratio of ten at five different strain rates with increasing temperature. The results are qualitatively the same. This graph confirms the transition and indicates a transition temperature of about 113°C .

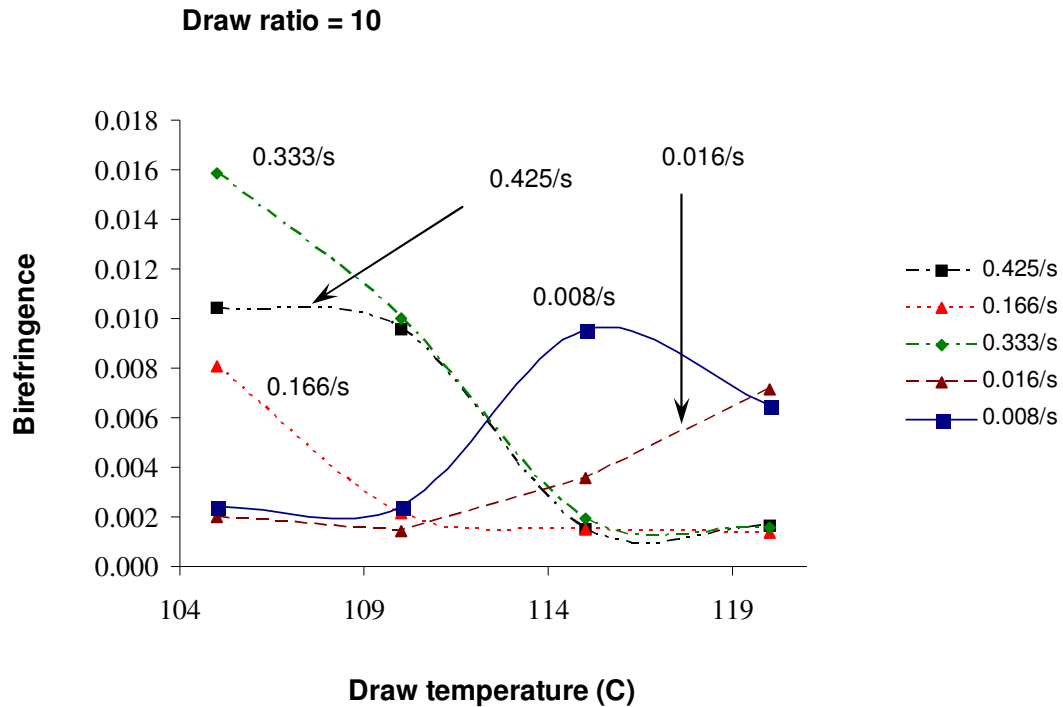


Figure 47. Birefringence for samples drawn to draw ratio of 10 versus draw temperature at five strain rates

4.4.2.2 Birefringence as a function of strain rate

If we see the evolution of birefringence with strain rate at different draw temperatures (see *Figure 48*) it becomes clear that distinct temperature regimes also exist for orientation and crystallinity development. The birefringence increases with strain rate for draw temperature up to 110°C, and the trend is clearly reversed at 115°C and 120°C.

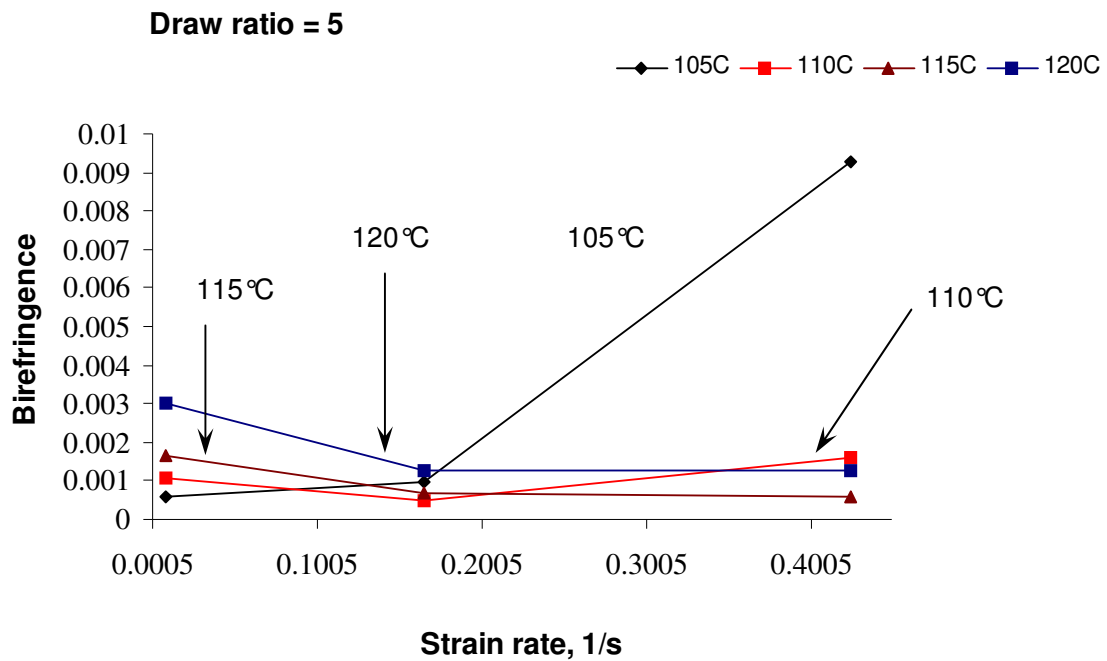


Figure 48. Birefringence for samples drawn to draw ratio of 5 versus strain rate at four draw temperatures

Similar trends are visible in *Figure 49* which is the same as *Figure 48* but with samples drawn to a draw ratio of ten. From these plots we can deduce that the crossover occurs at a strain rate of about 0.17/s.

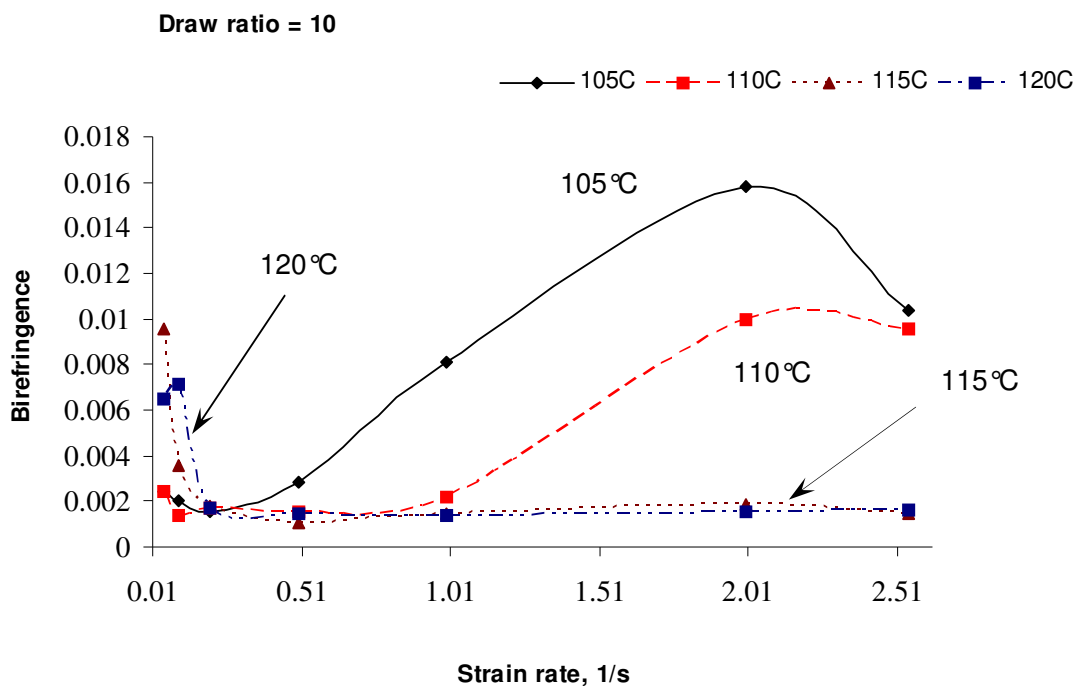


Figure 49. Birefringence for samples drawn to draw ratio of 10 versus strain rate at four draw temperatures

4.4.2.3 Birefringence as a function of draw ratio

The birefringence increases with increasing draw ratio at any given draw temperature and strain rate. This is explained on the basis of increasing amount of orientation imparted by stretching the network. *Figures 50-53* show the birefringence as a function of draw ratio at all three representative strain rates for four draw temperatures. These graphs clearly show the transition in crystallization mechanism with increasing temperature that has been discussed in *Section 4.4.2.2*.

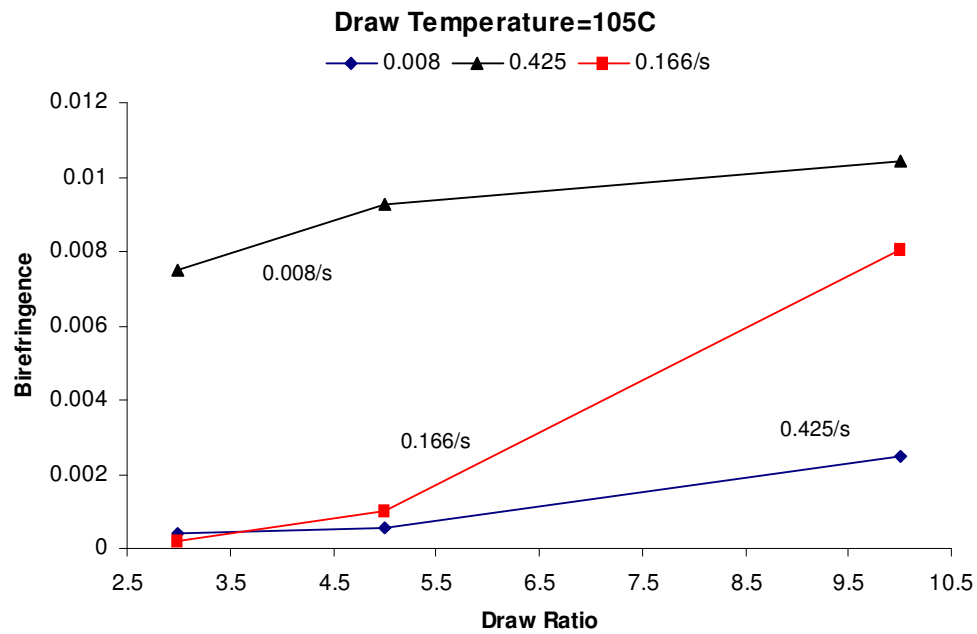


Figure 50. Birefringence versus draw ratio for three selected strain rates at draw temperature of 105°C

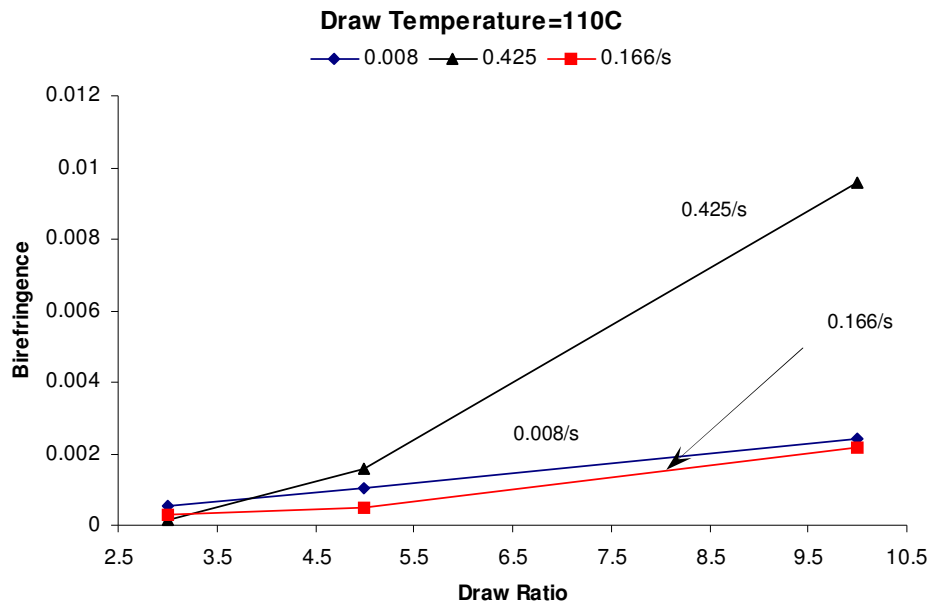


Figure 51. Birefringence versus draw ratio for three selected strain rates at draw temperature of 110°C

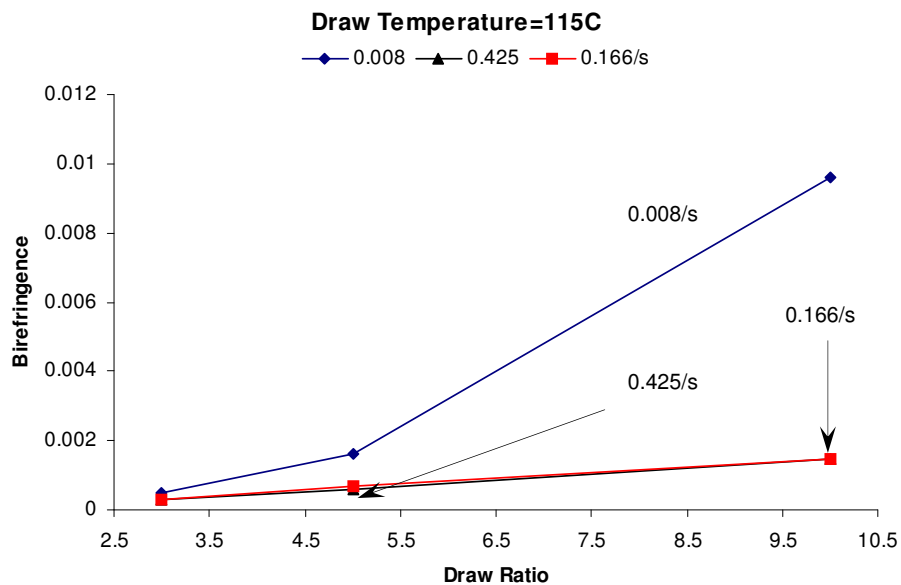


Figure 52. Birefringence versus draw ratio for three selected strain rates at draw temperature of 115°C

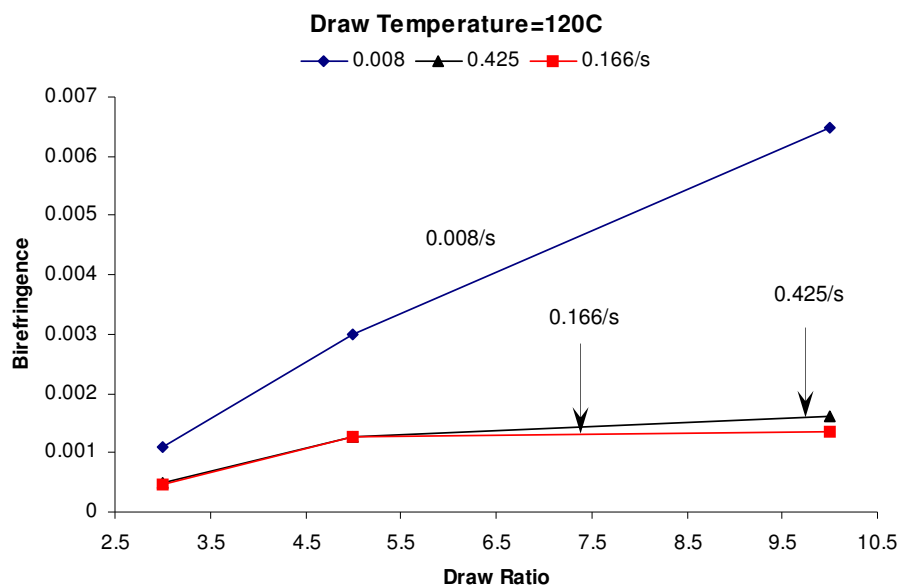


Figure 53. Birefringence versus draw ratio for three selected strain rates at draw temperature of 120°C

It is evident that for a given draw ratio the orientation increases with increasing strain rate at 105°C (*Figure 50*). But as temperature increases to 110°C a crossover begins to be visible (*Figure 51*). Thus for the draw temperatures of 115°C and 120°C, the transition has occurred and birefringence is *more* at the slowest stretching rate (*Figures 52 and 53*).

4.5 Analysis of mechanical, thermal and orientation behavior at representative strain rates

Experimental studies were conducted at eight different strain rates ranging from slowest (0.008 s^{-1}) to fastest (0.425 s^{-1}). In this section the critical three strain rates as mentioned before – 0.008 , 0.166 and 0.425 s^{-1} – have been highlighted as representative rates for making sense of the data. The stress-strain curves at these strain rates are shown in *Figure 54* for all the draw temperatures. We omitted the 90°C curves in these plots for reasons of clarity. At the drawing temperatures of 105 and 110°C, the stress-strain curves for 0.008 s^{-1} exhibit a relatively low draw stress and very large elongation to failure as seen in *Figure 54(a)*. Interestingly this superdrawing behavior is observed at temperatures of 115 and 120°C for the *fastest* strain rate of 0.425 s^{-1} as shown in *Figure 54(c)*. It is evident from the graphs that the deformation behavior of PET involves a peculiar characteristic: at 0.008 s^{-1} the draw stress *increases* with increasing temperature in excess of 110°C.

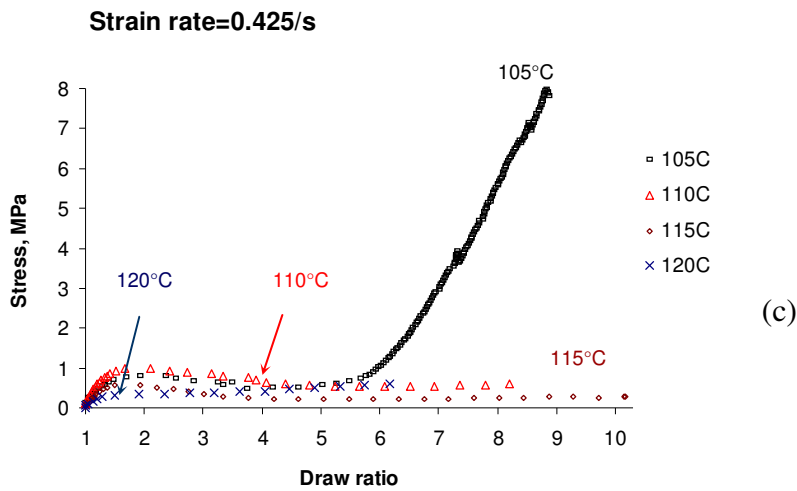
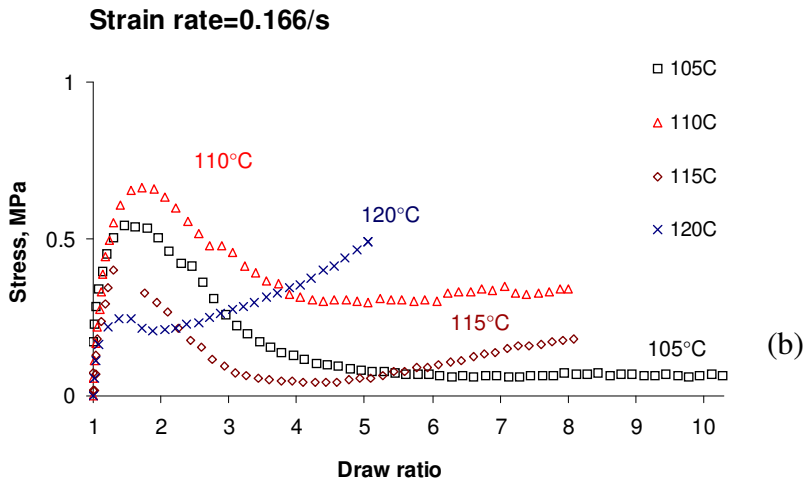
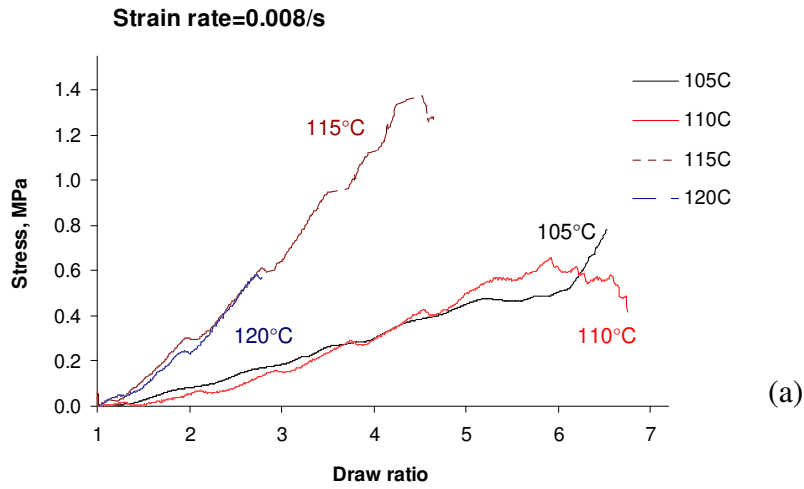


Figure 54. Stress-strain curves for four draw temperatures at representative strain rates:
(a) 0.008 s^{-1} , (b) 0.166 s^{-1} and (c) 0.425 s^{-1}

For stretching at 0.166 s^{-1} , in *Figure 54(b)*, there is no clear distinction between stress-strain behaviors at the four draw temperatures. Therefore we could assume this rate as the one at which a ‘transition’ might be taking place in terms of orientation and crystallinity development. This ‘transition’ was corroborated by the DSC study.

Then the thermal transitions for all the draw temperatures at the representative strain rates were analyzed as shown in *Figures 55(a), (b) and (c)*. It is evident from these DSC curves that non-crystalline samples were obtained if drawn at *slow* rate ($0.008/\text{s}$) for draw temperatures below 110°C . After this temperature is crossed, however, the transition occurs and a *fast* strain rate ($0.425/\text{s}$) is needed to achieve flow drawing. Thus our predictions from *Figure 44* (see *Section 4.3.3.2*) from the draw-time versus half crystallization time approach are consistent with the results of thermal analysis. In *Figure 55(b)* the thermal behavior at strain rate of 0.166 s^{-1} does not fall into the trend of decreasing crystallization onset temperature with higher strain rate. The thermal properties of samples drawn to draw ratio of eight at 105, 110, 115 and 120°C are listed in Table 10. It is clear from Table 10 and *Figure 55* that there is a hint of ‘crossover’ in crystallization behavior at 113°C or a strain rate of 0.166 s^{-1} .

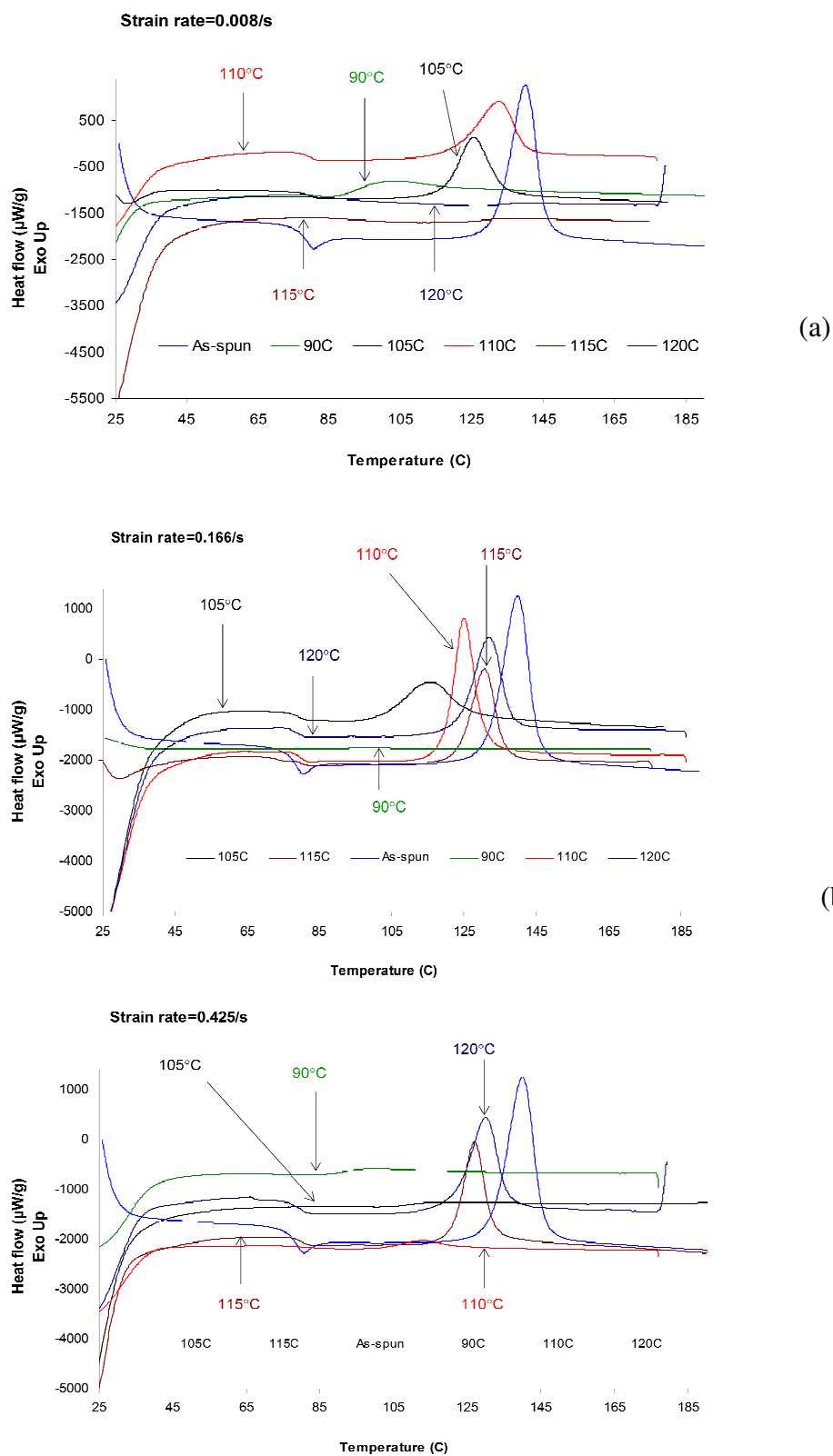


Figure 55. DSC scans at $10^\circ\text{C}/\text{min}$ of PET drawn at different temperatures and at rates of (a) $0.008/\text{s}$, (b) $0.166/\text{s}$ and (c) $0.425/\text{s}$; compared with as-spun fibers

Table 10. Thermal properties of the fibers drawn at representative strain rates and different temperatures

↓ Draw temperature (°C) Strain rate (s ⁻¹) →	T _g (°C)			T _c Onset (°C)			T _c peak (°C)		
	0.008	0.166	0.425	0.008	0.166	0.425	0.008	0.166	0.425
105	80	80	80	111	99	--	126	117	--
110	81	81	80	110	110	102	133	122	113
115				--	114	115	--	131	128
120	--	80	80	--	112	110	--	132	131
As-spun fibers	79			122			141		

This observation now confirms what was seen from the mechanical behavior: a ‘transition’ in crystallization kinetics might be taking place at 0.166 s⁻¹. This transition was studied further and validated with the orientation measurements.

To highlight this transition, the birefringence of drawn samples is plotted as a function of draw temperature for the slowest and fastest strain rates of this study in *Figure 56*. This graph clearly depicts that birefringence increases with draw temperature for a given draw ratio at the smallest strain rate of 0.008 s⁻¹. But since a transition has happened at the highest strain rate of 0.425 s⁻¹, it leads to highest orientation at lowest temperature.

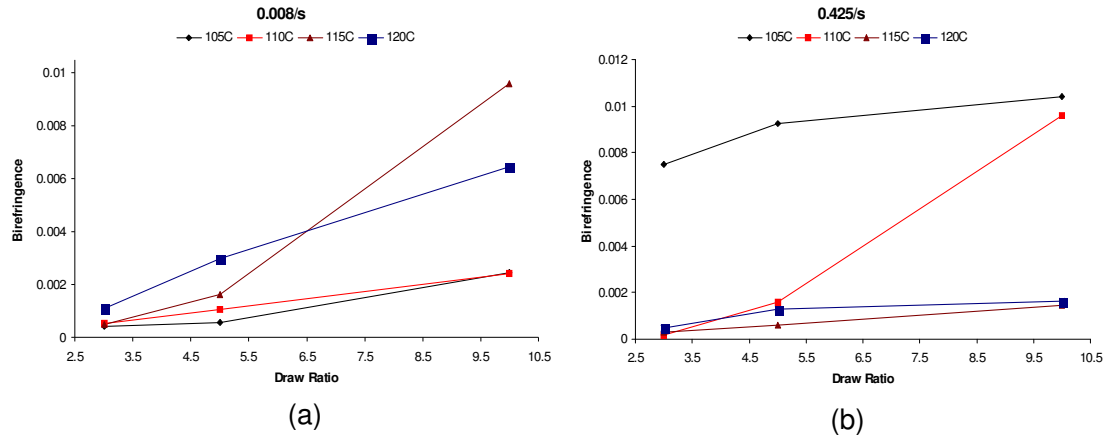


Figure 56. Birefringence versus draw ratio for four different draw temperatures at the strain rates of (a) 0.008/s and (b) 0.425/s

4.6 Summary

The boundary of superdrawing as illustrated in Table 11 was determined based on the above findings.

Table 11. Parameter window for Superdrawing

Strain rate ($\times 10^{-3} \text{ s}^{-1}$)	Draw Temperature ($^{\circ}\text{C}$)				
	90	105	110	115	120
8	⊖	◇	◇	⊖	⊖
16	⊖	◇	◇	⊖	⊖
33	⊖	◇	◇	◇	◇
83	⊖	◇	◇	◇	◇
141	⊖	◇	◇	◇	◇
166	⊖	◇	◇	◇	◇
333	⊖	⊖	◇	◇	◇
425	⊖	⊖	⊖/◇ (boundary)	◇	◇

Superdrawing: ◇ (DR>10; amorphous, unoriented)
Non-Superdrawing: ⊖ (crystallization, orientation)

The boundary of superdrawing in terms of temperature and strain rate has been determined. It exists below a strain rate of $33.3 \times 10^{-2} \text{ s}^{-1}$ at 105°C and gets pushed up to $42.5 \times 10^{-2} \text{ s}^{-1}$ at 110°C . With increasing draw temperature a transition in the crystallization mechanism leads to the dramatic shifting of this boundary to *above* $1.6 \times 10^{-2} \text{ s}^{-1}$ for temperatures of 115°C and 120°C . From the experimental results it is proposed that draw temperature of 113°C and strain rate of 0.17 s^{-1} are the critical values of the two main drawing parameters where the crossover regime in terms of crystallization exists. This crossover or transition can explain the shifting of the superdrawing parameter window as discussed above.

An explanation for the above findings is proposed based on the effects of both SIC and quiescent isothermal crystallization kinetics on the overall crystallinity development. At 105°C , flow drawing at slow strain rates is explained on the basis of the predominant occurrence of SIC only at fast rates. It is assumed that molecular relaxation prevents significant crystallization at slow strain rates. The effect of quiescent thermal crystallization, however, must also be considered. If the drawing process under a given set of conditions takes longer than the value of $t_{1/2}$ at that temperature, it gives sufficient time for crystallinity to develop during the drawing. The values of $t_{1/2}$ until the temperature of 110°C are so high that even the samples drawn at the slowest rate of 0.008 s^{-1} to very large draw ratios of ten (10) could not have developed significant crystallinity due to isothermal crystallization. But as the temperature goes above 110°C the half crystallization time ($t_{1/2}$) decreases quite significantly and becomes comparable to the draw time. Thus the quiescent crystallization has a profound effect on total crystallinity

above 110°C for some, if not all, draw conditions. The birefringence, a measure of overall orientation, was found to increase with strain rate until the draw temperature of 110°C. Thus for draw temperatures until 110°C there was some contribution from SIC to the crystallinity development, although the effect of isothermal crystallization was negligible. Their total contribution to crystallinity becomes large enough to yield non-superdrawn samples above certain critical strain rate. Since the rate of increase of birefringence at 110°C was slower than that at 105°C, this critical rate is higher at 110°C ($42.5 \times 10^{-2} \text{ s}^{-1}$) than at 105°C ($33.3 \times 10^{-2} \text{ s}^{-1}$). However as the draw temperature increases, the birefringence trend is reversed. So the orientation in drawn samples is smaller at higher strain rates. Also the effect of quiescent crystallization is significant only until a strain rate of $1.6 \times 10^{-2} \text{ s}^{-1}$. Thus if drawn at a rate greater than $1.6 \times 10^{-2} \text{ s}^{-1}$, the samples remain amorphous and unoriented for draw temperatures of 115°C and 120°C.

CHAPTER 5

MODELING THE NON-LINEAR VISCOELASTIC DEFORMATION BEHAVIOR OF PET FIBERS

5.1 Constitutive relations for the large strain stress-strain behavior of amorphous PET at different temperatures and strain rates

The principle aim of developing the model is to provide a good description of drawing of amorphous poly (ethylene terephthalate) at large strains above the glass transition temperature at various rates of deformation. Only a limited amount of work has been done to predict the PET fiber deformation behavior in the temperature range of 90-120°C deformed to draw ratios up to 9.

For this work, we identified the model's two core capabilities: first is to capture the evolution of crystallinity by phase transformation occurring during the stretching process; secondly to include the capability to predict stress-strain response to large deformations at stretching rates between 0.008 s^{-1} and 0.425 s^{-1} and temperatures in the range of 90-120°C.

It was found in the current experimental study that there are several regimes of mechanical behavior for as-spun PET fibers. The stress-strain response of PET was found not only to be highly non-linear but also exhibited a crossover effect with changing temperature and strain rate. In order to predict this extremely complex viscoelastic and

viscoplastic behavior in those deformation regimes, the proposed model invokes both the molecular structure-based and phenomenological approaches.

5.1.1 Summary of the model

The basic framework for the constitutive model follows prior modeling work on predicting time-dependent large strain deformation of polymers [106, 126, 127]. In particular, the approach and development build on the work of Boyce et al. [102]; Mulliken and Boyce [111] and Dupaix and Boyce [128, 129]. The model capability to account for crystallization effects is based on the approach of Ahzi and Makrabi [124] whereas the temperature dependence of network response is built on the work of Tassin et al. [143]. The highly non-linear yielding and strain hardening effects are modeled based on the work of Duan et al. [117]. They proposed a physical model built from four previous models, with modifications for capturing strain softening and strain stiffening at large strains (see also *Section 5.1.4.6*). Their new model (DSGZ model) was shown to satisfactorily capture the deformation behavior of glassy polymers, poly (methyl methacrylate) and polycarbonate, as well as a semi-crystalline polymer polyamide 12 at different strain rates and temperatures.

The models of Boyce et al. successfully captured the uniaxial compression behavior of PET at strain rates from 0.005 to 0.5 s⁻¹ and temperatures from 90 to 105°C for draw ratios up to 3. Ahzi et al. predicted the uniaxial tensile behavior of PET at strain rates of 0.05 to 2.1 s⁻¹ at 90°C and at strain rates of 0.01 to 0.42 s⁻¹ at 90 and 96°C. While those models used more complicated schemes such as network resistance decomposition into flow and relaxation [102] or upper and lower bounds of intermolecular resistance [125]

or splitting intermolecular resistance into α and β components [111], we have chosen the basic scheme of resistance decomposition as shown in *Figure 57*.

The original idea behind the constitutive model is the decomposition of resistance to deformation into two parts: intermolecular resistance to chain-segment rotation (elastic spring and viscous dashpot), and entropic resistance to chain alignment (Langevin spring). The intermolecular resistance has its origins in the intermolecular interactions between close lying polymer chain segments. These forces give rise to the initial stiffness and cause the material's plastic deformation at a finite stress (yield or flow stress). The entropic resistance arises from stretching and alignment of network polymer chains and contributes to hardening at large strains. This resistance also acts as a secondary contributor to the initial stiffness of the material. The non-linear viscous element contains the chain relaxation phenomena at high temperatures or slow rates of stretching. Both resistances act simultaneously and therefore treated as a parallel combination.

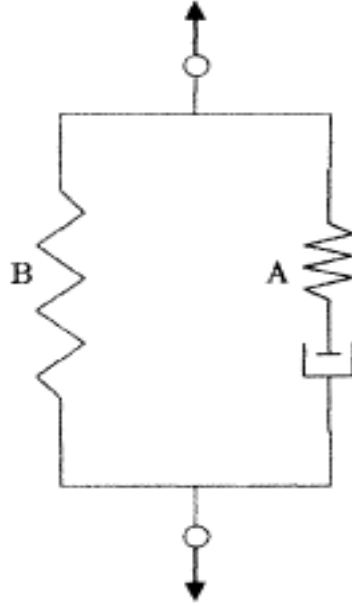


Figure 57. Schematic representation of breakdown of overall resistance to deformation

Therefore, built on the previous three-dimensional models, our proposed uniaxial one dimensional model for PET consists of three components: an elastic spring, a viscoplastic dashpot, and a non-linear Langevin spring. The dashpot and elastic spring act in series and are connected to the non-linear spring in parallel. Thus the strain in both the intermolecular resistance and the entropic network is equal to the applied strain

$$\varepsilon = \varepsilon_A = \varepsilon_B \quad (56)$$

The total stress is obtained as the sum of the stresses in the two resistances

$$\sigma = \sigma_A + \sigma_B \quad (57)$$

In this model the overall stress-strain behavior of PET is assumed to be comprised of two contributions:

- The intermolecular resistance (A) is responsible for the initial elastic behavior followed by yielding. This resistance changes with the strain-induced

crystallization in the material during drawing. The evolution of resistance A with increasing amount of strain has been captured by – (a) an elastic spring whose modulus (E) is not only dependent on the fraction of crystalline phase in the material but is also temperature dependent, (b) including the strain rate and temperature dependence of the viscosity coefficient (η).

- The network resistance (B) is responsible for the strain hardening behavior at large strains. It should be noted that although this resistance has been modeled as a macromolecular rubber-like network as in other works [102, 124, 129], it also contributes to the transitional characteristics (such as the roll-over to flow found at the intermediate strain rate of 0.166 s^{-1}) of mechanical behavior observed in the experimental results. This has been accomplished by incorporating phenomenological factors in its stress-strain relationship.

More details can be found in the description of the constitutive relations of both components as follows.

5.1.2 Intermolecular resistance (A)

The molecular resistance to deformation is modeled as an elastic spring in series with a viscous element. The instantaneous elasticity is accounted for by the spring whereas the delayed response is reflected in the dashpot response to applied strain. The constitutive equation given below relates the stress to the deformation conditions for intermolecular resistance:

$$\dot{\sigma}_A = \frac{E}{1000} \cdot \left(\dot{\epsilon} - \frac{\sigma_A}{\eta} \right) \quad (58)$$

where E is the elastic modulus, η is the viscosity parameter and $\dot{\epsilon}$ is the applied strain rate. This fairly simple model enables us to capture the non-linear behavior of PET under varying conditions of deformation by incorporating the temperature and strain rate dependence of the model parameters η and E .

Another form of the intermolecular resistance constitutive relation is based on the equation derived by Kawaguchi [43]:

$$\sigma = \frac{E}{1 + \epsilon} \cdot \left[(\tau\alpha)^2 \left(1 - e^{-\epsilon/\tau\alpha} \right)^2 + (\tau\alpha) \left(1 - e^{-\epsilon/\tau\alpha} \right) \right] \quad (59)$$

where $\alpha = \dot{\epsilon}$ is the applied strain rate, τ is the relaxation time constant and E is the elastic modulus. This expression is essentially the same as equation (58) at small strains.

5.1.2.1 Elasticity modeling

The material was treated as a three-phase composite (see *Figure 58*) whose elastic modulus E is not constant but varies with progressive deformation due to the occurrence of crystallization.

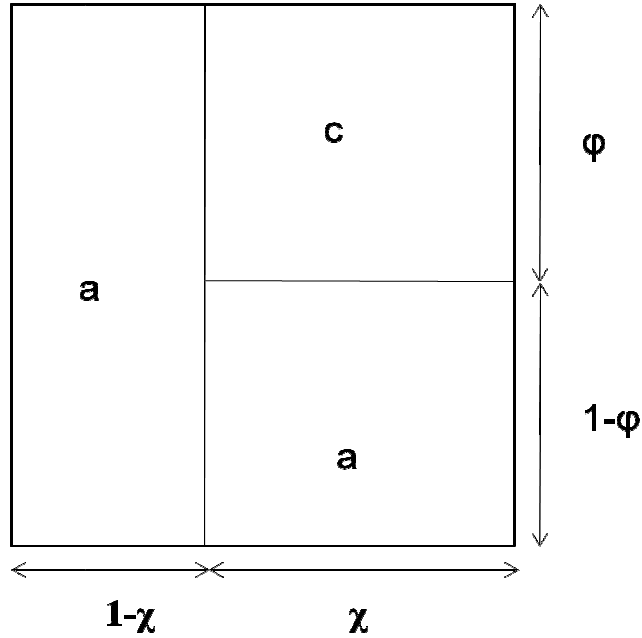


Figure 58. Schematic representation of the parallel-series model for determination of modulus

The effective elastic modulus of a short-fiber-reinforced composite is dependent not only upon the aspect ratio of fiber, the fiber volume fraction, the fiber-to-matrix stiffness ratio, but also upon the orientation of the fibers [144]. In our amorphous, unoriented material the contribution of either of the two phases to effective composite modulus is not known. Obviously the arrangement of chains in both the phases is not along the chain axis and therefore a distribution of orientation functions would be needed. The effect of orientation distribution on strength and elastic modulus has been extensively studied, and possible to predict, for two-dimensional structures. For short-fiber composites with three-dimensional fiber orientation distributions there is no precise format to predict the modulus. However, Kardos [144] gave an approximate expression for the average modulus of a structure with three-dimensionally random fiber orientation:

$$\bar{E} = \frac{1}{5} \cdot E_{11} + \frac{4}{5} \cdot E_{22} \quad (60)$$

where E_{11} and E_{22} are the longitudinal and transverse stiffnesses.

Based upon this result and equation (51), see the discussion in *Section 2.9*, the effective elastic constant of the composite is given as:

$$E = \left(\frac{\chi}{\frac{\varphi}{E_c} + \frac{(1-\varphi)}{E_a}} \right) + ((1-\chi) \cdot E_a) \quad (61)$$

where E_c is the elastic constant of crystalline phase of PET and E_a is the elastic constant of amorphous phase of PET. The parameter φ is the ratio of the mean crystallite length (L) to the long period (LP) of the material. The experimental determination of L and LP for PET with x-ray scattering techniques has yielded the value of φ roughly equal to 0.46 [133, 138] which was used for the present calculations.

The parameter χ is defined as

$$\chi = \frac{x}{\varphi} \quad (62)$$

$$x = \frac{y \cdot \rho_0}{\rho} \quad (63)$$

where x is the volume fraction crystallinity of the material, y is the weight fraction crystallinity (measured with DSC), ρ is the density of the PET sample used (1336 kg/m³) and ρ_0 is the density of the crystalline PET (1455 kg/m³) [145].

5.1.2.2 Effect of crystallization

The occurrence of crystallization has profound effects on the stress-strain behavior of the material: Firstly, it alters the intermolecular resistance by formation of new crystalline regions and a decrease in the fraction of amorphous domains. Secondly, it causes molecular relaxation to cease after a critical level of stretch [102]. This effect was captured through the evolution of the weight fraction of crystallinity, y , with drawing time. The variation of y as a function of time was determined at each condition from the known values of degree of crystallinity at different draw ratios (equivalent to different draw times) for that condition. The assumption was that thermal crystallization and stress-induced crystallization could be accounted for by having a single crystallization parameter representing the overall crystallinity of material. The separation of the two crystallization phenomena is not expected to change the current model's predictions.

5.1.3 Entropic resistance (B)

This resistance is responsible for the stress upturn at large strains. It has been modeled by treating the polymer as a non-permanent network structure of entanglements [143]. The stress in the network is assumed to have purely entropic origins based upon the deformation of the monomer units between entanglement points. The expression relating the stress to the uniaxial extension conditions is obtained by the classical rubber-elasticity theory for large strains as

$$\sigma_B = \frac{\rho RT}{3M_s} \lambda_{\max} \lambda L^{-1} \left[\frac{\lambda}{\lambda_{\max}} \right] \quad (64)$$

where λ_{max} is the limiting stretch ratio on each chain, λ is the draw ratio along the stretching direction, $\rho=1336 \text{ kg/m}^3$ is the polymer mass per unit volume, M_s is the molar mass of the “elastic subchain”, T is the absolute temperature, $R=8.3144 \text{ J K}^{-1} \text{ mol}^{-1}$ is the universal gas constant and L^{-1} is the inverse Langevin function

$$L^{-1}[\beta] = 3\beta + \left(\frac{9}{5}\right)\beta^3 + \left(\frac{297}{175}\right)\beta^5 \quad (65)$$

The value of λ_{max} represents the maximum stretch that can be applied to the network after which the entanglement slippage ceases. The entanglement points begin to act as ‘crystallites’ or ‘tie-points’ that causes a large upturn in network stress. It was observed from the stress-strain curves of PET that the point of stress upturn varies in a non-linear fashion and may be not seen at all in some cases. Buckley and Jones [104] modeled the hardening behavior of PET at temperatures above T_g using the above classical rubber-elasticity model. However, their results specifically demonstrated the inability of a rubber–elastic network model to capture the strong temperature dependence of hardening observed at these temperatures in PET. In order to enable the model to capture this non-linear and complicated behavior it is necessary to introduce other functional variables in the classical constitutive relation of a rubber network. In this work it is proposed to modify the stress-strain relation as following:

$$\sigma_B = f(\varepsilon) \cdot \sigma_0 + C \cdot \frac{\rho RT}{3M_s} \lambda_{max} \lambda L^{-1} \left[\frac{\lambda}{\lambda_{max}} \right] \quad (66)$$

The constant σ_0 , with units of MPa, is multiplied with $f(\varepsilon)$ and is calculated from the stress-strain curves at each deformation condition.

The approach adopted by us in this work is to make the following modifications in the molecular network's constitutive relation:

- In order to capture the temperature dependence of the network response a temperature dependence of the network properties was included. As the temperature is increased, some entanglements will become ineffective and M_s will increase thereby causing a decrease in the hardening modulus [102, 123, 126].
- The approach to account for the non-linear yielding and strain hardening characteristics is based on the 'DSGZ model' proposed by Duan et al. [117] by inclusion of $f(\varepsilon)$:

$$f(\varepsilon) = \left(e^{-C_1 \cdot \varepsilon} + \varepsilon^{C_2} \right) \cdot \left(1 - e^{-\alpha \cdot \varepsilon} \right) \quad (67)$$

where C_1 , C_2 and α are the strain, strain rate and temperature dependent parameters determined from the uniaxial tension test results. $f(\varepsilon)$ is the dimensionless variable which enables to include strong strain, strain rate and temperature dependence of stress as observed in experimental results.

The constant C in equation (66) represents the strong non-linear strain rate and temperature dependence of the hardening behavior exhibited under the deformation conditions of this work. It serves as a sensitivity parameter whose value varies between 0 and 1. Table 12 lists the values of the two constants C and σ_0 as given below:

Table 12. The values of constant of the hardening parameter (σ_0) and the sensitivity coefficient (C) at all deformation conditions

Strain rate (s ⁻¹) Draw temperature (°C) ↓	C			σ_0 (MPa)		
	0.008	0.166	0.425	0.008	0.166	0.425
90	0	0	0	0.043	0.138	0.104
105	1	0	1	0.234	0.054	1.108
110	1	0	0	0.4	0.282	1.887
115	1	0	0	0.024	1.335	0.99
120	1	0.5	1	0.3	0.337	0.878

5.1.4 Model parameters

The following sections contain the detailed description of determination methods for all the model coefficients involved in this study.

5.1.4.1 Viscosity parameter: η

The variation of the viscosity coefficient with temperature and strain rate was taken as follows based upon the data of Kawaguchi [43]:

$$\eta = (\dot{\epsilon})^{-0.512} \cdot \exp\left\{-24.3 + 15100 \cdot \left(\frac{1}{T}\right)\right\} \quad (68)$$

where $\dot{\epsilon}$ is the applied strain rate (% min.⁻¹) and T is the draw temperature (°K). Therefore the strain rate and temperature dependent viscosity constant is determined at each condition of deformation as shown in Table 13 below.

Table 13. Viscous dashpot parameter η (MPa.s) at all deformation conditions

Strain rate (s^{-1}) \rightarrow Draw temperature ($^{\circ}C$) \downarrow	0.008	0.166	0.425
90	430512.2	92866.28	57505.52
105	82621.46	17822.37	11036.13
110	49046.41	10579.85	6551.35
115	29509.29	6365.48	3941.69
120	17985.6	3879.69	2402.42

5.1.4.2 Initial modulus of the crystalline phase: E_c

As discussed in *Section 2.9*, the elastic constant of PET crystalline phase has been measured by various workers using different experimental techniques and different methods of calculation. The apparent fiber modulus E_f has been shown to be only a fraction of the crystal modulus E_c because of poor orientation and low crystallinity. This ratio ($E_c \sim 6E_f$) was used to determine E_c from the value of E_f given in the data of Kawaguchi's work [43]. Table 14 below shows values of PET crystal modulus E_c at each temperature of deformation.

Table 14. Young's modulus of crystalline phase of PET (GPa) at all deformation conditions

Temperature ($^{\circ}C$)	90	105	110	115	120
E_c	59.09	36.01	30.00	26.30	24.00

5.1.4.3 Initial modulus of the amorphous phase: E_a

Literature review showed that the elastic modulus of amorphous phase of fibers E_a is generally a certain fraction of the fiber modulus E_f . This ratio ($E_a \sim 0.5E_f$) was used to determine E_a from the value of E_f given in the data of Kawaguchi's work [43]. The calculated values of E_a are listed in Table 15 below.

Table 15. Young's modulus of amorphous phase of PET (GPa) at all deformation conditions

Temperature (°C)	90	105	110	115	120
E _a	4.92	3.00	2.50	2.19	2.00

5.1.4.4 Limiting stretch ratio of the amorphous PET network: λ_{max}

The maximum draw ratio is obtained [143, 146] from the expression:

$$\lambda_{max} = \frac{l_p}{l} \left(\frac{3N_e}{C_\infty} \right)^{1/2} \quad (69)$$

where l_p is the average projected length of each flexible unit along the chain axis, l is the average length of a flexible unit in PET repeat unit, N_e is the number of links between entanglements and C_∞ is the characteristic ratio of PET. For PET, C_∞ has been taken as 4.2 [143], $l=2.68$ Å, $N_e=133$ and $l_p=1.79$ Å yielding the value of λ_{max} equal to 6.509.

5.1.4.5 Molar mass of the PET elastic subchain: M_s

The values of the molar mass were taken from Lorentz and Tassin [143] at each deformation temperature involved, as shown in Table 16. The molecular weight of the PET used in their study ($M_w=40000$ g mol⁻¹) was very close to the one used in our experiments ($M_v=41233.74$ g mol⁻¹).

Table 16. Values of the molar mass of subchain of PET network (From Ref. 143)

Temperature (°C)	90	105	110	115	120
M _s (kg mol ⁻¹)	8	18	22	31	40

5.1.4.6 Constants of the hardening parameter: C_1 , C_2 , α and σ_0

The DSGZ model by Duan et al. [117] as given below in original form,

$$\sigma(\varepsilon, \dot{\varepsilon}, T) = K \cdot \left\{ f(\varepsilon) + \left[\varepsilon \cdot e^{\left(1 - \frac{\varepsilon}{C_3 \cdot h(\dot{\varepsilon}, T)}\right)} - f(\varepsilon) \right] \cdot e^{[\ln(h(\dot{\varepsilon}, T)) - C_4] \varepsilon} \right\} \cdot h(\dot{\varepsilon}, T) \quad (70)$$

$$h(\dot{\varepsilon}, T) = (\dot{\varepsilon})^m e^{\left(\frac{\alpha}{T}\right)} \quad (71)$$

, consists of eight constants that were computed from compression data. The calibration procedure employed by them was used by us to arrive at the four constants that have been used in our model. The data of at least three experimental stress-strain curves at different strain rates and temperatures was used for computations.

For a stress-strain curve at large strain, the equation of stress can be approximately written as:

$$\sigma(\varepsilon, \dot{\varepsilon}, T) = K \cdot \left(e^{-C_1 \cdot \varepsilon_1} + \varepsilon_1^{C_2} \right) \cdot h(\dot{\varepsilon}, T) \quad (72)$$

For three large strain points on a curve, $(\varepsilon_1, \sigma_1)$, $(\varepsilon_2, \sigma_2)$ and $(\varepsilon_3, \sigma_3)$, the following system of equations can be obtained:

$$\begin{aligned} \frac{e^{-C_1 \cdot \varepsilon_1} + \varepsilon_1^{C_2}}{e^{-C_1 \cdot \varepsilon_2} + \varepsilon_2^{C_2}} &= \frac{\sigma_1}{\sigma_2} \\ \frac{e^{-C_1 \cdot \varepsilon_1} + \varepsilon_1^{C_2}}{e^{-C_1 \cdot \varepsilon_3} + \varepsilon_3^{C_2}} &= \frac{\sigma_1}{\sigma_3} \end{aligned} \quad (73)$$

Thus the values of C_1 and C_2 were obtained by solving equation (73) using an iteration code in MATLAB.

The value of α was determined based on the following approximate equation proposed by Duan et al.:

$$\alpha = -\frac{\ln(0.03)}{\varepsilon_s} \quad (74)$$

where ε_s is the strain at the end of softening at the given deformation condition.

The fitted values of all of the three non-linear hardening parameters are given in Table 17 below.

Table 17. The values of constants of the non-linear hardening parameter $f(\varepsilon)$: C_1 , C_2 and α , at all deformation conditions

Strain rate (s ⁻¹) Draw temperature (°C) ↓	C_1			C_2			α		
	0.008	0.166	0.425	0.008	0.166	0.425	0.008	0.166	0.425
90	-1.699	-1.456	-1.429	-0.9902	-0.6007	-0.794	1.5049	1.6576	1.7081
105	16.574	0.9912	-0.218	0.454	-1.51	-0.507	0.7622	2.805	0.8231
110	1.577	0.5656	0.483	0.294	-0.0765	-0.845	0.718	3.615	0.3489
115	-0.2313	2	0.563	0.1911	-1.44	-0.942	1.0182	1.0219	0.7165
120	1.9728	1.311	0.5656	1.194	0.0278	-0.56	1.3058	3.9667	1.2896

5.2 Comparison of predictions with experiment

The stress-strain curves of PET were generated using the proposed model at three representative strain rates: 0.008 s⁻¹, 0.166 s⁻¹ and 0.425 s⁻¹ and five temperatures: 90°C, 105°C, 110°C, 115°C and 120°C. The procedure for systematically fitting data to the model was carried out to obtain values of the model parameters which best described the

stress-strain curves in terms of the experimental results. They are plotted together with the experimental observations as seen in *Figures 59 to 63*. The model is adequately able to predict the non-linear viscoelastic behavior of amorphous PET at all conditions.

The experimental observations of the mechanical behavior of amorphous PET at the aforementioned conditions can be roughly divided into four groups or categories:

- a) Group I: This type of behavior involves an initial elastic response followed by flow, until a draw ratio depending upon the conditions, and finally dramatic upturn in stress values due to stiffening.
- b) Group II: This type of behavior involves an initial elastic response followed by yield and finally flow with no stiffening.
- c) Group III: This group is essentially similar to Group II with the difference lying in the small to moderate amount of stiffening seen at different stages of drawing.
- d) Group IV: This group exhibits no yielding and the initial linear elastic response is difficult to differentiate from hardening.

We now discuss all the predicted results with respect to the experimental observations.

5.2.1 90°C

At this temperature all the curves fall into Group I (see *Figure 59*). At all strain rates they are characterized by a sigmoid shape, with large strain hardening appearing at a draw ratio of 3.05, 3.11 and 3.32 for 0.425 s^{-1} , 0.166 s^{-1} and 0.008 s^{-1} respectively. The simulation results show small deviation from the flow behavior before the stress upturn at 0.425 s^{-1} and 0.166 s^{-1} whereas the point (draw ratio) of stress upturn seems delayed for

all strain rates. This may be attributed to the insignificant effect of intermolecular resistance to yielding.

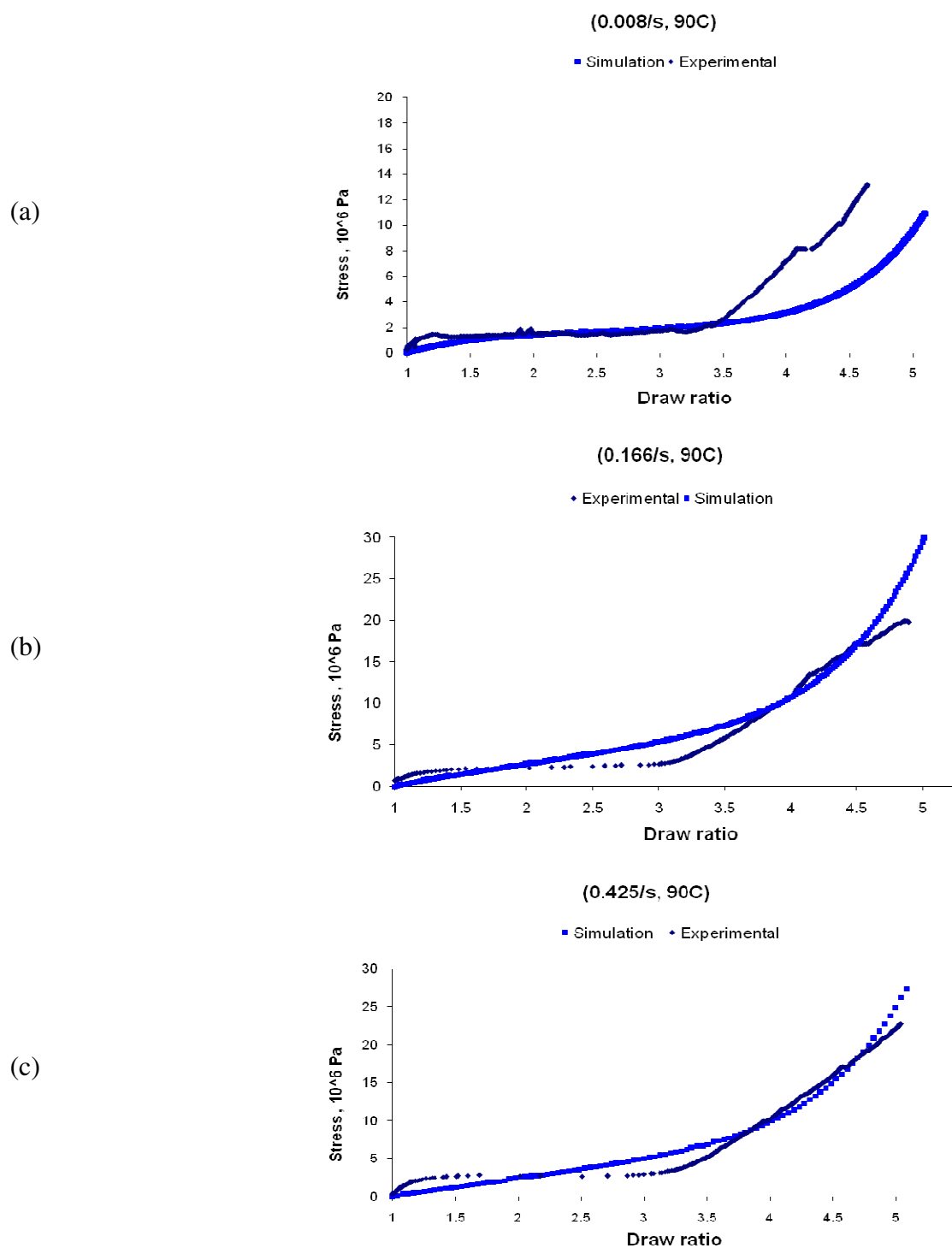


Figure 59. Predicted stress-strain curves at the draw temperature of 90°C for the strain rates of (a) 0.008 s⁻¹, (b) 0.166 s⁻¹ and (c) 0.425 s⁻¹

5.2.2 105°C

As shown in *Figure 60* the curves fall into Group I, II and IV respectively for 0.425 s^{-1} , 0.166 s^{-1} and 0.008 s^{-1} . This is easily explained by there being a much more complex deformation mechanism due to crystallization and relaxation effects. At strain rate of 0.008 s^{-1} the predictions are very close to the observed results except slight deviation at draw ratio greater than 5. At 0.166 s^{-1} , the prediction follows the general trend. At the strain rate of 0.425 s^{-1} the predictions exhibit a gradual change in slope during hardening.

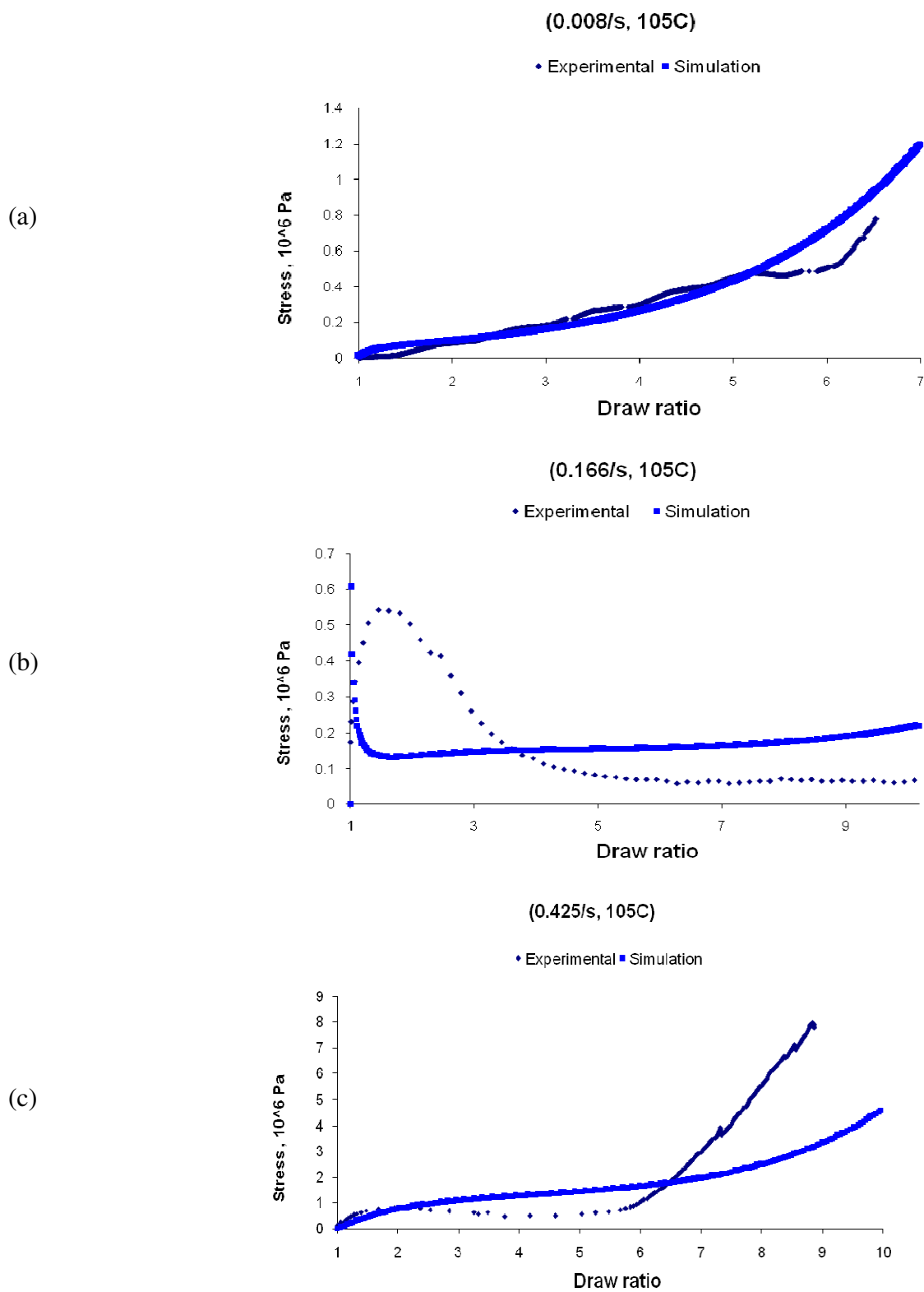


Figure 60. Predicted stress-strain curves at the draw temperature of 105°C for the strain rates of (a) 0.008 s^{-1} , (b) 0.166 s^{-1} and (c) 0.425 s^{-1}

5.2.3 110°C

The curves for 0.425 s^{-1} and 0.166 s^{-1} fall into Group II and in Group IV for 0.008 s^{-1} . At strain rate of 0.008 s^{-1} the predictions are very close to the observed experimental curves (see *Figure 61*). At strain rate of 0.166 s^{-1} and 0.425 s^{-1} the predictions are very close to the experiment initially as well as at yield point and after roll-over to flow. Again for both larger strain rates, the severity of the roll-over to flow is predominant in the experiments.

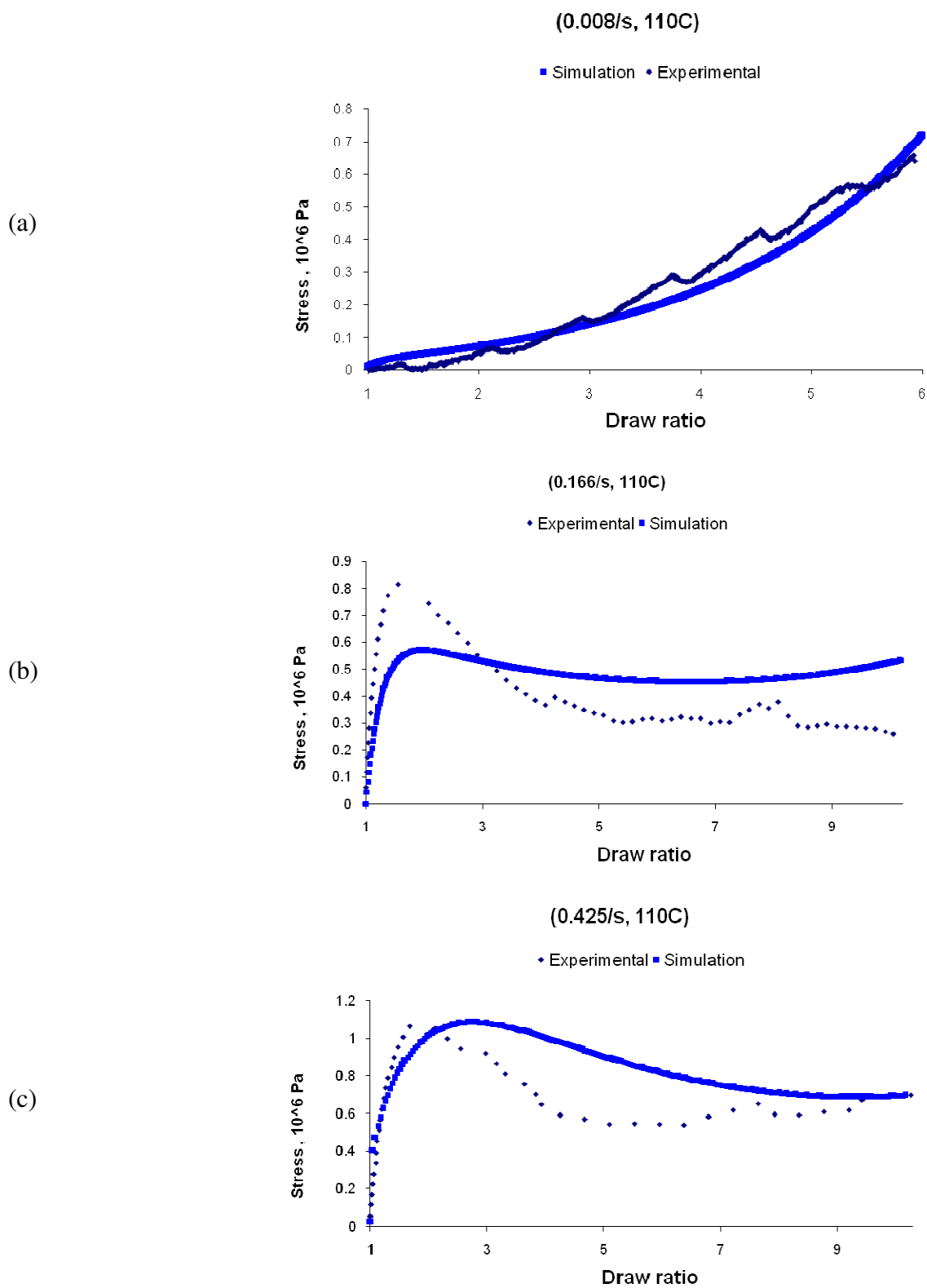


Figure 61. Predicted stress-strain curves at the draw temperature of 110°C for the strain rates of (a) 0.008 s^{-1} , (b) 0.166 s^{-1} and (c) 0.425 s^{-1}

5.2.4 115°C

As shown in *Figure 62* the curves fall into Group II, III and IV respectively for 0.425 s^{-1} , 0.166 s^{-1} and 0.008 s^{-1} . At strain rate of 0.008 s^{-1} the predictions are very close to the observed results, while at 0.425 s^{-1} the predictions slightly deviate from the initial and intermediate strain behavior although they match the experimental curve qualitatively. Again for the strain rate of 0.166 s^{-1} the predictions qualitatively match the observations.

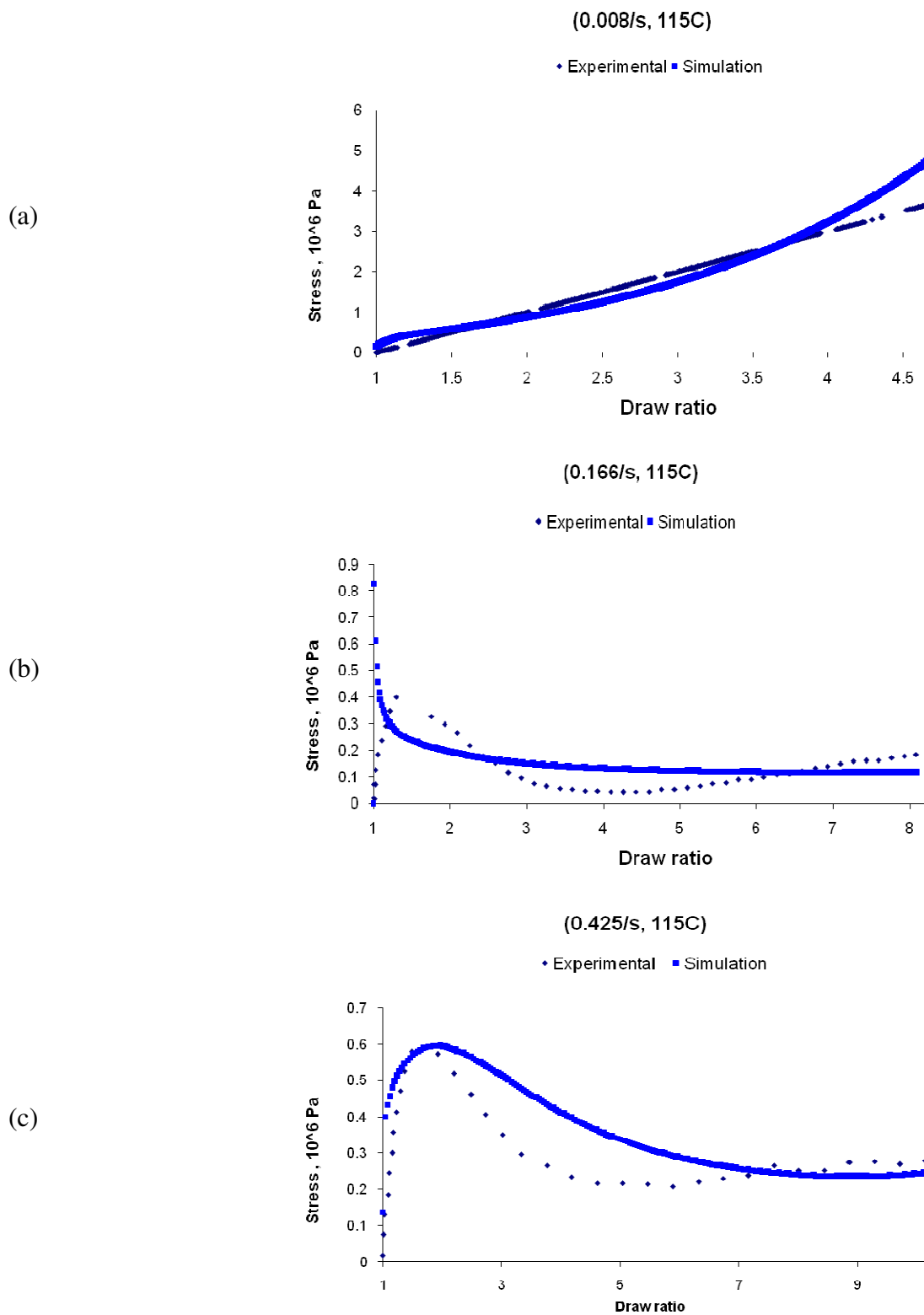


Figure 62. Predicted stress-strain curves at the draw temperature of 115°C for the strain rates of (a) 0.008 s⁻¹, (b) 0.166 s⁻¹ and (c) 0.425 s⁻¹

5.2.5 120°C

The curves for 0.425 s^{-1} and 0.166 s^{-1} fall into Group III and in Group IV for 0.008 s^{-1} . Again the model was able to predict the observed results very well for the strain rate of 0.008 s^{-1} . At strain rate of 0.166 s^{-1} the predictions are very close to the experiment initially but deviate at yield point. At 0.425 s^{-1} the predictions are very close to the experimental curves (see *Figure 63*).

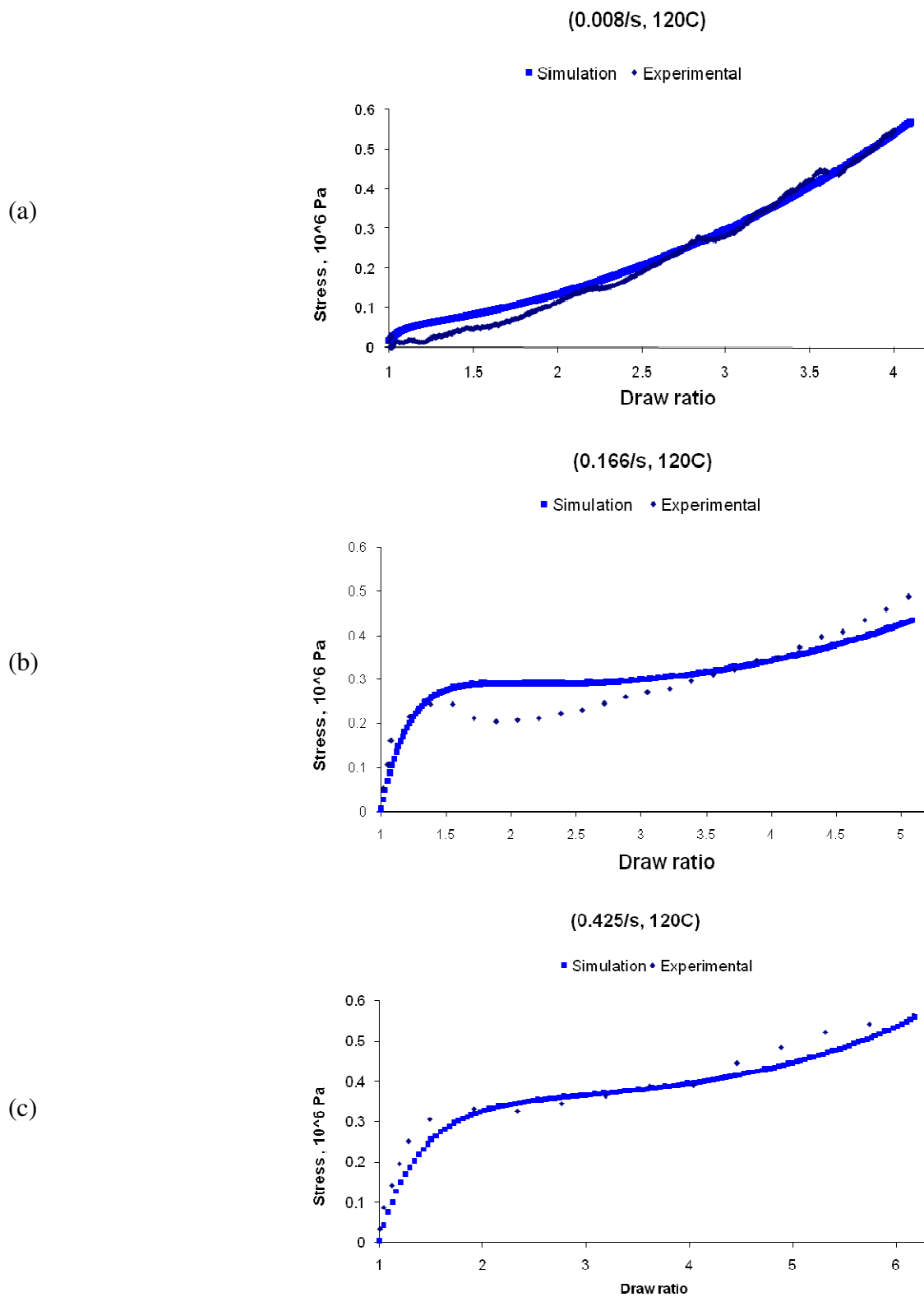


Figure 63. Predicted stress-strain curves at the draw temperature of 120°C for the strain rates of (a) 0.008 s^{-1} , (b) 0.166 s^{-1} and (c) 0.425 s^{-1}

5.3 Evolution of crystallinity

Figures 64 through 66 show the development of weight fraction crystallinity, y , with the progress of drawing. The calculations were done based on the equation of y as a function of time of drawing obtained from the measured values of y with DSC. The graphs show that the rate of crystallinity development is fastest at all strain rates for the draw temperature of 90°C. It is clearly seen in *Figure 64* that for the strain rate of 0.008 s⁻¹ the rate of crystallinity development is faster at the temperatures of 115 and 120°C in comparison to that observed at 105 and 110°C. In contrast at 0.425 s⁻¹ the crystallinity evolves much faster at draw temperatures of 105 and 110°C relative to that at 115 and 120°C (see *Figure 66*). This transition suggests that the crystallization mechanism undergoes a transition at 110°C. Also since the rate of crystallinity growth appears to be similar for all draw temperatures (except for 90°C where contribution of SIC is much greater) at the strain rate of 0.166 s⁻¹ it can be taken as a threshold strain rate after which the crossover in crystallization mechanism occurs.

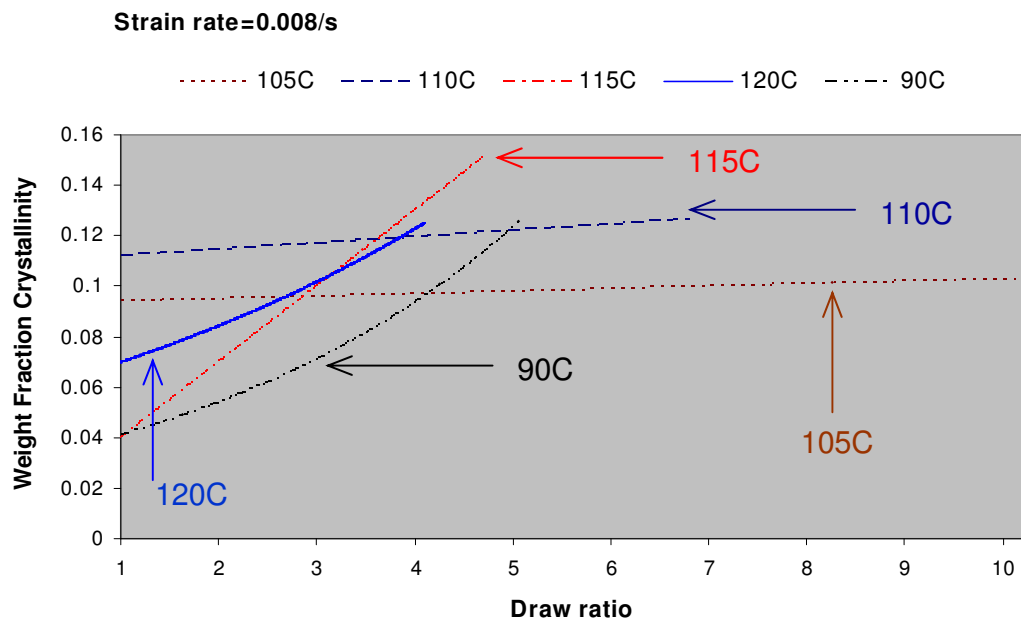


Figure 64. The evolution of weight fraction crystallinity (calculated), y , with time of drawing at the strain rate of 0.008 s^{-1} for all draw temperatures

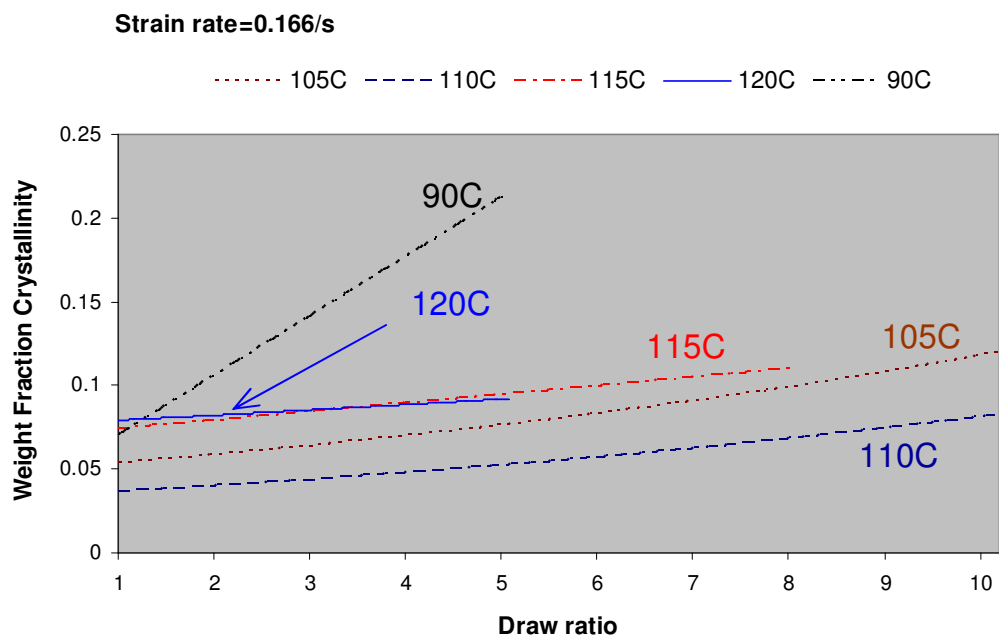


Figure 65. The evolution of weight fraction crystallinity (calculated), y , with time of drawing at the strain rate of 0.166 s^{-1} for all draw temperatures

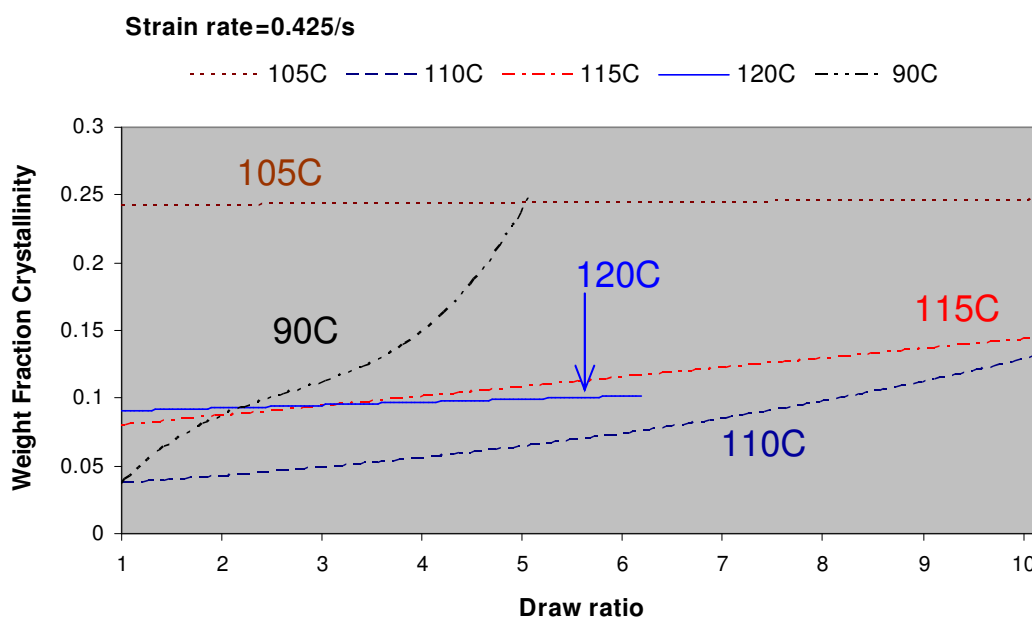


Figure 66. The evolution of weight fraction crystallinity (calculated), y , with time of drawing at the strain rate of 0.425 s^{-1} for all draw temperatures

5.4 Significance of model parameters

The viscosity coefficient (η) depends upon not only the temperature but also the strain rate. The graphs in *Figure 67 (a)* and *(b)* have been plotted to show how the viscosity coefficient changes with strain rate and temperature in the range of our experimental conditions. At a given temperature, the viscosity coefficient drops largely then shows a less sharp decrease with increasing strain rate, as seen in *Figure 67 (b)*. This is easily explained by the fact that at larger rates of deformation only the short time-scale response of polymer molecules is probed. This behavior was observed at all draw temperatures.

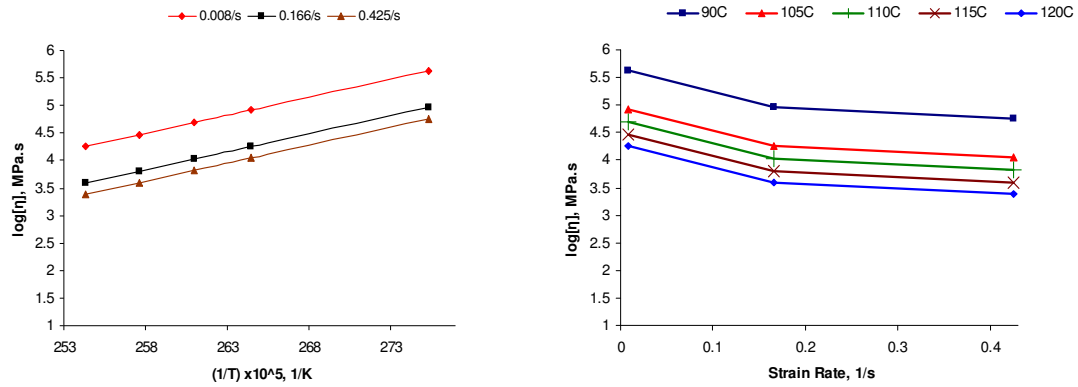


Figure 67. Variation of viscosity coefficient (η) of the intermolecular resistance with (a) $1/\text{temperature}$ and (b) strain rate [data adapted from Ref. 43]

At a given strain rate, the viscosity coefficient η decreases with increasing temperature, as seen in *Figure 67 (a)*. The decrease in η with temperature can be attributed to significant molecular relaxation at higher temperatures above the glass transition. This behavior was observed at all strain rates.

The value of the coefficient C2 has the most significant effect on the predicted stress-strain curve at a given condition. C2 was taken positive where hardening takes place while its value is negative for including yielding in the stress-strain behavior. For example the stress-strain behavior at the strain rate of 0.166 s^{-1} is similar and exhibits a roll-over to ‘permanent flow’ at all temperatures except 120°C . Accordingly, the value of C2 is positive only for the draw temperature of 120°C .

The value of C is the next significant factor affecting the results of the modeling. The reason of having the value of C equal to 0 or 1 is a need to control the dramatic hardening

at certain conditions. The stress upturn is implicit in the rubber-elasticity expression due to formation of trapped network by crystallization. But at certain drawing conditions, particularly at strain rate of 0.166 s^{-1} , there is no strain hardening even at large strains. The presence of dominant flow behavior was modeled by using C equal to zero and suppressing the rubber-elasticity contribution. At other conditions (see Table 12) the value of C was taken equal to one where neither hardening nor flow behavior was dominant.

The limiting elasticity of the entanglement network was defined in the form of the parameter λ_{max} . Its value of 6.5 was calculated by using $M_e = 4.2 \text{ kg mol}^{-1}$ in the equation $N_e = M_e/32$ where 32 g mol^{-1} is the average molecular weight of PET repeat unit. This yielded a higher value of N_e (=133) than used by Lorentz and Tassin [143] and correspondingly the maximum stretch ratio λ_{max} was much higher. A higher value of λ_{max} obviously means that the dramatic upturn in stress is seen at higher strains. This approach seems justified based upon the experimental observation of very large draw ratios with only little hardening exhibited by amorphous PET samples of this study.

The molecular relaxation mechanisms during the deformation of the network were reflected in M_s – average molar mass of the flexible subchain. In this model M_s , the apparent “mesh size” for PET, was assumed to increase with increasing temperature. This can be easily explained by the fact that at higher temperatures relaxation times are smaller leading to more relaxation during drawing. In other words some entanglements of the network become ineffective with increasing temperature for a given rate of stretching,

resulting in a larger apparent “mesh size”. It is also possible to vary the mesh size with strain rate but for this model M_s was independent of strain rate.

5.4.1 Deficiencies in the model and possible ways of improvement

The major inadequacy of the model was that it requires the use of many constants to be obtained from the experimental data. The very large draw ratios and non-linear strain-stiffening and flow behavior involved in the experimental observations made it necessary to include some data-fitted constants so that all conditions of stretching could be predicted closely. Also the yield followed by flow behavior at the strain rate of 0.166 s^{-1} and temperatures of 105°C to 115°C needs improvement in model predictions. It is thought that the transition in crystallization mechanism at this rate has influenced the model capability.

If the values of C_1 and C_2 are calculated using the whole stress-strain curve instead of a few points, the predictions are expected to improve. If the strain rate dependence of M_s – average molar mass of the flexible subchain – is also included in addition to the temperature dependence used in this model, the model results would be closer to the experimental data. Of course, eventually the use of a fewer constants would result in a better model.

5.4.2 Model predictions at other drawing conditions

The use of this model to extend the prediction capability to other conditions can be achieved if the constants are determined. Also it is applicable for predicting the mechanical behavior of other crystallizable polymers.

5.5 Summary

A one-dimensional constitutive model based on the rubber elasticity theory, the parallel-series model and phenomenological data fitting was used to predict the stress-strain curves of PET fibers at three strain rates each for five temperatures above the glass transition temperature. The overall stress-strain curve was constructed from adding the network contribution (resistance B) to the intermolecular resistance (A). The resistance A was modeled to contain the initial elastic response as well as the effect of crystallization. The elastic modulus of the intermolecular resistance evolves with the occurrence of crystallization. The model employs strain rate as well as temperature dependence of the viscous response of intermolecular resistance. The network contribution to stress (B) was quantified on the basis of conformational properties of the PET network.

It was found that the strong strain, strain rate and temperature dependence of mechanical behavior observed in drawing of PET fibers could be adequately captured by the model. An attempt was made to model the stress-strain behavior of PET fibers deformed to very large draw ratios (up to 10) in a wide range of temperature (90-120°C) and strain rate (0.008-0.425 s⁻¹). These types of conditions have not been modeled explicitly for PET fibers by other researchers. The transition in mechanical behavior, observed at strain rate of 0.17 s⁻¹ and temperature of 113°C in our experimental study, was demonstrated by the model. Draw ratios larger than the maximum draw ratio of entanglement network were obtained at some conditions. This could be attributed to molecular relaxation processes occurring at those conditions.

CHAPTER 6

CONCLUSIONS AND FUTURE DIRECTIONS

6.1 Conclusions

Comprehensive experimental studies were conducted to characterize the structure of PET fibers drawn at different temperatures, strain rates and to different draw ratios. Uniaxial stretching experiments were performed on amorphous PET fibers above the glass transition temperature. PET fiber samples deformed to different draw ratios were characterized for the structural changes by DSC and birefringence measurements. In this study, if a sample can be extended to a draw ratio of 10 ($\lambda \geq 10$) under a low draw stress, this drawing behavior is considered to be superdrawing. It was found that the superdrawing produces a molecular structure with a low degree of orientation and insignificant changes in crystallinity of the original sample. This is evidenced by an essentially similar cold crystallization exotherm area and low birefringence values.

At a draw temperature just above the glass transition (90°C) significant strain-induced crystallization (SIC) leads to high draw stress levels and failure at small draw ratios for all strain rates involved. At 90°C a large upturn in stress occurs at a draw ratio of three, indicating the predominant SIC mechanism at this temperature for all strain rates. As draw temperature went up to 105°C the draw stress went down considerably and prevalent molecular relaxation mechanisms lead to superdrawing for strain rates below $33.3 \times 10^{-2} \text{ s}^{-1}$.

With increasing temperature to 110°C, the draw stress levels drop further and increased relaxation results in superdrawing up to $42.5 \times 10^{-2} \text{ s}^{-1}$. But orientation, as reflected by the birefringence values, showed an increase with increasing strain rate. Thus crystallization occurred mainly due to SIC at these temperatures, since the isothermal crystallization is assumed to play a negligible role as evidenced by the large half-crystallization times. Thus for a given temperature in this regime, the overall crystallinity grows with increasing strain rate and yields non-superdrawn samples after a critical rate. The rate of increase of orientation at 110°C was found to be slower than that at 105°C, leading to a higher critical rate at 110°C ($42.5 \times 10^{-2} \text{ s}^{-1}$) than at 105°C ($33.3 \times 10^{-2} \text{ s}^{-1}$). On further increasing the temperature to 115°C and up to 120°C, drawing occurs at very low stress levels. Also the significantly reduced half-crystallization times mean that thermal effects would expectedly have a large effect on overall crystallinity. However the orientation *decreased* with increasing rate in this regime. Additionally it was found that temperatures greater than 110°C resulted in *less* crystallization at strain rates faster than $1.6 \times 10^{-2} \text{ s}^{-1}$ after which presumably the time of drawing becomes too small for significant crystallization to occur. Thus unoriented and non-crystalline samples in this regime were obtained only until the strain rate of $1.6 \times 10^{-2} \text{ s}^{-1}$. From the above results a parameter window/boundary of superdrawing in terms of temperature and strain rate was defined. It exists below a strain rate of $33.3 \times 10^{-2} \text{ s}^{-1}$ at 105°C and gets pushed up to $42.5 \times 10^{-2} \text{ s}^{-1}$ at 110°C. A crossover of the crystallization regimes at around 113°C leads to the dramatic shifting of this boundary to *above* $1.6 \times 10^{-2} \text{ s}^{-1}$ for temperatures of 115°C and 120°C.

A new constitutive model was proposed to predict the stress-strain behavior of PET fibers deformed to very large draw ratios (up to 10) in a wide range of temperature (90-120°C) and strain rate (0.008-0.425 s⁻¹). These types of conditions have not been modeled explicitly for PET fibers by other researchers. A one-dimensional constitutive model based on the rubber elasticity theory and non-linear viscoelasticity was built to simulate the stress-strain curves of PET fibers at three representative strain rates each for five temperatures above the glass transition temperature. The overall stress-strain curve was constructed from the stresses arising from an intermolecular resistance (A) and a network resistance (B). The intermolecular resistance was modeled to represent the initial elastic response followed by yielding. The effect of crystallization was accounted for by increasing intermolecular resistance and increased elastic modulus of the material. The model also accounted for the strain rate and temperature dependence of the time-dependent response of intermolecular resistance. The network contribution to stress, which represented the strain hardening at large strains, was quantified on the basis of conformational properties of the PET network. The temperature dependence of one of the network properties (M_s , molar mass of elastic sub-chain of PET) allowed us to capture the observed non-linear temperature dependence of stiffening. It was found that the strong strain, strain rate and temperature dependence of mechanical behavior observed in drawing of PET fibers could be adequately captured by the model.

In short, this study has helped us gain new insights into the PET fiber superdrawing behavior and provided a better understanding of the crystallization mechanisms over a wide range of conditions. The transition regimes of crystallization behavior and

orientation development revealed in this study were not reported in previous research: firstly that increasing draw temperature from 110 to 120°C leads to more crystallization at small strain rates (10^{-3} s^{-1}) and less crystallization at high strain rates (10^{-1} s^{-1}); secondly that for strain rates below about 0.17 s^{-1} the orientation *increases* with increasing temperature.

6.2 Future directions

Since the processing of PET in many commercial applications occurs at very high rates of deformation, an experimental study involving the study of drawing behavior at faster rates of stretching ($> 1 \text{ s}^{-1}$) is proposed for the further work. Also biaxial drawing behavior of PET in a similar range of conditions needs more investigation. The use of online x-ray diffraction and birefringence measurements is recommended to form a clearer picture of crystallinity and orientation evolution during drawing. It is hoped that those methods will also give a better understanding of whether strain-induced crystallization is initiated during the drawing process itself or after it has ceased. It is also needed to elucidate whether or not the initiation of crystallite formation process depends upon the draw ratio reached.

The one-dimensional constitutive model for drawing behavior of PET needs further improvement by reducing the number of constants required. The use of strain rate dependence of the mesh size M_s in the network resistance could improve the strain hardening predictions. A more complicated intermolecular resistance model (e.g. three- or four-element models) is recommended to improve the model capability for capturing

non-linear viscoelastic features. Although molecular theory based three-dimensional models are extremely complicated to implement numerically, they do not rely too much on experimental data and are recommended for more precise simulation capabilities. Those models will also extend the predictions over a much larger range of drawing conditions, especially faster deformation rates.

REFERENCES

1. Swallowe, G.M. and J.O. Fernandez, *Crystallization effects during high rate deformation of polymers*. Journal De Physique. IV : JP, 2000. **10**(9): p. 311.
2. Misra, A. and R.S. Stein, *Stress-Induced Crystallization of Poly(Ethylene Terephthalate)*. Journal of Polymer Science, Polymer Physics Edition, 1979. **17**(2): p. 235.
3. Blundell, D.J., et al., *Characterization of strain-induced crystallization of poly(ethylene terephthalate) at fast draw rates using synchrotron radiation*. Polymer, 1996. **37**(15): p. 3303.
4. Cobbs, W.H.J. and B. R.L., *Crystallization of polyethylene terephthalate*. J. Poly. Sci., 1952. **10**(3): p. 275.
5. Foster, E.L., *The Rheology of Elastomers*. 1957: Pergamon Press NY.
6. Hamidi, A., A.S. Abhiraman, and P. Asher, *Melt Spinning of Poly(ethylene terephthalate) - Structural Transitions In a Range of Spinning Speeds*. Journal of Applied Polymer Science, 1983. **28**(2): p. 567.
7. Hristov, H.A. and J.M. Schultz, *Thermal response and structure of PET Fibers*. J. Poly. Sci., Part B: Poly. Phys., 1990. **28**: p. 1647-1663.
8. LeBourvellec, G., L. Monnerie, and J.P. Jarry, *Amorphous Orientation And Induced Crystallization In Uniaxially Stretched Poly(Ethylene Terephthalate Glycol)*. Polymer, 1986. **27**(6): p. 856.
9. Lu, X.F. and J.N. Hay, *Crystallization orientation and relaxation in uniaxially drawn poly(ethylene terephthalate)*. Polymer, 2001. **42**(19): p. 8055.
10. Mahendrasingam, A., et al., *Effect of draw ratio and temperature on the strain-induced crystallization of poly (ethylene terephthalate) at fast draw rates*. Polymer, 1999. **40**(20): p. 5553.
11. Mahendrasingam, A., et al., *Observation of a transient structure prior to strain-induced crystallization in poly(ethylene terephthalate)*. Polymer, 2000. **41**(3): p. 1217.
12. Napolitano, M.J. and A. Moet, *Effect Of Processing Conditions On Structure Evolution In Melt Spun Poly(Ethylene Terephthalate) Fibers*. Journal of Applied Polymer Science, 1986. **32**(5): p. 4989.
13. Napolitano, M.J. and A. Moet, *Mechanism Of Cold Drawing In Melt-Spun Poly(Ethylene Terephthalate) Fibers*. Journal of Applied Polymer Science, 1987. **34**(3): p. 1285.
14. Peszkin, P.N., J.M. Schultz, and J.S. Lin, *Kinetics of fiber heat treatment. II. Poly(ethylene terephthalate) Fibers*. J. Poly. Sci., Part B: Poly. Phys., 1986. **24**: p. 2591-2616.
15. Salem, D.R., *Crystallization during hot-drawing of poly (ethylene terephthalate) film: influence of temperature on strain-rate/draw-time superposition*. Polymer, 1994. **35**(4): p. 771.
16. Salem, D.R., *Crystallization during hot-drawing of poly(ethylene terephthalate) film: influence of the deformation mode*. Polymer, 1995. **36**(18): p. 3605.

17. Salem, D.R., *Orientation and crystallization in poly(ethylene terephthalate) during drawing at high temperatures and strain rates*. Polymer Engineering and Science, 1999. **39**(12): p. 2419.
18. Schrauwen, B.A.G., et al., *Intrinsic deformation behavior of semicrystalline polymers*. Macromolecules, 2004. **37**(16): p. 6069.
19. Shimizu, J., et al., *High Speed Melt Spinning of Poly Ethylene Terephthalate (PET): Effects of Melt-Draw Ratio and Flow Rate*. Sen-i-Gakkaishi, 1978. **34**(2): p. T-64.
20. Shimizu, J., et al., *High Speed Melt Spinning of Poly Ethylene Terephthalate (PET): Effect of Molecular Weight*. Sen-i-Gakkaishi, 1978. **34**(3): p. T-93.
21. Spruiell, J.E., D.E. McCord, and R.A. Beuerlein, *Effect Of Strain History On The Crystallization Behavior Of Bulk Poly(Ethylene Terephthalate)*. Transactions of the Society of Rheology, 1972. **16**(3): p. 535.
22. Thompson, A.B., *Strain-Induced Crystallization in Polyethylene Terephthalate*. J. Poly. Sci., 1959. **34**: p. 741-760.
23. Allison, S.W. and I.M. Ward, *Cold drawing of polyethylene terephthalate*. British Journal of Applied Physics, 1967. **18**(8): p. 1151.
24. Dargent, E., et al., *Effect of macromolecular orientation on the structural relaxation mechanisms of poly(ethylene terephthalate)*. Polymer, 2005. **46**(9): p. 3090.
25. Dulmage, W.J. and A.L. Geddes, *Structure of drawn polyethylene terephthalate*. J. Poly. Sci., 1958. **31**: p. 499.
26. Fernandez, J.O. and G.M. Swallowe, *Crystallization of PET with strain, strain rate and temperature*. Journal of Materials Science, 2000. **35**(17): p. 4405.
27. Heuvel, H.M. and R. Huisman, *Effect Of Winding Speed On The Physical Structure Of As-Spun Poly(Ethylene Terephthalate) Fibers, Including Orientation-Induced Crystallization*. Journal of Applied Polymer Science, 1978. **22**(8): p. 2229.
28. Hotter, J.F., et al., *Effect of initial take-up speed on properties and structure of as-spun and drawn/heat-set poly(ethylene terephthalate) filaments*. Journal of Applied Polymer Science, 1998. **69**(11): p. 2115.
29. Hristov, H.A., et al., *Rapid mechanical deformation of poly(ethylene terephthalate) fibers at temperatures above the glass transition*. Journal of Polymer Science, Part B: Polymer Physics, 1995. **33**(1): p. 125.
30. Matthews, R.G., et al., *Effects of stress relaxation on the structure and orientation of tensile drawn poly(ethylene terephthalate)*. Polymer, 2000. **41**(19): p. 7139.
31. Salem, D.R., *Crystallization kinetics during hot-drawing of poly (ethylene terephthalate) film: strain rate/draw-time superposition*. Polymer, 1992. **33**(15): p. 3189--3192.
32. Salem, D.R., *Development of crystalline order during hot-drawing of poly(ethylene terephthalate) film: influence of strain rate*. Polymer, 1992. **33**(15): p. 3182-3188.
33. Swallowe, G.M., J.O. Fernandez, and S. Hamdan, *Crystallinity increases in semi crystalline polymers during high rate testing*. Journal De Physique. IV : JP, 1997. **7**(3): p. 453.

34. Gupta, V.B., S.K. Sett, and A. Venkataraman, *Flow-drawing of poly(ethylene terephthalate)*. Polymer Engineering and Science, 1990. **30**(19): p. 1252.
35. Haruko Sasano, T.K., *On the mechanism of the flow process of poly(ethylene terephthalate)*. Die Makromolekulare Chemie, 1983. **184**(1): p. 217-223.
36. Qian, R., J. Shen, and L. Zhu, *Crystallization and chain orientation in hot drawn amorphous poly(ethylene terephthalate) films*. Die Makromolekulare Chemie, Rapid Communications, 1981. **2**(8): p. 499-505.
37. Radhakrishnan, J. and V.B. Gupta, *Characterization of the network in nonbirefringent flow-drawn poly(ethylene terephthalate) films*. Journal of Macromolecular Science - Physics, 1993. **B32**(2): p. 243.
38. DuPont, *Super-stretching polyester filaments, yarns, films, and similar structures*, U.K.P. Office, Editor. 1953: U.K. .
39. Pace, A., *Superstretching Polyester Structures*, USPO, Editor. 1949: USA.
40. Aneja, A.P., *Circumferential Superdrawing of hollow poly(ethylene terephthalate) filaments*. Textile Research Journal, 2004. **74**(4): p. 365.
41. Aneja, A.P., *Efficient Circumferential Superdrawing*. Journal of Applied Polymer Science, 2005. **97**: p. 123.
42. Shimizu, J. and T. Kikutani, *Dynamics and evolution of structure in fiber extrusion*. Journal of Applied Polymer Science, 2002. **83**(3): p. 539.
43. Kawaguchi, T., *Studies on straining of amorphous polyethylene terephthalate above the glass temperature*. Journal of Applied Polymer Science, 1961. **5**(16): p. 482-490.
44. Kim, K.H., A.I. Isayev, and K. Kwon. *Flow-induced crystallization and birefringence in high-speed spun pet fibers*. 2004. Chicago, IL., United States: Society of Plastics Engineers.
45. Kim, K.H., A.I. Isayev, and K. Kwon, *Flow-induced crystallization in the injection molding of polymers: A thermodynamic approach*. Journal of Applied Polymer Science, 2005. **95**(3): p. 502.
46. Kim, K.H., et al., *Modeling and experimental study of birefringence in injection molding of semicrystalline polymers*. Polymer, 2005. **46**(12): p. 4183.
47. Kwon, K., A.I. Isayev, and K.H. Kim, *Toward a viscoelastic modeling of anisotropic shrinkage in injection molding of amorphous polymers*. Journal of Applied Polymer Science, 2005. **98**(5): p. 2300.
48. Flory, P.J., *Thermodynamics of Crystallization in High Polymers. I. Crystallization Induced by Stretching*. The Journal of Chemical Physics, 1947. **15**(6): p. 397-408.
49. Yeh, G.S.Y. and K.Z. Hong, *Strain-Induced Crystallization, Part III: Theory*. Polymer Engineering and Science, 1978. **19**(6): p. 395-400.
50. W. R. Krigbaum, R.-J.R., *Diffraction study of crystallite orientation in a stretched polychloroprene vulcanizate*. Journal of Polymer Science Part A: General Papers, 1964. **2**(10): p. 4391-4414.
51. Kim, H.G. and L. Mandelkern, *Crystallization kinetics of stretched natural rubber*. Journal of Polymer Science -- Polymer Physics Part A-2, 1968. **6**(1): p. 181-196.
52. Yeh, G.S.Y., *Strain-Induced Crystallization, Part I: Limiting Extents of Strain-Induced Nuclei*. Polymer Engineering and Science, 1976. **16**(3): p. 138-144.

53. Mandelkern, L., *Polymer Crystallization: Progress and Problems*. Polymer PrePrints, ACS, Division of Polymer Chemistry, 1978. **19**(1): p. 286-289.
54. Wu, W., *Thermodynamic Approach to Deformation-induced Crystallization in Crosslinked Polymer Networks*. Polymer PrePrints, ACS, Division of Polymer Chemistry, 1978. **19**(1): p. 294-297.
55. Yeh, G.S.Y., *Strain-Induced Crystallization, Part II: Subsequent Fibrillar-To-Lamellar Transformation*. Polymer Engineering and Science, 1976. **16**(3): p. 145-151.
56. R. J. Gaylord, D.J.L., *Morphological changes during oriented polymer crystallization*. Polymer Engineering & Science, 1976. **16**(3): p. 163-167.
57. R. J. Gaylord, *A theory of the stress-induced crystallization of crosslinked polymeric networks*. Journal of Polymer Science: Polymer Physics Edition, 1976. **14**(10): p. 1827-1837.
58. A. Ziabicki, H.K., ed. *High-Speed Fiber Spinning*. 1985, John Wiley & Sons, Inc. 586.
59. G. Vassilatos, B.H.K., H.R.E. Frankfort, in *High-Speed Fiber Spinning*, H.K. A. Ziabicki, Editor. 1985, John Wiley & Sons, Inc. p. 383-428.
60. Kawaguchi, T., in *High-Speed Fiber Spinning*, H.K. A. Ziabicki, Editor. 1985, John Wiley & Sons, Inc. p. 3-20.
61. J. Shimizu, N.O., T. Kikutani, in *High-Speed Fiber Spinning*, H.K. A. Ziabicki, Editor. 1985, John Wiley & Sons, Inc. p. 429-484.
62. H.M. Heuvel, R.H., in *High-Speed Fiber Spinning*, H.K. A. Ziabicki, Editor. 1985, John Wiley & Sons, Inc. . p. 295-332.
63. Yasuda, H., in *High-Speed Fiber Spinning*, H.K. A. Ziabicki, Editor. 1985, John Wiley & Sons, Inc. p. 363-382.
64. H. H. George, A.H., A. Buckley,, *A study of structural development in the high speed spinning of poly(ethylene terephthalate)*. Polymer Engineering & Science, 1983. **23**(2): p. 95-99.
65. George, H.H., in *High-Speed Fiber Spinning*, H.K. A. Ziabicki, Editor. 1985, John Wiley & Sons, Inc. p. 271-294.
66. Doufas, A.K., I.S. Dairanieh, and A.J. McHugh, *A continuum model for flow-induced crystallization of polymer melts*. Journal of Rheology, 1999. **43**(1): p. 85-109.
67. Doufas, A.K., A.J. McHugh, and C. Miller, *Simulation of melt spinning including flow-induced crystallization: Part I. Model development and predictions*. Journal of Non-Newtonian Fluid Mechanics, 2000. **92**(1): p. 27-66.
68. McHugh, A.J. and A.K. Doufas, *Modeling flow-induced crystallization in fiber spinning*. Composites - Part A: Applied Science and Manufacturing, 2001. **32**(8): p. 1059-1066.
69. McHugh, A.J., W.H. Kohler, and P. Shrikhande, *Modelling of flow-enhanced crystallisation in fibre spinning*. Plastics, Rubber and Composites, 2004. **33**(9-10): p. 377-382.
70. Jabarin, S.A. *Chemistry, processing, and morphology of poly(ethylene terephthalate)*. 1999. Anaheim, CA, USA: American Chemical Society, Washington, DC, USA.

71. Rabello, M.S. and R.M.R. Wellen, *The kinetics of isothermal cold crystallization and tensile properties of poly (ethylene terephthalate)*. Journal of Materials Science, 2005. **40**: p. 6099.
72. Zhiying Zhang, S.W., Minqiao Ren, Changfa Xiao, *Model of cold crystallization of uniaxially oriented poly(ethylene terephthalate) fibers*. Polymer, 2004. **45**: p. 4361.
73. Shirataki, H., et al., *Correlation Between Tensile Properties and Network Draw Ratio for Poly (ethylene terephthalate) Fibers with WideRange of Molecular Orientation and Crystallinity*. J Appl Polym Sci, 1997. **64**: p. 2631.
74. G'Sell, C., Jonas, J. J., *Determination of the plastic behaviour of solid polymers at constant true strain rate*. Journal of Materials Science, 1979. **14**(3): p. 583-591.
75. Ajji, A., et al., *Orientation of amorphous poly(ethylene terephthalate) by tensile drawing, roll-drawing, and die-drawing*. Polymer Engineering and Science, 1997. **37**(11): p. 1801.
76. Ajji, A., et al. *Roll-drawing and die-drawing of initially amorphous PET*. in *Annual Technical Conference - ANTEC, Conference Proceedings*. 1997. Toronto, Can: Soc of Plastics Engineers, Brookfield, CT, USA.
77. Ladouce, L., J. Perez, and R. Vassoille, *High speed deformation of the poly(ethylene terephthalate)*. Journal De Physique, III, 1996. **6**(1): p. 35.
78. Chandran, P. and S. Jabarin, *Biaxial orientation of poly(ethylene terephthalate). Part I: Nature of the stress-strain curves*. Advances in Polymer Technology, 1993. **12**(2): p. 119-132.
79. Chandran, P. and S. Jabarin, *Biaxial orientation of poly(ethylene terephthalate). Part II: The strain-hardening parameter*. Advances in Polymer Technology, 1993. **12**(2): p. 133-151.
80. Jabarin, S.A., *Strain-induced crystallization of poly(ethylene terephthalate)*. Polymer Engineering and Science, 1992. **32**(18): p. 1341-9.
81. Smith, P., P.J. Lemstra, and H.C. Booij, *Ultradrawing of high-molecular-weight polyethylene cast from solution. II. Influence of initial polymer concentration*. Journal of Polymer Science, Part B: Polymer Physics, 1981. **19**(5): p. 877-888.
82. Keum, J.K., et al., *Crystallization and transient mesophase structure in cold-drawn PET fibers*. Macromolecules, 2003. **36**(26): p. 9873.
83. Murthy, N.S., S.T. Correale, and H. Minor, *Structure of the amorphous phase in crystallizable polymers. Poly(ethylene terephthalate)*. Macromolecules, 1991. **24**(5): p. 1185.
84. Murthy, N.S., S.T. Correale, and R.A.F. Moore. *Characterization of the amorphous phase in nylon 6 fibers by X-ray diffraction*. 1991. Princeton, NJ, USA: Publ by John Wiley & Sons Inc, New York, NY, USA.
85. Alves, N.M., et al., *Glass transition and structural relaxation in semi-crystalline poly(ethylene terephthalate): a DSC study*. Polymer, 2002. **43**(15): p. 4111-4122.
86. Zaroulis, J.S. and M.C. Boyce, *Temperature, strain rate, and strain state dependence of the evolution in mechanical behaviour and structure of poly(ethylene terephthalate) with finite strain deformation*. Polymer, 1997. **38**(6): p. 1303-1315.

87. Chaari, F., M. Chaouche, and J. Doucet, *Crystallization of poly(ethylene terephthalate) under tensile strain: Crystalline development versus mechanical behaviour*. Polymer, 2003. **44**(2): p. 473-479.
88. F. Chaari, M.C., *Rheooptical investigation of the crystallization of poly(ethylene terephthalate) under tensile strain*. Journal of Polymer Science Part B: Polymer Physics, 2004. **42**(10): p. 1915-1927.
89. Hee Soo, M., et al., *Effect of shearing on crystallization behavior of poly(ethylene terephthalate)*. Journal of Applied Polymer Science, 2001. **80**(14): p. 2640.
90. Chan, T.W. and A.I. Isayev, *Quiescent polymer crystallization: Modeling and measurements*. Polymer Engineering and Science, 1994. **34**(6): p. 461-471.
91. Radhakrishnan, J. and A. Kaito, *Structure formation during the isothermal crystallization of oriented amorphous poly(ethylene terephthalate) films*. Polymer, 2001. **42**(8): p. 3859-3866.
92. K. G. Mayhan, W.J.J., Wouter Bosch,, *Poly(ethylene terephthalate). I. Study of crystallization kinetics*. Journal of Applied Polymer Science, 1965. **9**(11): p. 3605-3616.
93. Jabarin, S.A., *Crystallization kinetics of polyethylene terephthalate. I. Isothermal crystallization from the melt*. Journal of Applied Polymer Science, 1987. **34**(1): p. 85-96.
94. Jabarin, S.A., *Crystallization kinetics of Polyethylene Terephthalate. II. Dynamic crystallization of PET*. Journal of Applied Polymer Science, 1987. **34**(1): p. 97-102.
95. Ozawa, T., *Kinetics of non-isothermal crystallization*. Polymer, 1971. **12**(3): p. 150-158.
96. Alfonso, G.C., M.P. Verdoni, and A. Wasiak, *Crystallization kinetics of oriented poly (ethylene terephthalate) from the glassy state*. Polymer, 1978. **19**(6): p. 711-716.
97. Turnbull, D. and J.C. Fisher, *Rate of Nucleation in Condensed Systems*. The Journal of Chemical Physics, 1949. **17**(1): p. 71-73.
98. Nakamura, K., K. Katayama, and T. Amano, *Some aspects of nonisothermal crystallization of polymers. II. Consideration of the isokinetic condition*. 1973. p. 1031-1041.
99. G. S. Y. Yeh, K.Z.H., *Strain-induced crystallization, Part III: Theory*. Polymer Engineering & Science, 1979. **19**(6): p. 395-400.
100. Guo, X., *Crystallization, Microstructure, Residual Stresses and Birefringence in Injection Molding of Semicrystalline Polymer: Simulation and Experiment*. 1999, University of Akron, Ohio: Akron, Ohio. p. 67-96.
101. Flory, P.J., *Thermodynamics of Crystallization in High Polymers. IV. A Theory of Crystalline States and Fusion in Polymers, Copolymers, and Their Mixtures with Diluents*. The Journal of Chemical Physics, 1949. **17**(3): p. 223-240.
102. Boyce, M.C., S. Socrate, and P.G. Llana, *Constitutive model for the finite deformation stress-strain behavior of poly(ethylene terephthalate) above the glass transition*. Polymer, 2000. **41**(6): p. 2183.
103. I. M. Ward, *The role of molecular networks and thermally activated processes in the deformation behavior of polymers*. Polymer Engineering & Science, 1984. **24**(10): p. 724-736.

104. Buckley, C.P., D.C. Jones, and D.P. Jones, *Hot-drawing of poly(ethylene terephthalate) under biaxial stress: application of a three-dimensional glass-rubber constitutive model*. Polymer, 1996. **37**(12): p. 2403-2414.
105. Haward, R.N. and G. Thackray, *The Use of a Mathematical Model to Describe Isothermal Stress-Strain Curves in Glassy Thermoplastics*. Proceedings of the Royal Society of London. Series A, Mathematical and Physical Sciences, 1968. **302**(1471): p. 453-472.
106. Boyce, M.C., D.M. Parks, and A.S. Argon, *Large inelastic deformation of glassy polymers. I. Rate dependent constitutive model*. Mechanics of Materials, 1988. **7**(1): p. 15.
107. M. C. Boyce, E.M.A., *An experimental and analytical investigation of the large strain compressive and tensile response of glassy polymers*. Polymer Engineering & Science, 1990. **30**(20): p. 1288-1298.
108. Buckley, C.P. and D.C. Jones, *Glass-rubber constitutive model for amorphous polymers near the glass transition*. Polymer, 1995. **36**(17): p. 3301-3312.
109. Ashford, E., et al., *Prediction of orientation and crystallinity in drawn poly(ethylene terephthalate)*. Chemical Engineering Research and Design, Transactions of the Institute of Chemical Engineers, Part A, 2000. **78**(1): p. 33-38.
110. Diani, J., F. Bedoui, and G. Regnier, *On the relevance of the micromechanics approach for predicting the linear viscoelastic behavior of semi-crystalline poly(ethylene)terephthalates (PET)*. Materials Science and Engineering A, 2008. **475**(1-2): p. 229-234.
111. Mulliken, A.D. and M.C. Boyce, *Mechanics of the rate-dependent elastic-plastic deformation of glassy polymers from low to high strain rates*. International Journal of Solids and Structures, 2006. **43**(5): p. 1331-1356.
112. Poitou, A., et al., *Crystallization of polymers under strain: From molecular properties to macroscopic models*. Computer Methods in Applied Mechanics and Engineering, 2003. **192**(28-30): p. 3245-3264.
113. Richeton, J., et al., *A formulation of the cooperative model for the yield stress of amorphous polymers for a wide range of strain rates and temperatures*. Polymer, 2005. **46**(16): p. 6035-6043.
114. Shepherd, J.E., D.L. McDowell, and K.I. Jacob, *Modeling morphology evolution and mechanical behavior during thermo-mechanical processing of semi-crystalline polymers*. Journal of the Mechanics and Physics of Solids, 2006. **54**(3): p. 467-489.
115. Michael Rubinstein, R.H.C., *Polymer Physics*. 2004 ed. 2003: Oxford University Press. 440.
116. Boyce, M.C. and E.M. Arruda, *Constitutive models of rubber elasticity: A review*. Rubber Chemistry and Technology, 2000. **73**(3): p. 504-523.
117. Duan, Y., et al., *A uniform phenomenological constitutive model for glassy and semicrystalline polymers*. Polymer Engineering and Science, 2001. **41**(8): p. 1322-1328.
118. Zairi, F., et al., *Elasto-viscoplastic constitutive equations for the description of glassy polymers behavior at constant strain rate*. Journal of Engineering Materials and Technology, 2007. **129**(1): p. 29-35.

119. Adams, A.M., C.P. Buckley, and D.P. Jones, *Biaxial hot drawing of poly(ethylene terephthalate): Measurements and modelling of strain-stiffening*. Polymer, 2000. **41**(2): p. 771-786.
120. Sweeney, J. and I.M. Ward, *Rate dependent and network phenomena in the multiaxial drawing of poly(vinyl chloride)*. Polymer, 1995. **36**(2): p. 299-308.
121. Ball, R.C., et al., *Elasticity of entangled networks*. Polymer, 1981. **22**(8): p. 1010-1018.
122. Matthews, R.G., et al., *Biaxial drawing behaviour of poly(ethylene terephthalate)*. Polymer, 1997. **38**(19): p. 4795.
123. Vigny, M., et al., *Constitutive viscoplastic behavior of amorphous PET during plane-strain tensile stretching*. Polymer Engineering and Science, 1999. **39**(12): p. 2366.
124. Ahzi, S., et al., *Modeling of deformation behavior and strain-induced crystallization in poly(ethylene terephthalate) above the glass transition temperature*. Mechanics of Materials, 2003. **35**(12): p. 1139.
125. Makradi, A., et al., *A two-phase self-consistent model for the deformation and phase transformation behavior of polymers above the glass transition temperature: Application to PET*. International Journal of Plasticity, 2005. **21**(4): p. 741.
126. Arruda, E.M. and M.C. Boyce, *Three-dimensional constitutive model for the large stretch behavior of rubber elastic materials*. Journal of the Mechanics and Physics of Solids, 1993. **41**(2): p. 389.
127. Bergstrom, J.S. and M.C. Boyce, *Constitutive modeling of the large strain time-dependent behavior of elastomers*. Journal of the Mechanics and Physics of Solids, 1998. **46**(5): p. 931.
128. Dupaix, R.B. and M.C. Boyce, *Finite strain behavior of poly(ethylene terephthalate) (PET) and poly(ethylene terephthalate)-glycol (PETG)*. Polymer, 2005. **46**(13): p. 4827.
129. Dupaix, R.B. and M.C. Boyce, *Constitutive modeling of the finite strain behavior of amorphous polymers in and above the glass transition*. Mechanics of Materials, 2007. **39**(1): p. 39.
130. Toshio Kunugi, A.S., Minoru Hashimoto,, *Mechanical properties and superstructure of high-modulus and high-strength PET fiber prepared by zone annealing*. Journal of Applied Polymer Science, 1981. **26**(6): p. 1951-1960.
131. Michielsen, S., *Application of Raman Spectroscopy to Organic Fibers and Films*, in *Handbook of Raman Spectroscopy*, G.M.H. Ian R. Lewis, Editor. 2001, Marcel Dekker. p. 1054.
132. Ward, I.M., ed. *Structure and Properties of Oriented Polymers*. 1975, John Wiley & Sons, Inc. 475.
133. G. Urbarczyk, A.J., *Peculiarities of the Fine Structure of PET fibers and the Relationship to their Basic Physical Properties*, in *Handbook of engineering polymeric materials*, N.P. Cheremisinoff, Editor. 1997, Marcel Dekker. p. 881.
134. W. J. Dulmage, L.E.C., *A study of the elastic modulus and extensibility of the crystalline regions in highly oriented polymers*. Journal of Polymer Science, 1958. **28**(117): p. 275-284.

135. K. L. Peng, C.M.R., *The amorphous phase in high-speed spun PET fibers*. Journal of Polymer Science Part B: Polymer Physics, 1993. **31**(10): p. 1339-1345.
136. Yuezhen Bin, K.O., K. Yoshida, M. Matsuo, *Mechanical Properties of Poly(ethylene terephthalate) Estimated in Terms of Orientation Distribution of Crystallites and Amorphous Chain Segments under Simultaneous Biaxially Stretching*. Polymer Journal, 2004. **36**(11): p. 888-898.
137. Tashiro, K., *Molecular theory of mechanical properties of crystalline polymers*. Progress in Polymer Science (Oxford), 1993. **18**(3): p. 377-435.
138. Thistlethwaite, T., R. Jakeways, and I.M. Ward, *The crystal modulus and structure of oriented poly(ethylene terephthalate)*. Polymer, 1988. **29**(1): p. 61-69.
139. Nishino, T., H. Miyazaki, and K. Nakamae, *X-ray diffraction of polymer under load at cryogenic temperature*. Review of Scientific Instruments, 2002. **73**(4): p. 1809-1812.
140. Okui, N., Sakai, T., *Effect of monomeric unit length on crystallinity and young's modulus for highly oriented fibers*. Polymer Bulletin (Berlin), 1987. **17**(1): p. 79-85.
141. Ward, I.M., *The mechanical behavior of poly(ethylene terephthalate)*. Journal of Macromolecular Science, Part B, 1967. **1**(4): p. 667 - 694.
142. Salem, D.R., *Microstructure development during constant-force drawing of poly(ethylene terephthalate) film*. Polymer, 1998. **39**(26): p. 7067-7077.
143. Lorentz, G. and J.F. Tassin, *Molecular description of constant-load stretching of amorphous poly(ethylene terephthalate) films*. Polymer, 1994. **35**(15): p. 3200-3205.
144. Kardos, J.L., *Short-Fiber-Reinforced Polymeric Composites, Structure-Property Relations*, in *Handbook of composite reinforcements*, S.M. Lee, Editor. 1993, Wiley-VCH. p. 715.
145. Rule, M., *Physical Constants of Poly(oxyethylene-oxyterephthaloyl) (Poly(ethylene terephthalate))*, in *Polymer Handbook*, E.H.I. J. Brandrup, E.A. Grulke, Editor. 1999, John Wiley & Sons, Inc. p. 113.
146. Treloar, L.R.G., *The Physics of Rubber Elasticity*. 3rd ed. 1975: Clarendon Press. 310.